MEDNARODNA PODIPLOMSKA ŠOLA JOŽEFA STEFANA
JOŽEF STEFAN INTERNATIONAL POSTGRADUATE SCHOOL

MILOVAN ŠUVAKOV

NETWORK MODELS OF SELF-ASSEMBLED FUNCTIONAL MATERIALS

DOCTORAL DISSERTATION

LJUBLJANA, NOVEMBER 2008

NETWORK MODELS OF SELF-ASSEMBLED FUNCTIONAL MATERIALS

Doctoral Dissertation
Jožef Stefan International Postgraduate School
Ljubljana, Slovenia, November 2008

Supervisor: *Prof. Dr. Bosiljka Tadić*

Evaluation Board:

Prof. Dr. Dragan Mihailović, Chairman, Jožef Stefan Institute, Ljubljana, Slovenia
Prof. Dr. Philip Moriarty, Member, University of Nottingham, Nottingham, UK
Prof. Dr. Raša Pirc, Member, Jožef Stefan Institute, Ljubljana, Slovenia

Milovan Šuvakov

Network Models of Self-Assembled Functional Materials

Doctoral Dissertation

Modeliranje samourejenih funkcionalnih materialov s pomočjo teorije omrežij

Doktorska disertacija

Supervisor: Prof. Bosiljka Tadić

November 2008

MEDNARODNA PODIPLOMSKA ŠOLA JOŽEFA STEFANA
JOŽEF STEFAN INTERNATIONAL POSTGRADUATE SCHOOL
Ljubljana, Slovenia

Work on this thesis was done at the Department of Theoretical Physics, Jožef Stefan Institute, Ljubljana, Slovenia. The research was supported by Marie Curie Training and Research Network, European Project MTRN-CT-2004-005728 (PATTERNS).

Acknowledgements

I would like to thank people who made this Thesis possible. First of all, I would like to express my gratitude to my Ph.D. supervisor, Prof Bosiljka Tadić for the help, enthusiasm and inspiration during the research.

I would also like to thank Prof Philip Moriarty and other collaborators from the PATTERNS project.

Thanks to Prof Raša Pirc for useful discussions and encouragement for my work.

Many thanks to my colleagues Zoran Levnajić and Lev Vidmar for their support and intriguing discussions. I am also grateful to the personnel of Department of Theoretical Physics and my other coworkers at the Department.

Thanks to Prof Rajmund Krivec for help with administering Department computer facilities during my work.

Finally, I take this opportunity to express my profound gratitude to my lovely fiancee Sonja Čučulanović for her love, patience and support during my long stay in Slovenia.

Contents

Abstract

The fabrication of functional materials composed of metallic nanoparticles is one of the most important steps in the contemporary nanotechnology. Nonlinear self-assembly of nanoparticles into macroscopic aggregates are promising methods in which various structures can be obtained by tuning certain control parameters. Such large-scale aggregates exhibit new physical features, which are often induced by the structural complexity of the system.

In this thesis, we study the self-assembly processes of metallic nanoparticles on substrates with numerical methods. The aggregates or nanoparticle films are further investigated by examining their structure and their conduction via quantum tunnelling under applied voltage. Our approach is based on mapping the nanoparticle films onto planar graphs, or nano-networks, which enable quantitative analysis of the structure and dynamical processes using the methods of graph theory and statistical physics of complex networks.

Three models of the nanoparticle aggregates are introduced and studied: (a) networks based on fixed positions of the nanoparticles on substrate from empirical data; (b) nearly-equilibrium assemblies emerging in bio-molecular recognition binding; and (c) cellular networks grown by cell-aggregation rules. Charge transport through such nano-neworks is simulated, introducing a generalized model of single-electron conduction through capacitively coupled nanoparticle arrays. That nontrivial topology can lead to new conduction properties is shown. Specifically, non-linear current-voltage characteristics and non-Gaussian fluctuations at the electrode can arise due to the coalescence of conduction pathways through the sample, and long-range temporal correlations of charge fluctuations along the conduction pathways.

Povzetek

Produkcija funkcionalnih materialov, ki so zgrajeni iz kovinskih nanodelcev, je eden od pomembnejših korakov v sodobni nanotehnologiji. Ena od obetajočih metod je nelinearen proces samoureditve nanodelcev v makroskopske skupke, kjer lahko s spreminjanjem nekaterih kontrolnih parametrov ustvarimo različne strukture. Značilnost takih skupkov so nekatere nove fizikalne lastnosti, ki so pogosto posledica kompleksne strukture sistema.

V tej doktorski dizertaciji se ukvarjamo z numerično študijo procesov samoureditve kovinskih nanodelcev na substratih. Raziskujemo lastnosti tako dobljenih skupkov z pomočjo analize njihove strukture ter prevodnosti zaradi kvantnega tuneliranja posameznih elektronov pod vplivom zunanje napetosti. Naš približek temelji na mapiranju nanodelčnih filmov na planarne grafe, ali nano-omrežja, kar nam z uporabo metod teorije grafov in statistične fizike kompleksnih omrežij omogoča kvantitativno analizo strukture in dinamičnih procesov. Vpeljemo in raziskujemo tri modele nanodelčnih skupkov: (a) omrežja, ki temeljijo na empirično pridobljenih podatkih o pozicijah nanodelcev na substratih; (b) skoraj ravnovesne ureditve, ki so posledica vezave na podlagi bio-molekulskega prepoznavanja; ter (c) celična omrežja, ki nastanejo v procesih kopičenja manjših skupkov (celic) nanodelcev.

Z vpeljavo posplošenega modela prevodnosti posameznih elektronov skozi kapacitivno sklopljene nanodelčne filme simuliramo transport naboja skozi opisana nano-omrežja. Netrivialna topologija nano-omrezja lahko vodi do novih prevodniških lastnosti. Pojavijo se lahko nelinearne lastnosti odvisnosti toka od napetosti ter negausovske fluktuacije toka na elektrodah zaradi sovpliva prevodnih poti skozi film in korelacij dolgega dosega v časovnih fluktuacijah naboja vzdolž teh prevodnih poti.

Chapter 1

Introduction

Nanoscale metallic particles have potentially useful electronic, optical and material properties due to their small size. In the recent years, different methods had been developed for their assembly into useful macroscopic devices, e.g. for nanosensors, or as new functional materials (Mirkin, 2000; Moriarty, 2001). In contrast to the rapid technological progress, full understanding of the physical processes on these scales and their practical applications remain limited. The self-assembly of the nanoparticles into macroscopic aggregates is a promising approach, which leads to locally stable structures that can be tuned via control parameters. The self-assembly processes are nonlinear, driven processes and subject to various constraints (Nepomnyashchy & Golovin, 2006; Robinson, 2003; Tadić, 2008), often leading to complex multiscale structures; therefore, the control of such processes is a challenging problem. The theoretical analysis of such complex dynamical systems is in the focus of the contemporary statistical physics. The study of the self-assembly processes, the topological properties of the emergent aggregates, and the dynamical processes on them could provide better understanding physics of the integrated nanosystems. This is the leading idea of this thesis.

In this Thesis, we focus on the numerical study of two-dimensional metallic nanoparticle films, in particular, their structures and physical processes—conduction by quantum tunnelings of the electron through the junctions between nanoparticles. Our approach is based on the mapping of the nanoparticle films onto planar graphs (nano-networks), which then enables the use of the quantitative methods of graph theory to study their structures. Furthermore, numerical modeling and simulations of the conduction processes on these networks connects the physical properties of the nanoparticle films to their structure.

The thesis is divided into three interconnected parts. In the first part, we concentrate

on the graph presentations of two-dimensional nanoparticle assemblies. We use two different approaches: in one, we construct the dynamical network using the empirical data about the positions of nanoparticles on the substrate (Blunt *et al.*, 2007c; Šuvakov & Tadić, 2007) ;in the other, we develop a formal model for growing planar graphs with aggregation of cells, i.e. small clusters of nanoparticles. (Šuvakov & Tadić, 2006a,b). In both cases the elements of conducting nanoparticle networks are defined as follows: the nodes represent metallic nanoparticles, while the network links (edges) are the *tunneling junctions* between pairs of the nanoparticles.

The second part of the thesis is devoted to numerical modeling of the charge conduction through the nanoparticle films. It has been observed experimentally that the conduction through metallic nanoparticle films on substrates has interesting dynamical properties (Blunt *et al.*, 2007c; Elteto *et al.*, 2005; Parthasarathy *et al.*, 2004; Rimberg *et al.*, 1995; Wybourne *et al.*, 1997). Under external voltage, the film behaves as a capacitively-coupled system. Due to the small size and thus the small capacitance of nanoparticles, charging of a particle by a single electron would increase the energy of the particle enough to induce the effect known as the Coulomb blockade (Bakhvalov *et al.*, 1991; Ferry & Goodnick, 1997; Geigenmuller & Schon, 1989; Middleton & Wingreen, 1993). Under these conditions, the main conduction mechanism is the quantum electron tunneling through the junctions between neighboring metallic nanoparticles. In contrast to classical conduction, single electron tunneling processes have numerous advantages, e.g., the absence of dissipation due to heating, and nonlinear current-voltage characteristics, which are important in nanoelectronics (Guo *et al.*, 1997). Experiments on nanoparticle arrays show highly nonlinear conduction. We perform a numerical study of this dynamical system using modified Middleton-Wingreen model (Middleton & Wingreen, 1993) and systematically investigate the influence of underlying topology of the nanoparticle film on non-linear conduction properties. We study in detail the properties of the conduction processes through the nanoparticle film, which reveals the physical ground for the observed I-V nonlinearity. The collective dynamic behavior along the conducting paths through the nanoparticle film leads to the nonlinear currentvoltage curves, correlations in time series of the charge fluctuation, and a fat-tail distributions and scale invariance. The scaling exponents and other quantitative indicators of the dynamics vary when certain topological features of the graph are changed.

In the third part of the Thesis, we study one specific type of the self-assembly processes in order to show how such diverse structures of nanoparticle films and other aggregates may emerge from the same process. In particular, we present a model of colloidal aggregation in which binding between nanoparticles utilizes the biological recognitions of the attached molecules (Mirkin,

2000). Generally, this is a self-assembly process in binary mixtures of nanoparticles coated with complementary chemistry such as DNA strands (Aldaye *et al.*, 2008). Our theoretical approach includes: modeling potential of the interactions between the particles, numerically solving the Langevin equation and the representation and analysis of emergent structures. One of the goals is finding the relationship between the parameters of assembly and the inter particle potentials, on one side, and the resulting stable aggregates, on the other. Here we study such systems where the particles of coated with different strands of the DNA interacting via an attractive potential (cooperative interplay of hydrogen-bonding, $\pi-$stacking, electrostatic, and hydrophobic interactions (Aldaye *et al.*, 2008)). We assume that the attractive potential is a general Lennard-Jonestype potential while a short-range repulsive interaction occurs in the case of particles carrying the same type of molecules. The dynamics which is determined with Langevin equation and the above interactions is far from the thermodynamic equilibrium but. However, in low temperature limits, the final self-assembled assembles apeare to be stable. We considertwo-dimensional structures under varying parameters. In the case of small clusters, we are also able find the ground state configuration. This model of the colloidal aggregation could be considered as a another method of self-assembly of the nanoparticle films, but also a wide class of other aggregates can be obtained generally known as binary colloidal aggregation (Aldaye *et al.*, 2008; Blunt *et al.*, 2007a; Likos, 2001; Nykypanchuk *et al.*, 2008; Park *et al.*, 2008).

In the remaining part of the Introduction we will describe in more details the phenomenology and theoretical backgrounds of two self-assembly processes and introduce some basic concepts of the graph theory and physics of complex networks which are nessesery for our study in Chapters 2 and 3.

1.1 Self-Assembly Processes of Nanoparticle Films

Self-assembly (Alivisatos *et al.*, 1996; Moriarty, 2001) of molecules or nanoparticles is a process without guidance from an outside source. During this stochastic process which is far from the thermodynamic equilibrium nanoscale objects spontaneously assemble until a stable structure (local energy minimum) is reached. This type of processes is of a non-linear nature and to a certain extent can be controlled by external parameters. It is a strikingly elegant and economic approach to the formation of various structures with different sizes, shapes and physical properties (Tadić, 2008). Over the past decade, many important reviews of metallic nanoparticle synthesis and self-assembly have been published by leading scientists in the field, including

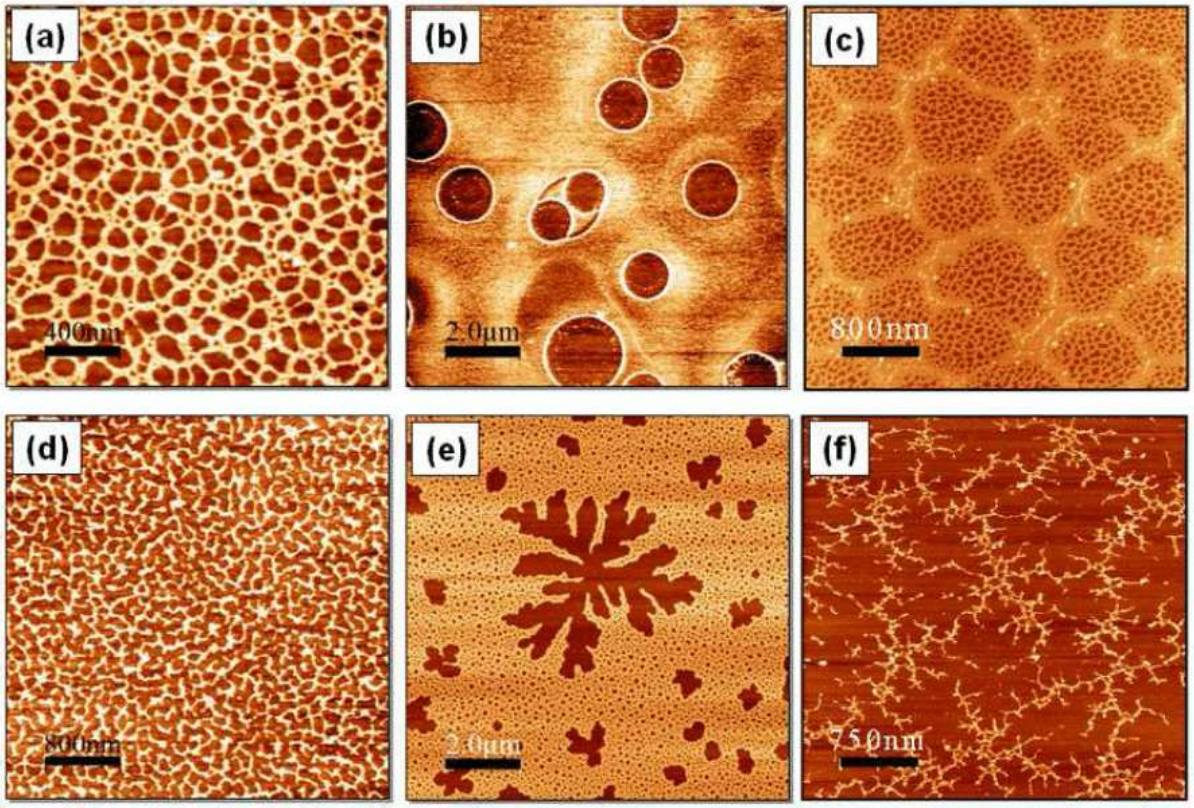

Figure 1.1: A selection of tapping mode atomic force microscope (AFM) images of the patterns formed by thiol-passivated Au nanoparticles deposited from an organic solvent onto silicon substrates. The scale bars in the images are: (a) $400nm$, (b) $2\mu m$, (c) $800nm$, (d) $800nm$, (e) $2\mu m$, (f) $750nm$. Figure from (Stannard *et al.*, 2008)

(Mirkin, 2000; Moriarty, 2001; Murray *et al.*, 2000; Nykypanchuk *et al.*, 2008; Park *et al.*, 2008; Pileni, 2001, 2006, 2007; Storhoff & Mirkin, 1999).

Two examples of the self-assembly processes that we will examine in this thesis are: drying-meditated pattern formation and self-assembly via biorecogniton binding. In this section, we review recent developments in the understanding and control of these two kinds of self-assembly processes.

Drying Meditated Pattern Formation

Figure 1.1 shows a representative subset of self-organized patterns formed by thiol-passivated *Au* nanoparticles (2nm diameter) via dewetting of a droplet of colloidal solution on native oxide-terminated Si (111) substrates (Stannard *et al.*, 2008). The different morphologies are ob-

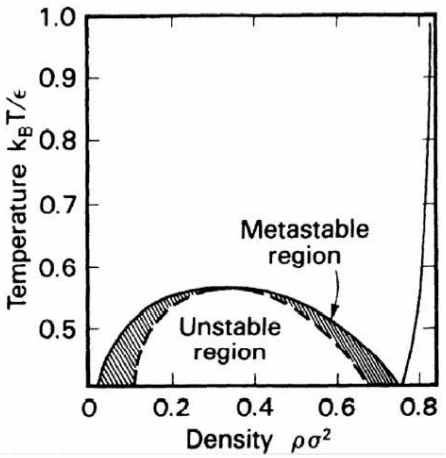

Figure 1.2: Temperature-density phase diagram of a $2D$ Lennard-Jones system. The solid line represents the binodal, while the dashed line is the spinodal which separates the metastable region from the unstable region. A reduced temperature quench through the critical temperature (0.55 in units of k_BT/ϵ, where ϵ is the interparticle interaction energy) into the unstable region of the phase diagram leads to spinodal decomposition. Figure from (S. W. Koch, 1983)

served depending on the external parameters: cellular structures, isolated droplets figure 1.1(b), dendritic aggregates figure 1.1(f), branching and fingering structures figure 1.1(e), labyrinthine assemblies, and isolated rings.

The key formation mechanisms and physics of the self-assembly process are presented in the work of (Ge & Brus, 2000; Rabani *et al.*, 2003) where they proposed that self-organization of colloidal nanoparticles occurred through fluid-fluid spinodal phase separation of a two-dimensional system of particles interacting via a Lennard-Jones type potential. Figure 1.2 is the universal two-dimensional phase diagram (S. W. Koch, 1983) around which Ge and Brus based their arguments. Perhaps the most important point with regard to colloidal nanoparticle systems is that evaporation of the solvent is equivalent to a reduced temperature quench, driving the system from the gas-liquid coexistence region (i.e. the upper region of Figure 1.2) to phase-separation, either in the unstable region of the phase diagram (spinodal decomposition) or in the metastable (nucleation and growth) regime. The critical temperature, in units of k_BT/ϵ is 0.55, at a coverage of 0.325 monolayer. Removal of the solvent results in less effective screening of the van der Waals interactions between the nanoparticles, driving the phase transition, and producing intricate, spatially correlated patterns of nanoparticles, highly reminiscent of those observed in

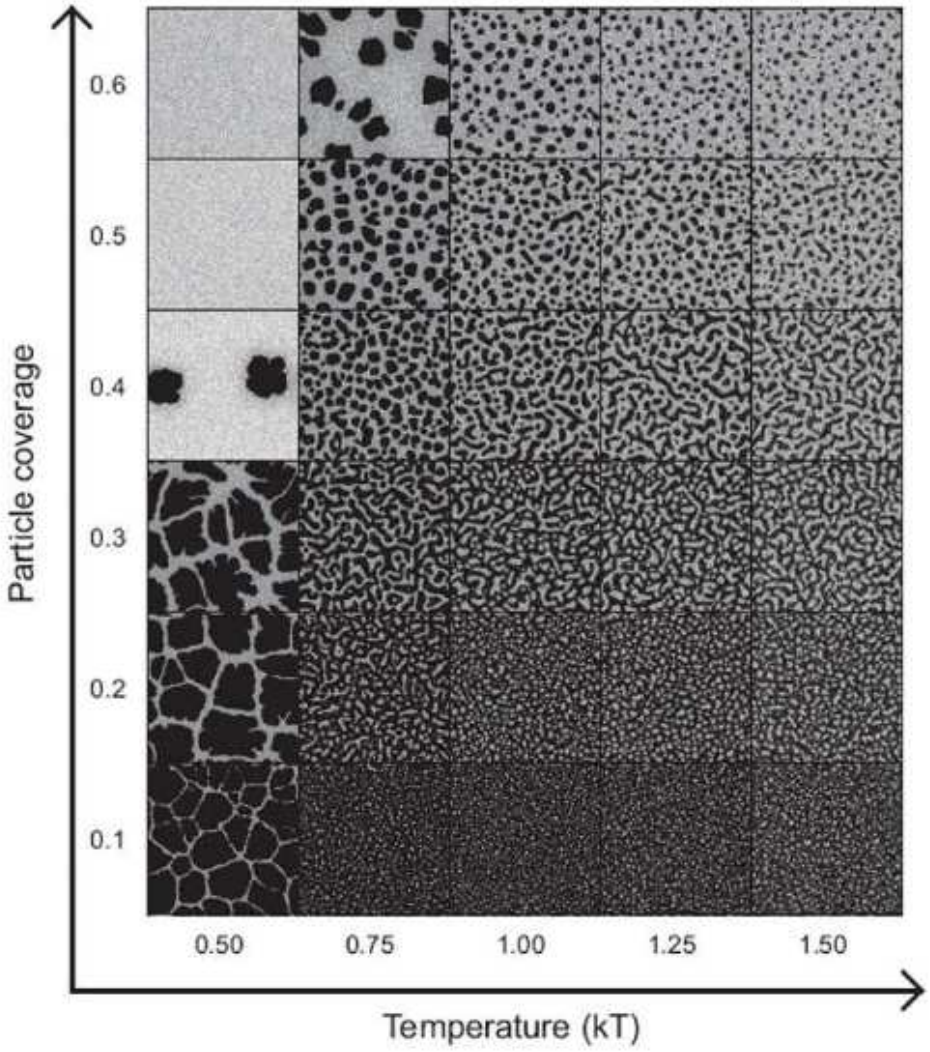

Figure 1.3: A representative set of nanoparticle assemblies generated using the (Rabani *et al.*, 2003) Monte Carlo model discussed in the text. A coverage vs temperature diagram is shown where each image is the result of running the simulation for 1000 Monte Carlo steps in a 1024×1024 solvent cell system with $l = 2$, $n = 2l$, $nl = 1.5l$, and a mobility ratio of 20. Taken from (Stannard *et al.*, 2008)

other systems which phase separate via a spinodal process (binary fluids, polymer blends) - see, for example, Fig 1.1(d).

The Rabani model suggested in (Rabani *et al.*, 2003) puts forward an important numerical model of colloidal nanoparticle systems, which takes into account the dynamics of the solvent

evaporation. In their lattice gas model, the two-dimensional plane is divided into square cells with size of the liquid coherence length. The cell can be occupied with a nanoparticle or with liquid. Two dynamic variables are defined at each cell, l_i and n_i, which can take two values 1 or 0, corresponding to the presence or the absence of the liquid/nanoparticle. A single nanoparticle occupies several cells. The Hamiltonian for the model is given as:

$$\mathcal{H} = -\epsilon_\ell \sum_{<ij>} \ell_i \ell_j - \epsilon_n \sum_{<ij>} n_i n_j - \epsilon_{n\ell} \sum_{<ij>} n_i \ell_j - \mu \sum_i \ell_i, \tag{1.1}$$

where ϵ_n, ϵ_ℓ, and $\epsilon_{n\ell}$ are interaction strengths for nanoparticle-nanoparticle, liquid-liquid and nanoparticle–liquid interaction, retrospectively. In equation (1.1) $< ij >$ indicates interaction pairs (i.e. nearest neighbors (Rabani *et al.*, 2003) or next-nearest neighbors ((Blunt *et al.*, 2007b; Martin *et al.*, 2004; Yosef & Rabani, 2006)). The chemical potential μ regulates the equilibrium liquid–vapor concentration.

The kinetics of the model comprises two processes: nanoparticle diffusion and liquid evaporation/condensation. The particle mobility rate (MR) is an important control parameter and determines the relative frequency of events due to these processes. A key element of the model is that nanoparticles can diffuse only in the presence of the solvent in cells neighboring the particle. The Monte Carlo dynamics for each of the two processes is performed with the acceptance probability:

$$p_{accept} = min(1, \exp\left[-\Delta H_\kappa / k_B T\right]) \ , \tag{1.2}$$

where ΔH_{evap} and ΔH_{diff} are the changes in the total energy associated with the attempted process, respectively, computed from the Hamiltonian (1.1). Figure 1.3 shows a region of the phase diagram for the Rabani model where some of the primary types of nanoparticle assembly observed experimentally - networks, worm-like domains and labyrinths, and droplets - are reproduced.

We will focus on the special case (see figure 1.1(a) and figure 1.4) with a structure known as the cellular structure and whose morphology is examined in (Moriarty *et al.*, 2002). Random cellular structures (networks) are usualy found in nature (Stavans, 1993) as evolving non-equilibrium systems. The structure can be described as composition of nearly-uniform domains of polygonal shape separated by thin (almost one-dimensional) boundaries. Although cellular networks are results of many different processes they obey some universal lows which are described in (Stavans, 1993). In this thesis, we study in detail the topology of these cellular networks using numerically generated planar graphs, which we grow by cell-aggregation procedure.

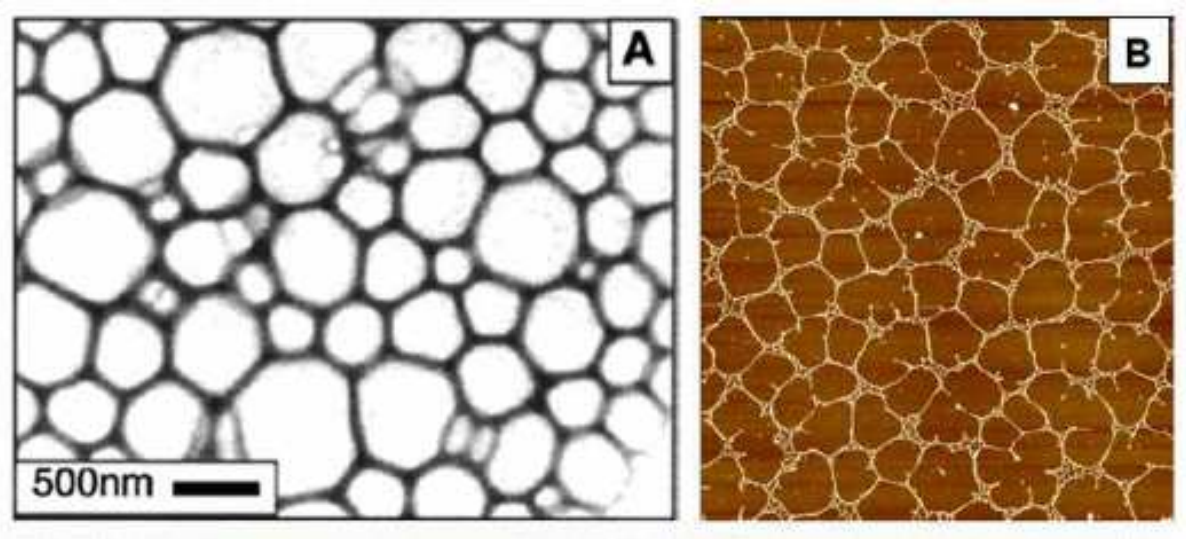

Figure 1.4: Examples of cellular network formations: (a) Transmission electron microscope image of polygonal pattern arising from Marangoni convection in drying Ag nanoparticle solutions. Figure from (Maillard *et al.*, 2000). (b) Dual-scale network formation in a submonolayer coverage of pentanethiol-passivated Au nanoparticles ($2nm$ diameter) on a native-oxide ter- minated Si(111) sample. Figure from (Moriarty *et al.*, 2002).

Furthermore, the conduction trough such and other nanoparticle structures will be studied and compared with the experiments.

Self-Assembly of Nanoparticles with Bio-Molecular Recognition

In recent years, the study of dynamical relaxation toward a stable configuration in colloidal or more generally in soft matter systems, has gained increasing scientific attention (Likos, 2001; Lu *et al.*, 2008; Zaccarelli, 2007). In contrast, the integration of biological molecules with nanoscale materials is an interdisciplinary task of great practical importance. Colloidal nanoparticles coated with functional biomolecules can be applied in different fields, from manufacturing of nanodevices or biosensors to medicine (drug delivery) (Alivisatos, 2004).

The assembly of nanosize colloidal particles ligated with the complementary chemistry is studied. Recently, different methods for this kind of assembly have been developed (Mirkin, 2000; Mirkin *et al.*, 1996; Nykypanchuk *et al.*, 2008; Park *et al.*, 2008). Consider two types of colloidal particles, A and B, which are ligated by biopolymers, such that the complementary parts of the molecule are attached to different particle type. Some well-known examples are the proteins with specific reactions, e.g., in the antigenantibody recognition (Huber, 1986) and

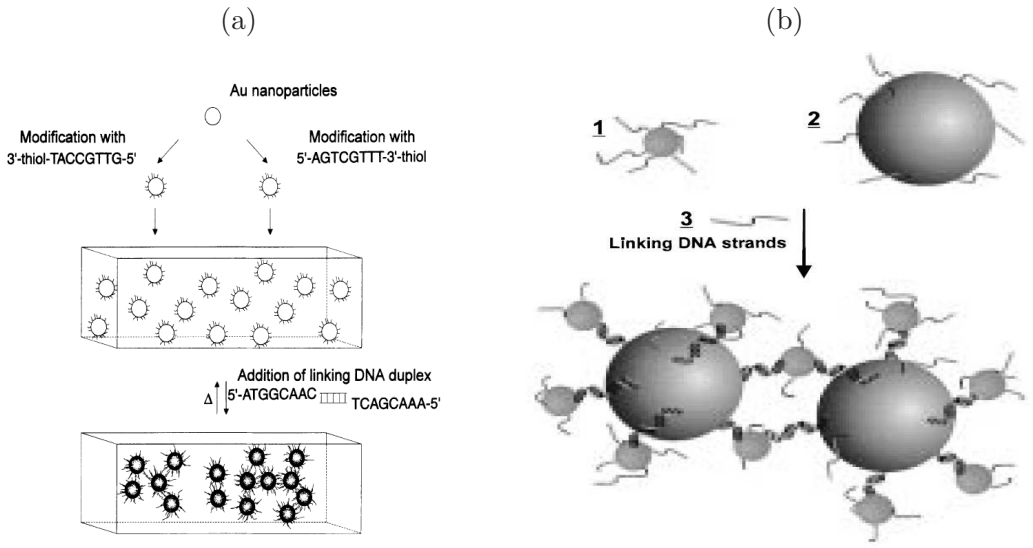

Figure 1.5: Two different types of nanoparticles coated with DNA duplex with floppy ends. Linker DNA strands have floppy ends which perfectly recognize the sequences attached on the two different kinds of nanoparticles. Taken from (Mirkin, 2000)

in the complementary pieces of DNA molecule, see figure 1.5, where the strength of bonding is directly related to the number of complementary base pairs. It was demonstrated recently (Nykypanchuk *et al.*, 2008; Park *et al.*, 2008) that, by varying the lengths of the free and the bonding parts of the ligands, different three-dimensional structures of nanoparticles may emerge, including regular BCC-like supra-crystals. Two examples of emergent structures are shown on figure 1.6.

Our theoretical approach is finding relations between control parameters, the inter particle potentials and the resulting stable aggregate. Here we will study such systems where particles of the different kind interacting via an attractive potential (which can be of hydrogen-bond or van der Walls origin) and short repulsive interaction in the case of particles of the same kind. The kinetics of the system was described with a Langevin equation in the high viscosity media.

1.2 Basics of Complex Networks Theory

In this section, we will give short introduction to the methods of graph theory, the physics of complex networks, and the graph visualization tools used in thesis.

In mathematics, a *graph* is defined as an ordered pair of disjoint sets $G = (V, E)$ such that

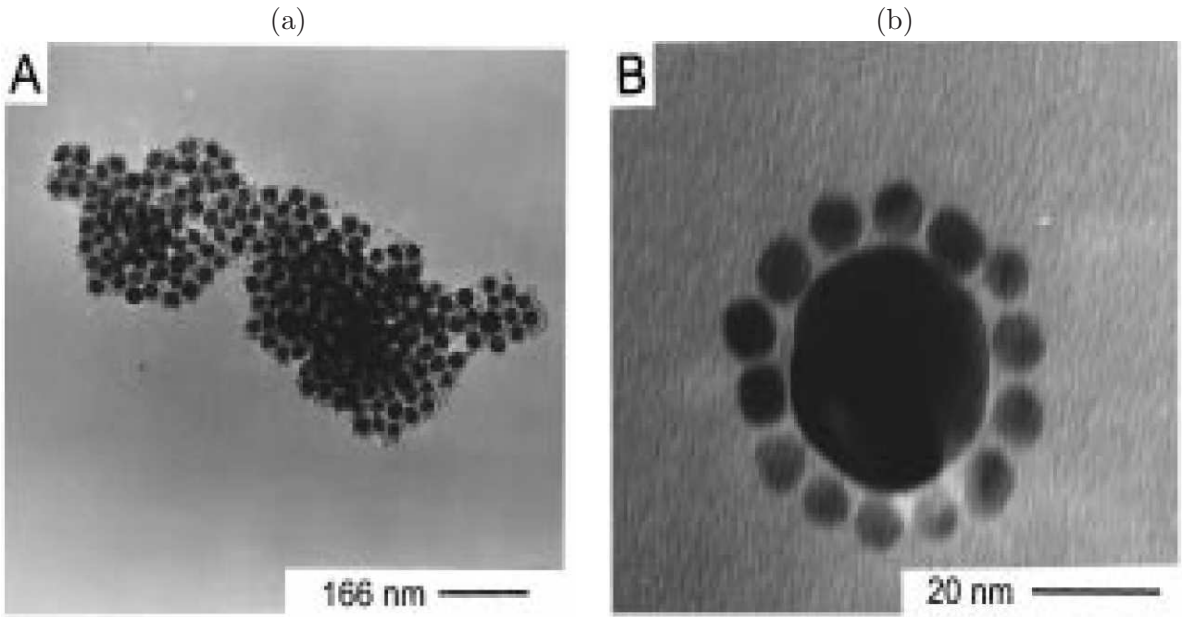

Figure 1.6: Taken from (Mirkin, 2000)

E is subset of the set $V \times V$ of ordered pairs of V. V is set *vertices* (nodes) and E is set of *edges* (links). If G is a graph, then $V = V(E)$ is the vertex set of G and $E = E(G)$ is the edge set. An edge $(x, y) \in E(G)$ is said to connect vertices x and y. If $(x, y) \in E(G)$, than x and y are *adjacent* or *neighboring* vertices of G. If for all $(x, y) \in E(G) \Rightarrow (y, x) \in E(G)$ than the graph G is *undirected*.

Here we consider only finite graphs, that is V and E are always finite. In this case we can enumerate vertices $V = \{v_i, v_2, ..., v_n\}$ where n is cardinality of V (number of vertices). The *adjacency* matrix A of the graph G is $n \times n$ matrix with zero diagonal elements $a_{ii} = 0$ and with off-diagonal elements a_{ij} equal to 1 if there is edge from vertex v_i to vertex v_j or to zero otherwise. More formally:

$$a_{ij} = \begin{cases} 0 & \text{if } i = j \text{ or } (i, j) \notin E(G) \\ 1 & \text{if } (i, j) \in E(G) \end{cases} \tag{1.3}$$

There exists a unique adjacency matrix for each graph (up to permuting rows and columns), and it is not the adjacency matrix of any other graph. If the graph is undirected the corresponding adjacency matrix is symmetric. On figure 1.7 is shown an simple example of a graph and corresponding adjacency matrix.

A graph is a *weighted graph* if a real number (weight) is assigned to each edge. Such weights

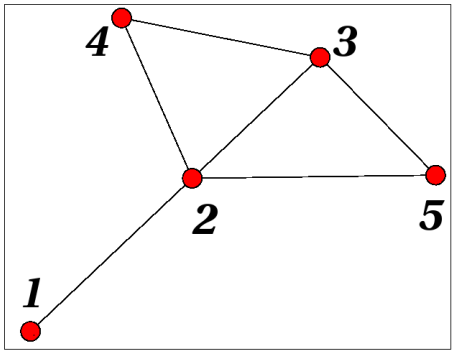

$$A = [a_{ij}] = \begin{pmatrix} 0 & 1 & 0 & 0 & 0 \\ 1 & 0 & 1 & 1 & 1 \\ 0 & 1 & 0 & 1 & 1 \\ 0 & 1 & 1 & 0 & 0 \\ 0 & 1 & 1 & 0 & 0 \end{pmatrix}$$

Figure 1.7: Simple example of a graph and its adjacency matrix

might represent, for example, electric current, lengths or capacities, etc., depending on the problem. In this case adjacency matrix is defined similarly but with weights as non-zero elements insted ones.

We define that $G' = (V', E')$ is a *subgraph* of a graph $G = (V, E)$ if $V' \subset V$ and $E' \subset E$. If $V = V'$ then G' is said to be a *spanning subgraph* of G. A graph H is called a *minor* of the graph G if H is isomorphic to a graph that can be obtained by zero or more edge deletions or edge contractions on a subgraph of G. A *subdivision* of a graph G is a graph resulting from zero or more subdivisions of edges in G. The subdivision of some edge (u, v) in G yields a graph containing one new vertex w, and with an edge set replacing (u, v) by two new edges (u, w) and (w, v).

A *path* in a graph G is a sequence of different vertices $\{v_1, v_2, .., v_m\}$ such that from each of its vertices there is an edge to the next vertex in the sequence $((v_i, v_{i+1}) \in E(G))$. The first vertex v_1 is called the start vertex and the last vertex v_m is called the end vertex. Both of them are called end or terminal vertices of the path. The other vertices in the path are internal vertices. A *cycle* is a path such that the start vertex and end vertex are the same. Notice that unlike with paths, any vertex of a cycle can be chosen as the start, so the start is often not specified. In general, the path between two vertices is not unique. The *length of the path* is defined as number of edges in path or as sum of weights for weighted graphs. The *shortest path* between two vertices is defined as a path with minimal length. The shortest path between two vertices is not necessarily unique.

A *tree* is a graph in which any two vertices are connected by exactly one path. Furthermore, a tree is an undirected simple graph G that satisfies any of the following equivalent conditions:

- G is connected and has no cycles.
- G has no cycles, and a simple cycle is formed if any edge is added to G.
- G is connected, and it is not connected anymore if any edge is removed from G.
- G is connected and the 3-vertex complete graph K_3 is not a minor of G.
- Any two vertices in G can be connected by a unique simple path.

If G has finitely many vertices, say N of them, then the above statements are also equivalent to any of the following conditions:

- G is connected and has $N - 1$ edges.
- G has no simple cycles and has $N - 1$ edges.

Spanning tree of a graph G is a tree which is also spanning subset of the graph G. Maximum (minimum) spanning tree of a weighted graph is the spanning tree with maximal (minimal) sum of weights over the edges. The algorithm we used to find minimum spanning tree is Prim's algorithm (Prim, 1957). This algorithm continuously increases the size of a tree starting with a single vertex until it spans all the vertices by adding a single node per time step which is connected to the tree by the edge with smallest weight.

Planar graphs are special class of graphs that can be embedded in a Euclidean plane in such a way that its edges intersect only at their endpoints. *Kuratowski's theorem* provide a characterization of planar graphs: *A graph is planar iff it does not contain as subgraphs a subdivision of K_5 (5-clique) and $K_{3,3}$ (minimal non-planar graph with 6 nodes)* (Bollobás, 1998). Consequently, planar graphs fulfill *Euler's law*: $N_p + N = E + 1$, which is relating the number of nodes N, links E and polygons N_p.

A *complex network* is a network (graph) with non-trivial topological features that do not occur in simple networks such as lattices or random graphs. The study of complex networks is a recent and active area of scientific research, inspired largely by the empirical study of real-world networks such as computer networks and social networks. Most social, biological, and technological networks display substantial non-trivial topological features, with patterns of connection between their elements that are neither purely regular nor purely random (Dorogovtsev & Mendes, 2003). Such features include a heavy tail in the degree distribution, a high clustering

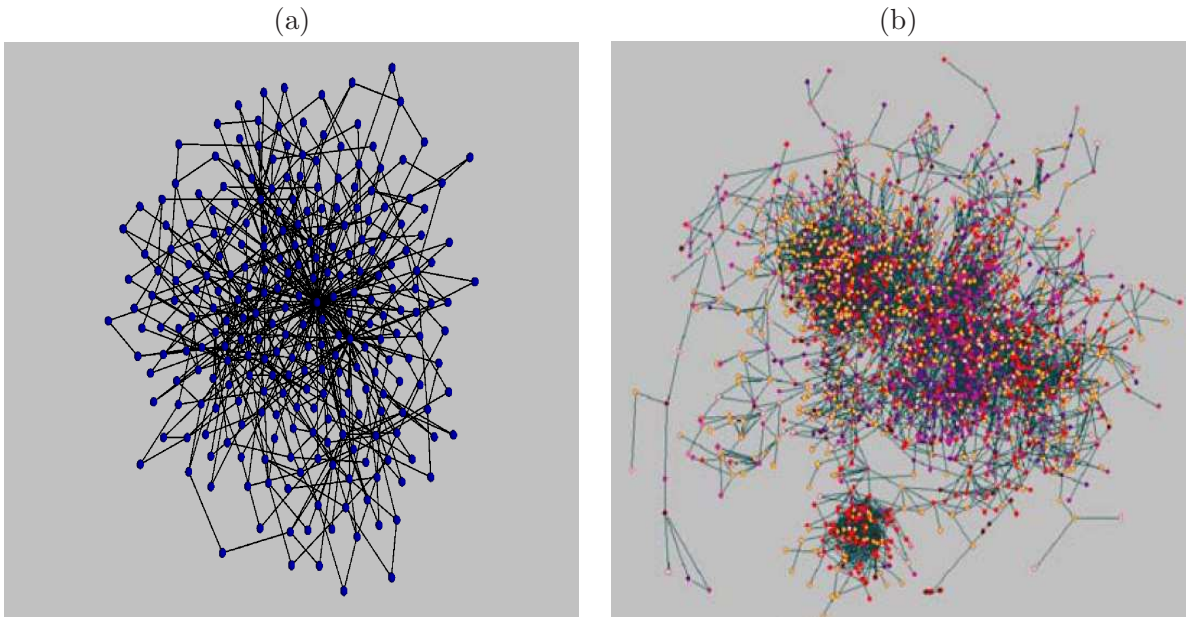

Figure 1.8: Two examples of complex networks: (a) Scale-free clustered network (generated using model (Tadić, 2001)); (b) Gene expression correlation network based on empirical data (figure taken from (Živković *et al.*, 2006))

coefficient, assortativity or disassortativity among vertices, community structure, and hierarchical structure. Well-known lattices and random graphs do not show these topological features. Two much-studied types of complex networks are scale-free networks and small-world networks, whose discovery and definition started large research activity in the field (Bollobás, 1998). A scale-free network is network with low-power distribution of node degrees. These kinds of networks can be often found in social, biological or computer sciences. Two examples of scale-free networks are given on figure 1.8.

The statistical physics of complex networks is a theory that uses methods of statistical physics to study evolution and structure of the complex networks. In this theory, formal graph models are used as representation of real graphs. There are few different methods for the generation of graphs that can be divided into two groups: (1) static networks; (2) growing networks. In growing network, the algorithms are used to generate graphs with the addition of one/more nodes and connect them with already present nodes using stochastic or deterministic rules. There is variety of such models proposed in last decade, for instance (Albert & Barabasi, 2002; Boccaletti *et al.*, 2006; Tadić, 2001; Šuvakov & Tadić, 2006a).

Mapping complex dynamical systems to network is an usefull tool within the follow con-

cepts: (1) quantitative analysis of structure of complex systems using graph theory methods (Živković *et al.*, 2006); (2) nodes/links can have properties in numerical modeling of network function (Argollo de Menezes & Barabasi, 2004; Tadić, 2008; Tadić *et al.*, 2005); (3) simulation of dynamical processes on graphs (Blunt *et al.*, 2007c; Kujawski *et al.*, 2007; Tadić, 2006; Tadić & Thurner, 2004; Šuvakov & Tadić, 2006b, 2007, 2008). These three concepts are the guiding idea in our work for representating the nanoparticle films by planar networks.

1.3 Graph Visualization Tools

This section will be devoted to graph visualization methods and tools which we use in this Thesis.

Graph drawing, as a branch of graph theory, applies topology and geometry to derive two-dimensional representations of graphs. Graph drawing is motivated by applications such as circuit design, social network analysis, cartography, and bioinformatics. Also, graph drawing can help in better understanding of the graph structure.

A drawing of a graph is graphical representation of an embedding of the graph in the $2D$ Euclidian plane, usually aimed at a convenient visualization of certain properties of the graph in question or of the object modeled by the graph. Graphs are usually represented graphically using circles or dots to represent vertices, and arcs to represent the edges between connected vertices. Arrows can be used to show the orientation of directed edges in the case of directed graph. Note that this graphical representation (a graph *layout* or an embedding) should not be confused with the graph itself (the abstract, non-graphical structure). Very different layouts may correspond to the same graph. Generally speaking, all that matters is which vertices are connected to which other and by how many edges. In practice, however, the arrangement of these vertices and edges impacts understandability, usability, fabrication cost, and aesthetics.

Terminology and Definition of the Problem: For a given graph $G = (V, E)$, the graph visualization is mapping between the vertices and two-dimensional or three-dimensional coordinates $f : V \rightarrow \mathbb{R}^n$ (where $n \in \{2, 3\}$). The quality of mapping is not precisely defined, but several criteria are generally accepted. One possibility is the minimization of the number of edge crossing (Šuvakov, 2008) in the layout. While some graphs cannot be drawn without edge crossings, some other graphs can. Planar graphs belong to this group. To test uncrossing property of the visualization algorithms in this paper, we will use model of cell-aggregated planar graphs which we were introduced in (Šuvakov & Tadić, 2006a). Other criteria for satisfactory of visualization

often used are: minimization of variance in the edge lengths, maximization of the minimal angle between neighboring edges, minimization of the number of bends in the edges, minimization of different slopes used in edge visualization, and other (Eades, 1984; Kamada & Kawai, 1989).

Based on these concepts, different graph layouts exist. We studied and used a strategy known as force-based layout, which is based on gradient-descent minimization of an energy function. We proposed a modification of existing spring model using next-neighbor approximation (Šuvakov, 2008). More about force-based layout and this modification which is appropriate for scale-free clustered graphs can be found in the Appendix A. Some other graph visualization strategies which proved applicable for specific types of graphs are: spectral layout (layout using as coordinates the eigenvectors of a matrix such as the Laplacian derived from the adjacency matrix of the graph), orthogonal layout (layout with edges running horizontally or vertically, with approaches that reduce the number of edge crossovers and area covered), symmetric layout (these attempt to find symmetry groups within the graph), tree layout (shows a rooted tree-like formation, suitable for some types of trees), hierarchical layouts (based on attempts to find a source and sink within a directed graph and arrange the nodes in layers with most edges starting from the source and flowing in the direction of the sink) (Di Battista *et al.*, 1998).

Apart from own methods, in this Thesis, we also use the free software "Pajek" (Batagelj, 2008) for graph analysis and visualization.

Chapter 2

Network Models of Conducting Nanoparticle Films

In this chapter we concentrate on graph representations of conducting nanoparticle assemblies and analysis of their structure. Our motivation is to find out how the topological properties of arrangements influence non-linear I-V characteristics in conduction via single electron tunneling studied in Chapter 3. We use two different approaches: in one, we construct the network using the empirical data of the positions of nanoparticles on the substrate (Blunt *et al.*, 2007c; Šuvakov & Tadić, 2007); in other, we develop a mathematical model for growing planar graph with aggregation of cells (Šuvakov & Tadić, 2006a,b). In both approaches in the conducting nanoparticle networks (*nano-network*): the network *nodes* represent the metallic nanoparticles, while the network *links* (edges) are the tunneling junctions between pairs of neighboring nanoparticles.

2.1 Nanonetworks from Empirical Data

In this case we propose mapping nanoparticle films to a nano-network without detailed knowledge about the self-assembly process. We assume that the positions of nanoparticles on the substrate are known, e.g., either from STM measurements or by statistical estimates based on the parameters of the deposition process. Under an applied voltage across the film the electron tunneling conductance fall exponentially with distance between nanoparticles (Ferry & Goodnick, 1997) and for a large enough distance it can be neglected. We define the tunneling radius r as the distance beyond which the tunneling conduction is negligible.

We make a nano-particle film network by connecting pairs of nanoparticles, which are spaced within a tunneling radius r from each other. In addition when the positions of the electrodes are

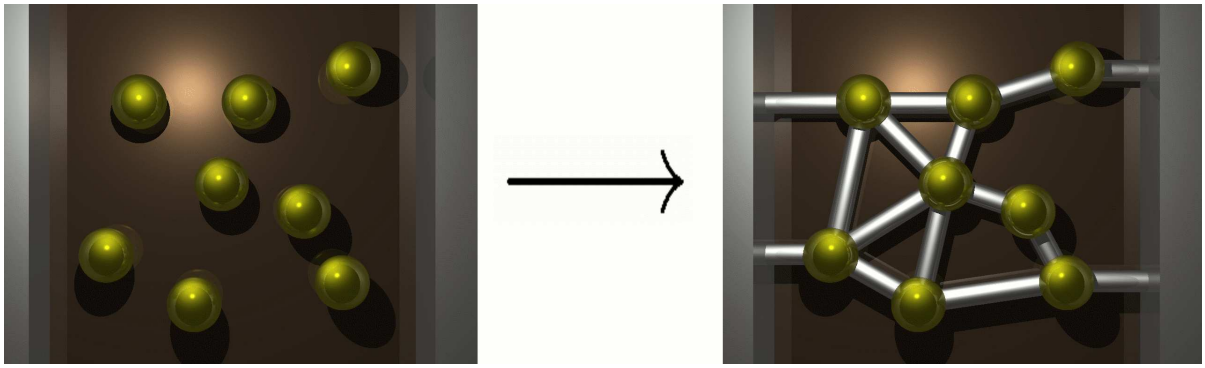

Figure 2.1: Construction of conduction network from positions of nanoparticles on substrate between the electrodes. The nanoparticles within tunneling radius are connected.

known, we connect the nanoparticles with the electrode if the distance between them is smaller than r. The procedure is schematically illustrated in Figure 2.1. In our numerical experiment, the tunneling radius r is an additional parameter in the network model.

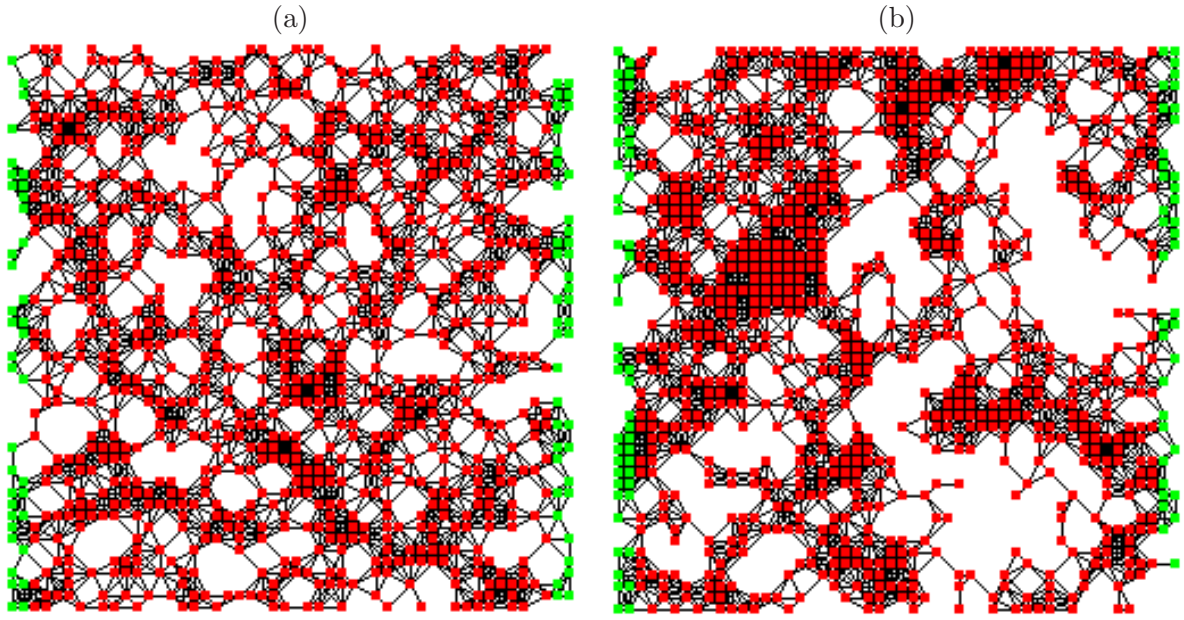

Figure 2.2: Examples of the nano-particle films with (a) random and (b) correlated deposition at density $\rho = 10\%$ grid points covered by particles. Network edges are shown corresponding to the tunneling radius r of 2 grid points

As an example we generate two types of films, shown in Figure 2.2, by sequential deposition of particles of a unique size (determined by the grid spacing). In Figure 2.2(a) the deposition site for a new particle is randomly selected away from already occupied sites, resulting in a random homogeneous structure. In Figure 2.2(b), however, we apply (self-avoiding) random-walk dynamics to select the deposition sites. In this case, the non-linear self-avoiding process leads to a correlated deposition, with inhomogeneity voids of different scales (Lawler, 1991). In both cases we put $N = 1000$ particles on the rectangular plane with 100×100 grid points.

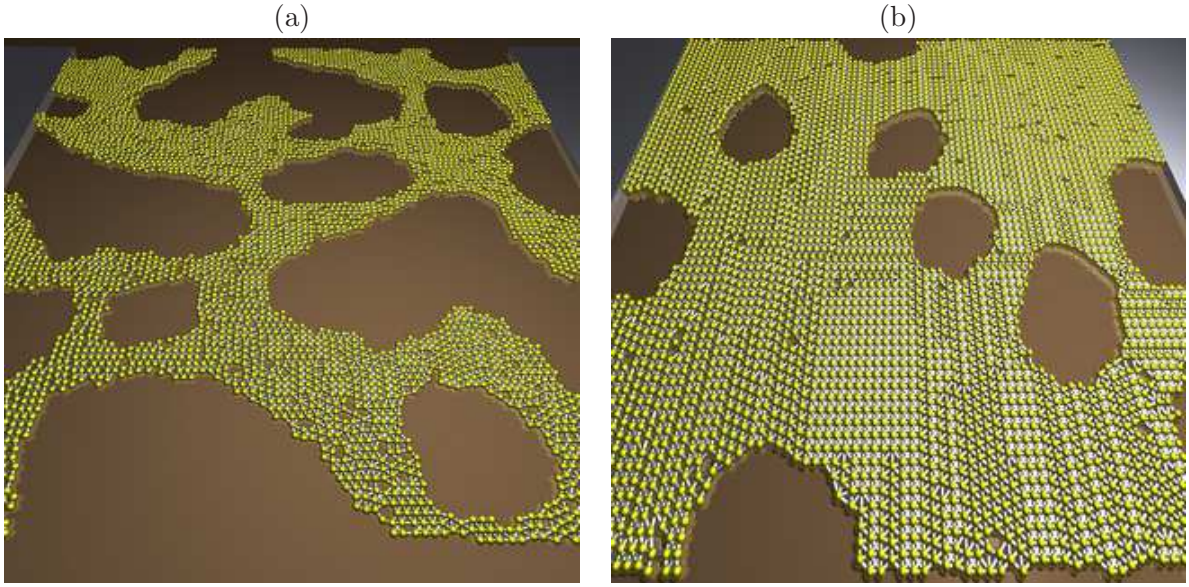

Figure 2.3: A three-dimensional rendering of a simulated nanoparticle network structure used in the transport calculations. Networks are made using coordinates from the model described in Ref. (Martin *et al.*, 2004). Two networks correspond to two different nanoparticle coverage of: (a) 40% ($NNET1$), and (b) 80% ($NNET2$). (Blunt *et al.*, 2007c)

A second example of nano-particle film networks used in our transport calculations in Chapter 3 are shown in Figure 2.3. The coordinates of nanoparticles are taken from simulations within the discrete model introduced in Chapter 1 (Martin *et al.*, 2004; Rabani *et al.*, 2003), for a nanoparticle coverage value of 40% ($NNET1$) and 80% ($NNET2$). These networks are associated with topological characteristics as measured by tessellation and Minkwoski measures (Martin *et al.*, 2004) which closely match those observed in experiment (Blunt *et al.*, 2007c).

In Figure 2.4 we show two topological properties of these two networks: the distribution of the lengths of shortest paths defined in Chapter 1 and the distribution of betweenness centrality

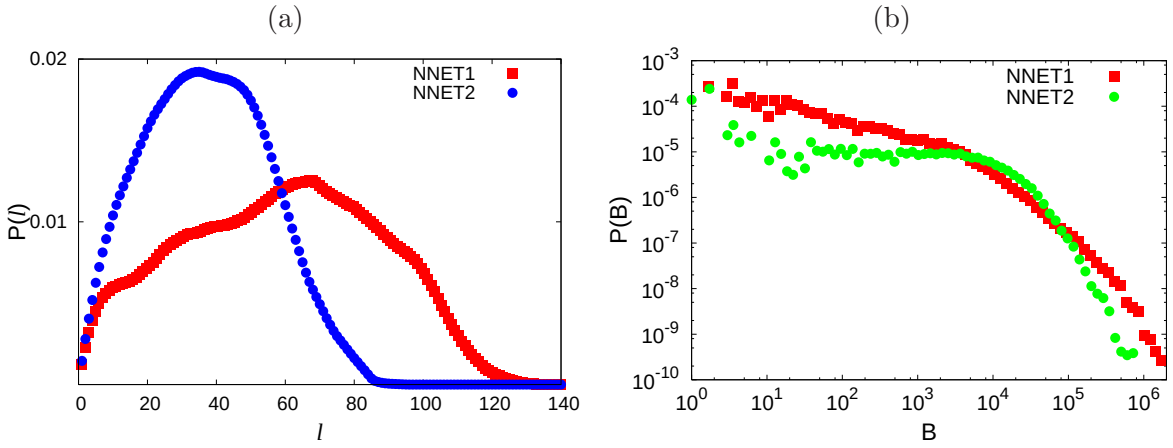

Figure 2.4: Topological properties of nanoparticle networks shown on figure 2.3: (a) Distribution of lengths of shortest paths on networks for $NNET1$ and $NNET2$. (b) Distributions of betweenness centrality of links for these networks

of links.Betweenness centrality of a node in network is defined by (Bollobás, 1998; Freeman, 1977)

$$C_B(v) = \sum_{s \neq v \neq t} \frac{\sigma_{st}(v)}{\sigma_{st}} \tag{2.1}$$

where σ_{st} is total number of shortest paths between nodes s and t, and $\sigma_{st}(v)$ is the number of these paths that node v lies on. Betweenness of links is defined in analogous way. In our algorithm, we record the number of shortest paths through each node and through each link on a network.

The distribution of the shortest path lengths is different depending on coverage (Figure 2.4 (a)). The first nanoparticle network ($NNET1$) has more inhomogeneities in structure due to the small coverage and consequently there are more shortest paths at a larger scale. Although there is a majority of small paths in the case of the second network ($NNET2$), this is not a small-world network. In this case, the mean shortest path grows as the square root of the number of nodes, not as the logarithm. The different distributions for these two networks are only a consequence of structural inhomogeneities. This can be seen also in the distribution of betweenness centrality of links (Figure 2.4 (a)). The second network $NNET2$ has a similar distribution as a cell-aggregated network (Figure 2.9 (b)) which are very homogeneous (fixed degree $k = 3$). The inhomogeneities cause a large number of "bottle necks", links with large betweenness.

2.2 Cellular Networks: Planar Graph Growing Model

In this section we present another mathematical model of inhomogeneous planar graph with cellular structure. These cellular networks are graphs grown by attachment of small graphs (loops) of different sizes to the graph boundary. This model is adjusted to generate topology of well known cellular structures (Stavans, 1993) which are often found in nature, from those resembling the soap froths to cellular patterns of nano-particles self-assembled through nonlinear dynamic processes (Blunt *et al.*, 2007b; Moriarty *et al.*, 2002). Typically, a pattern of cells appears when nano-particles are immersed in a liquid film on a substrate, which is then allowed to evaporate and holes of different sizes open-up leaving particles in the walls between the holes (Moriarty, 2001; Moriarty *et al.*, 2002). The structure of these patterns affects the physical processes on them, such as current transport (Blunt *et al.*, 2007c). It is therefore important to understand the topology of the aggregated cellular networks in detail. Here we study the topological properties, such as shortest paths between nodes, topological centrality, and fractality of the graph's perimeter in different cellular networks obtained by varying the control parameters of the aggregation processes.

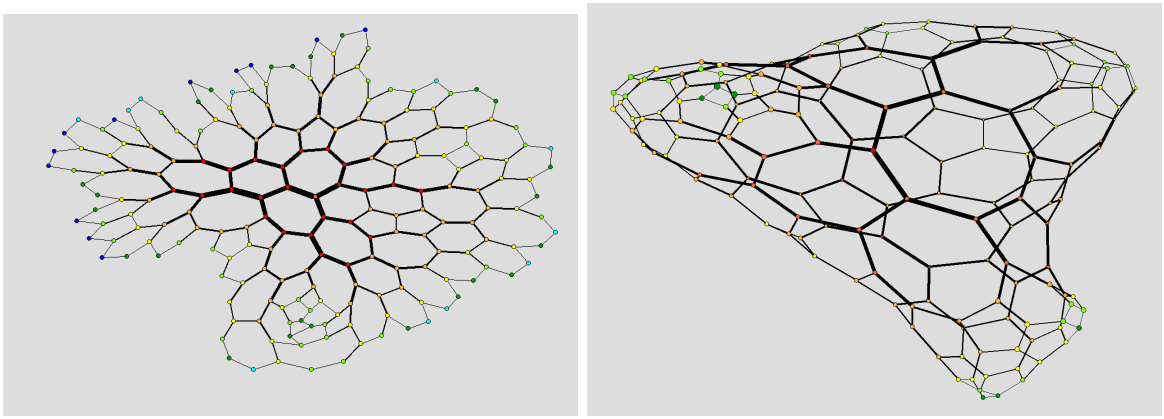

Figure 2.5: Two possible types of cell-aggregated *planar graphs*: open and closed structures, obtained by lognormal distribution with $\mu_2 = 1.0$, and aggregation potential $\nu = 5.0$.

Our method is based on growing planar cellular graphs by attachment of objects—cells (polygons) of length n_p, which are chosen from a given distribution $f(n_p)$. The polygons are added sequentially in time starting from an initial polygon. In addition, we strictly impose the constraint on number of links per node $k = 3$, which is thus fulfilled everywhere in the

interior of the graph and on some nodes on the graph boundary. This constraint is imposed by nature on real cellular structures (Stavans, 1993). The attachment of cells is controlled by two parameters—the width of the distribution of cell sizes μ_2 and the parameter ν that plays the role of the chemical potential of cell aggregation. In the limit of vanishing attachment potential, $\nu \to 0$, the growth process resembles the one in diffusion-limited aggregation (Witten & Sander, 1981). However, the aggregates comprise spatially extended cells of particles rather than single particles.

As mentioned in the Introduction, planar graphs are a special class of graph that can be embedded in a Euclidean plane. A graph is planar *iff it does not contain a subdivision of* K_5 *(5-clique) and* $K_{3,3}$ *(minimal non-planar graph with 6 nodes)* (Bollobás, 1998). Consequently, planar graphs fulfill Euler's law: $N_p + N = E + 1$, which relates the number of nodes N, links E, and polygons N_p.

2.2.1 Cell Aggregation

The basic idea is to make a growing model of a planar graph with a given distribution of cell (polygon) sizes $f(n_p)$ and with degree of nodes $2 \leq k \leq 3$.

Topological constraint

For this purpose we observe some topological constraints on the distribution of cell sizes: (i) $f(n_p)$ is defined. For $n_p \geq 3$, for non-clustered graph we fix $f(3) = 0$; (ii) the planar graph obeys Euler's law: $N_p + N = E + 1$. Among these the homogeneous plane-filling structures are of special interest (Stavans, 1993). For this class of graphs the majority of nodes are in the interior of the graph, ie., nodes with degree $k = 3$. Therefore $3N \approx 2E$ and Euler's law becomes

$$6N_p = 2E + 6. \tag{2.2}$$

For a large system with a distribution of cell sizes $f(n_p)$ we have

$$N = N_p \sum_{n_p} \frac{n_p f(n_p)}{3}, \; E = N_p \sum_{n_p} \frac{n_p f(n_p)}{2}. \tag{2.3}$$

Substituting the second relation into (2.2): $6N_p = N_p \sum_{n_p} n_p f(n_p) + 6$, then for large $N_p \gg 1$ one can find that the average cell size is equal to six

$$\langle n_p \rangle \equiv \sum_{n_p} n_p f(n_p) = 6. \tag{2.4}$$

We use a lognormal distribution of polygon size

$$f(n_p) = \frac{1}{s\sqrt{2\pi}x} e^{-\frac{\ln^2 x/x_0}{2s^2}}, \tag{2.5}$$

which is most often found in experiments (Moriarty *et al.*, 2002). Using the condition (2.4) the number of independent parameters in (2.5) is reduced

$$\langle n_p \rangle = 6 \quad \Rightarrow \quad x_0 = 6e^{-s^2/2},\ s^2 = \ln\left(1 + \frac{\mu_2}{36}\right), \tag{2.6}$$

where the second central moment μ_2 remains as the control parameter in our case.

Model and Implementation

Starting from an initial cell, at each time step a new cell with size taken from the distribution $f(n_p)$ is attached to the graph boundary of the graph according to the following rules:

1. In the aggregation only nodes with degree 3 can be closed inside the graph;
2. New link can be assigned only to nodes with degree 2;
3. Potential nesting place is searched as an array of nodes on graph boundary with degree 3 limited with two nodes of degree 2. The nested part of the cell is identified with the nodes of the nesting string. Therefore, number of extra nodes to be added is $n = n_p - l$, where l is length of the nesting string. We select the nesting place with probability $p \sim e^{-\nu n}$, where the parameter ν plays the role of the chemical potential for addition of new nodes.

We implemented this algorithm in *C++* as follows:

```
Initial graph: one polygon of size np taken from f(np)
For i=2 to Np
  np = next random from distribution f(np)
  If(there is no nodes on graph boundary with degree 2) exit(1)
  For all j=(periphery node with degree 2)
    d=distance to the next node on graph boundary with degree 2
    Number of new nodes n = np-d-1
    If(n>0) p(j)=exp(-nu*n)
  End of loop j
  If(there is no j with n>0) exit(2)
  Normalize p(j)
  j = next random from distribution p(j)
  Add new polygon with size np linked with
```

```
    node j and next node on graph boundary with degree 2
End of loop i
exit(0)
```

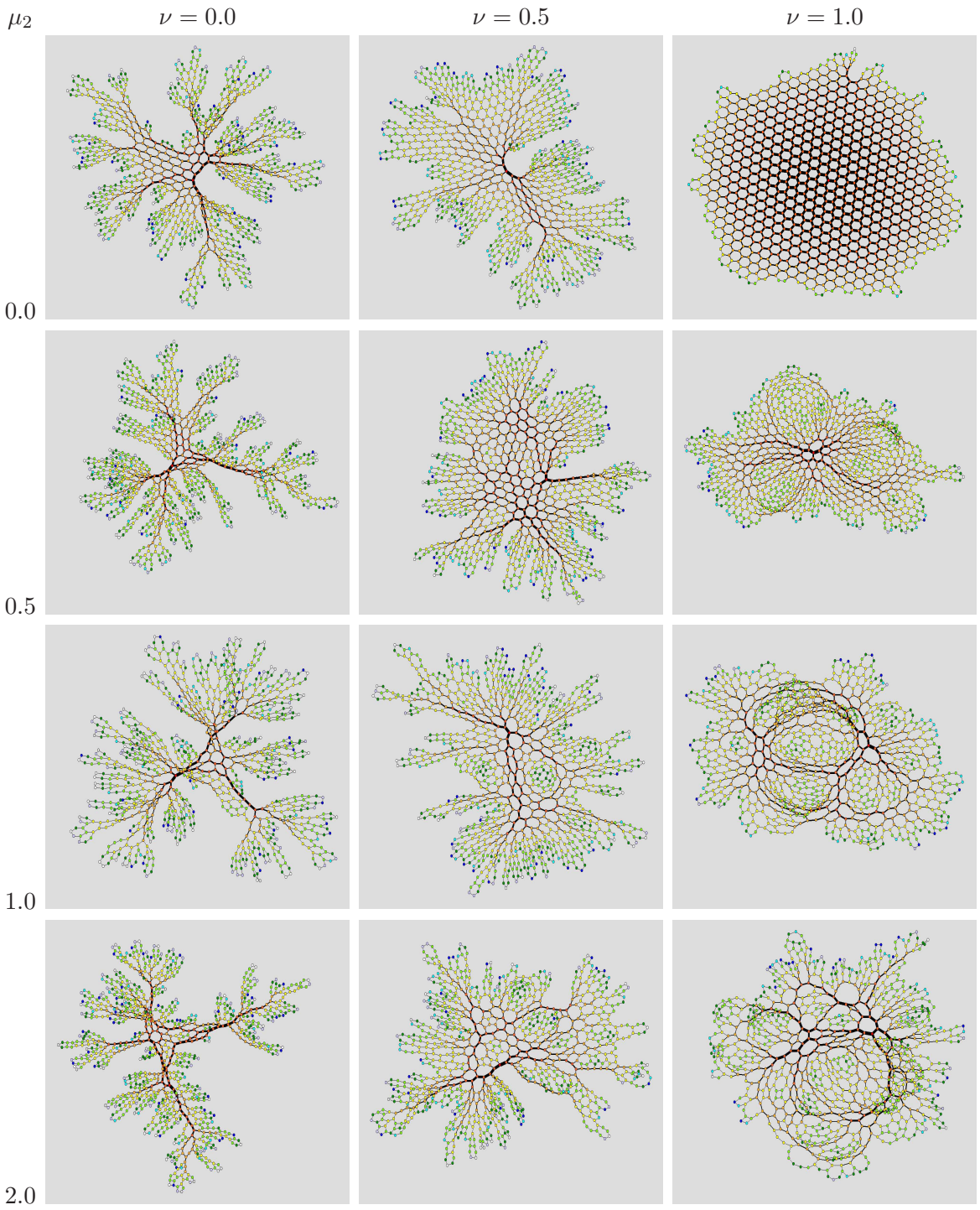

Figure 2.6: Cell-aggregated planar graphs with lognormal distribution of polygon size for various values of width μ_2 and cell aggregation potential ν. The widths of the lines are proportional to the topological betweenness (centrality) of the links.

Depending on the model parameters of the growth process and it stochasticity three possible exit cases are:

- exit(0) - Open structure (planar graph with N_p polygons);
- exit(1) - Closed structure (after some number of step there are no more nodes of degree 2 and structure stops to grow, no nesting places of any size);
- exit(2) - No nesting place available for current cell. In this case one can take next cell, which in turn perturbs the actual distribution.

We did not experience the exit(2) situation for the range of parameters $\mu_2 \in [0.5, 2.0]$, $\nu \in [0, 5]$ and $N_p = 1000$ in a very large number of samples. Two examples of the emergent open and closed structures are shown in Figure 2.5. More examples of cellular networks are shown in Figure 2.6 for varying parameters μ_2 and ν.

2.2.2 Topological Properties of Cellular Networks

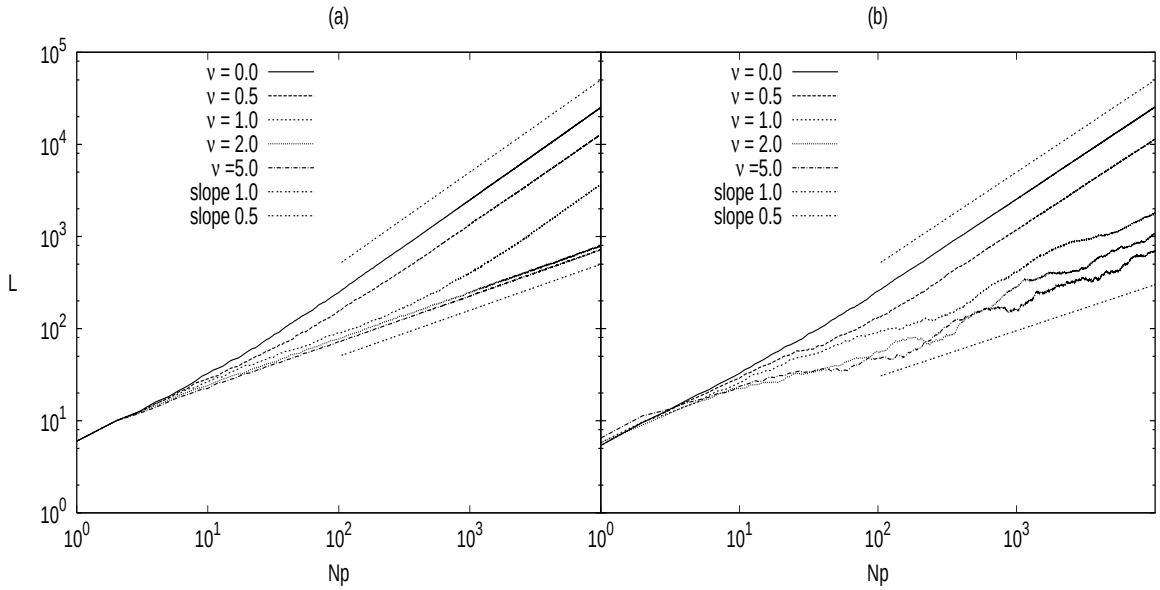

Figure 2.7: Scaling of the network perimeter (length of boundary L versus number of polygons N_p) for (a) $\mu_2 = 0$ hexagons only (b) $\mu_2 = 2.0$.

During the nesting growing process the number of nodes N increases by $n < n_p$ after one step. The number of nodes n added at each step depends on the cell size and length of the nesting

string. Therefore, $N \approx \kappa N_p$ where $\kappa = \langle n \rangle$ is the average growth rate. For open structures (see figure 2.5-2.6) boundary of the graph becomes fractal, depending on the control parameters. In fact, length of the graph boundary L grows as a power of the number of cells N_p (or network size N) with fractal dimension D defined by $L \sim N_p^D$.

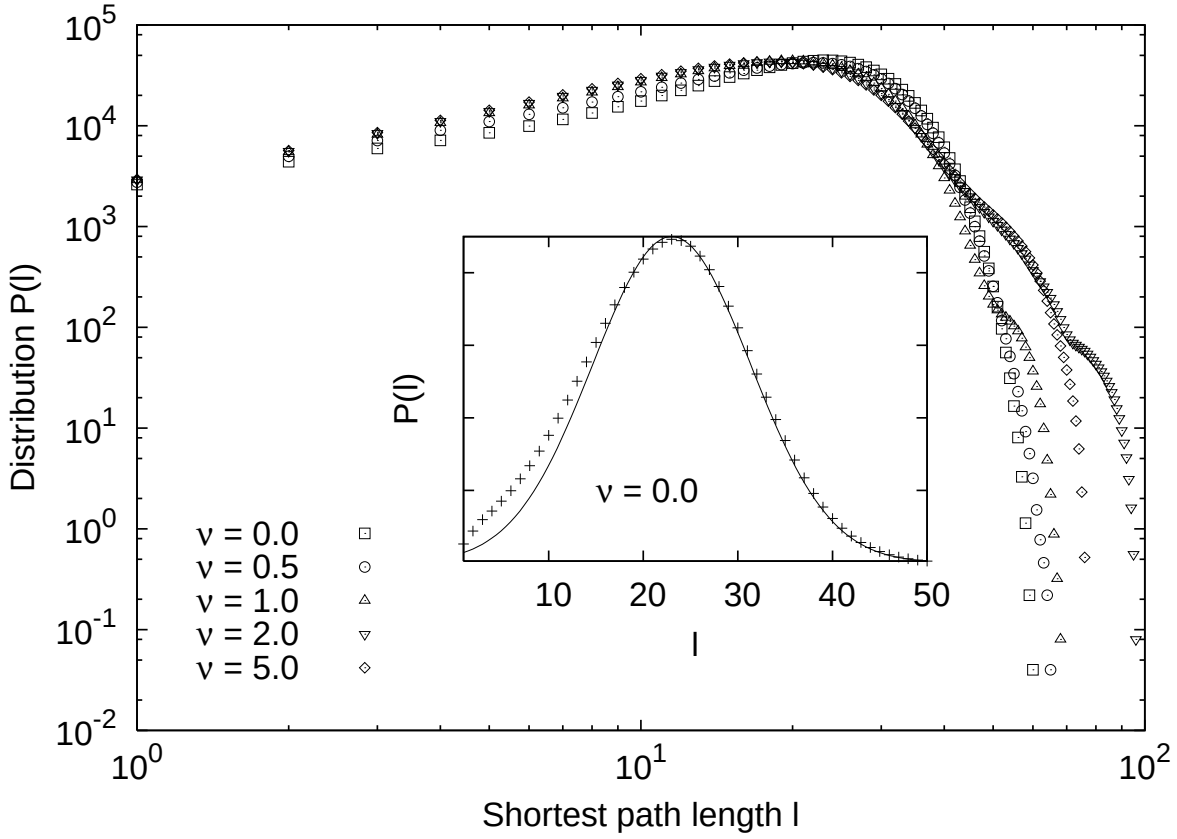

Figure 2.8: Distribution of lengths of shortest paths on networks for fixed $\mu_2 = 1.0$ and various values of ν. Insert: The distribution in the case $\nu = 0$ is shown on a linear scale. Solid line: Gaussian with $l_0 = 23$ and $\sigma = 8.37$ (Šuvakov & Tadić, 2006a).

In figure 2.7 we show how the number of nodes on the graph boundary increases with N_p. Each point is averaged over 10 emergent growing networks. The dimension D is in the range $\frac{1}{2} \leq D \leq 1$, where $D = 1$ corresponds to structures of high fractality (obtained for small values of the parameter ν). $D = \frac{1}{2}$ corresponds to planar "circle like" structures with reduced fractality. For $\mu_2 > 0$ we observe a continuous crossover between these two limits (see figure 2.7b for $\mu_2 = 2$). However, in structures with homogeneous cell distribution ($\mu_2 = 0$ - hexagons only) a

sharp transition seems to occur at $\nu_c \approx 1.5$.

Shortest path between two nodes is defined as path along the smallest number of intermediate links (Bollobás, 1998). We implemented an algorithm for counting the shortest paths of Dijksta type (Ahuja *et al.*, 1993). In figure 2.8 we show the distribution of lengths of shortest paths between all pairs of nodes on network. All networks are for fixed $\mu_2 = 1.0$ and approximately of the same size $N \approx 1000$ nodes. Each point in figure 2.8 is averaged over 100 sample networks. We found similar results for other μ_2 values.

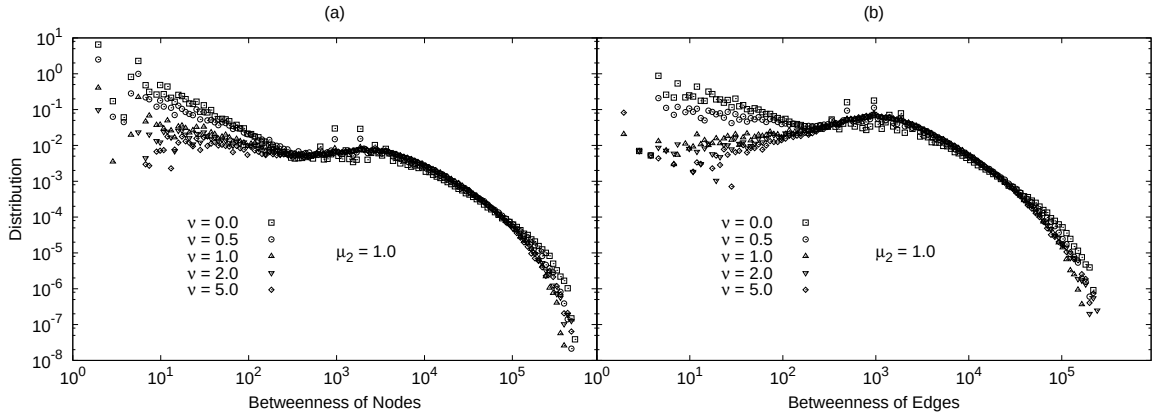

Figure 2.9: Distribution of betweenness (a) of nodes (b) of links.

All these networks have similar topology at local level, because the number of links at all interior nodes is constant $k = 3$. Therefore, the distributions of shortest distances at small scale are similar for all values of parameter ν. Differences in global topology appear at a large scale for lengths larger than a peak value $l_0 \sim 25$, and manifest in the occurrence of additional peaks (see figure 2.8). The probability of long paths increases for larger values of the parameter ν, whereas in the limit $\nu = 0$ the distribution of length of shortest paths on large scale can be approximated with a normal distribution (inset on figure 2.8).

In figure 2.9 we show distributions of betweenness of nodes and links (defined by (2.1)) averaged over 100 sample networks with fixed $\mu_2 = 1.0$ and size $N \approx 1000$ nodes.

For inhomogeneous networks, distributions of these two betweenness measures can be substantially different. In our case, however, they are similar because all interior nodes have fixed degree $k = 3$. We find that distributions at small scale strongly depend on parameter ν, which results from the graph boundary. Similar conclusions hold for other μ_2 values.

In figure 2.6 thick lines represent links with large betweenness. For this type of network the strongest lines, which make up the skeleton of the graph, connect the nodes with largest centrality measure.

2.3 Conclusions

In this chapter, two approaches to represent nanoparticle films as graphs were put forward. The first is based on the known positions of nanoparticles on the substrate. Topological properties of the two networks ($NNET1$ and $NNET2$), shortest path distribution and betweenness centrality of links were calculated. In the next chapter we will show how these properties influence charge transport. A new algorithm for the growth of graphs by an aggregation process of extended

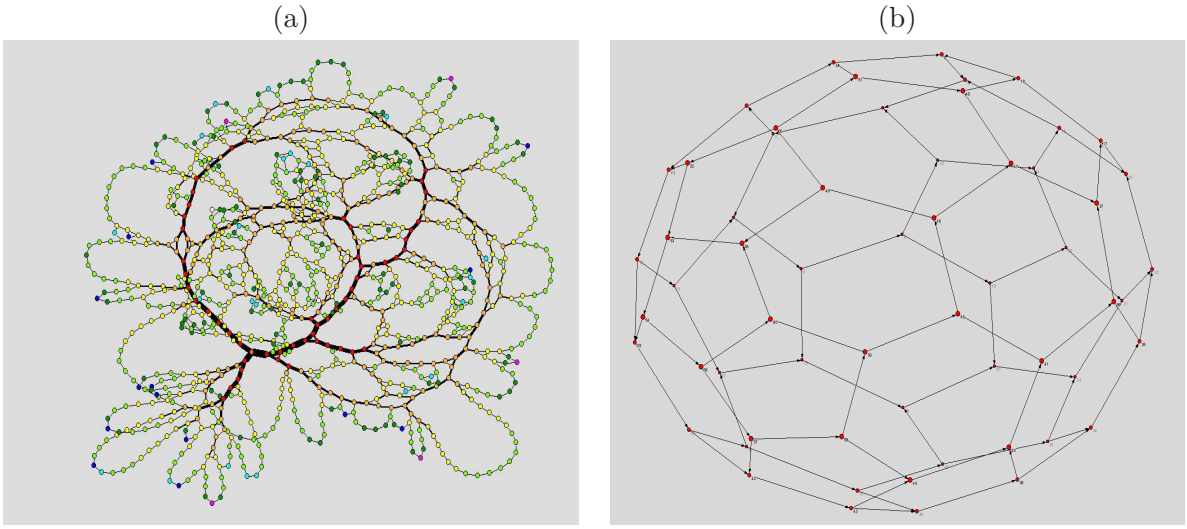

Figure 2.10: Two possible outcomes from the algorithm: (a) Scale-free distributions of loops (exponent -2.2) and $\nu = 5.0$; (b) Distributions of loops with only two sizes: fullerene like structure

objects - polygons with size distribution has also been introduced. Depending on the aggregation conditions, which are determined by two parameters controlling the distribution width and attachment potential, we can get a wide spectrum of emergent structures. We presented some results for the case of lognormal distribution of cells and additional constraints, leading to the emergent non-clustered planar graphs with a constant node connectivity. The algorithm works for a variety of cell distributions and constraints, resulting in diverse opened (fractal) or closed

structures. There are two more examples shown in Figure 2.10. In figure 2.10(a) emergent graph for power-low distribution of cell sizes is shown (exponent in the distribution is -2.2 and chemical potential $\nu = 5.0$), while in Figure 2.10(b) is shown emergent closed structure of C_{60} type. In this case we also measured several topological properties of these networks quantitatively - the fractal character of the graph boundary, shortest paths, and betweenness centrality distributions.

Chapter 3

Single Electron Conduction in Nanoparticle Films

In the Introduction and in Chapter 2 we presented different methods for assembly of nanoparticles in large-scale two-dimensional aggregates and the possibility of using graph representations to study their topology quantitatively. In this chapter we will focus on non-Ohmic conduction properties (Duruöz *et al.*, 1995; Ferry & Goodnick, 1997; Rimberg *et al.*, 1995) of metallic nanoparticle films. Under an external voltage the film behaves as a capacitively coupled system (Bakhvalov *et al.*, 1991; Middleton & Wingreen, 1993). Due to the small size, and thus small capacitance of nanoparticles, charging of a particle by a single electron increases the energy of the particle, an effect known as Coulomb blockade (Wybourne *et al.*, 1997). Hence the junction between each nanoparticle pair becomes a quantum tunneling resistor–capacitor junction. Therefore in the nanoparticle films the conduction occurs via *single-electron tunneling* through the tunneling junctions. As mentioned in the Introduction single-electron processes are highly interesting for new technologies, because of their quantized nature and the absence of thermal dissipation (Di Ventra *et al.*, 2004; Ferry & Goodnick, 1997). Conducting nanoparticle films on substrates have been investigated extensively (Blunt *et al.*, 2007c; Duruöz *et al.*, 1995; Elteto *et al.*, 2005; Moriarty *et al.*, 2002; Parthasarathy *et al.*, 2001, 2004; Rimberg *et al.*, 1995). The most striking feature of the conducting nanoparticle films is the occurrence of nonlinear current–voltage curves above the threshold voltage V_T as

$$I(V) = B\left(\frac{V - V_T}{V_T}\right)^{\zeta} \quad ; \tag{3.1}$$

The degree of the nonlinearity measured by the exponent ζ varies with the structure of the film which, in general, is strongly dependent on the way that the film has been composed. Experimentally measured values in the films on two-dimensional substrates vary in the range from $\zeta = 2.25$ (Parthasarathy *et al.*, 2004) to $\zeta = 3.9$ (Blunt *et al.*, 2007c).

The theoretical models (Bakhvalov *et al.*, 1991; Geigenmuller & Schon, 1989; Middleton & Wingreen, 1993) of conducting films with the single-electron tunnelings between capacitively coupled units have been considered mainly on the regular (triangular, square) lattices. It has been recognized that the collective behavior at the threshold voltage is related to the opening conducting paths through the system.

In this chapter we present a comprehensive study of the single-electron conduction in nanoparticle films of a general structure. Our approach is based on the network models introduced in Chapter 2. This approach gives quantitative analysis of the film topology. The emphasis is on the collective dynamic behavior underlying the nonlinear $I(V)$ curves and other scaling phenomena, and their relation to the topology of the film.

3.1 Conditions of Coulomb Blockade in Nanoparticle Systems

Let us consider a system of metallic nanoparticles arranged on a substrate, separated from each other, and nested between electrodes. When an electron tunnels from one nanoparticle or electrode to another one there is rearrangement of charge in the electrodes, resulting in a change in the electrostatic potential. For large systems this change is hardly noticeable and is associated with the *short noise* in the system (Ferry & Goodnick, 1997). In a system of very small conductors - nanoparticles, the capacitances C are small and the charging energy due to a single electron $e^2/2C$ becomes larger than thermal energy k_BT. The transfer of a single electron between conductors therefore results in voltage change which creates an energy barrier to the further transfer of electrons. This barrier remains until the charging energy is overcome by an external potential. This phenomenon is known as *single electron Coulomb blockade*.

The second constraint is that the charge is well localized on the particles. In this case we can consider tunneling within the framework of perturbation theory. If we consider the energy uncertainty relationship:

$$\Delta E \Delta t > h, \tag{3.2}$$

where $\Delta E \sim e^2/C$, and the time to transfer the charge is given by $\Delta t \sim R_t C$, where R_t is the tunnel resistance. Substituting these two expressions into (3.2), the constraint is now given by:

$$R_t \gg \frac{h}{e^2} = 25.813k\Omega. \tag{3.3}$$

Therefore, the conditions for Coulomb blockade are:

- the electrostatic energy $e^2/2C \gg$ thermal energy $k_B T$
- tunneling resistance $\gg$ quantum resistance h/e^2

At room temperature first condition is satisfied for a spherical nanoparticle with radius of the order of $R \sim 10nm$.

3.2 Physics at a Single Junction

Under the conditions of Coulomb Blockade we can consider the conduction at single junction within perturbation theory as a single electron process. The system for the transfer Hamiltonian approach (Ferry & Goodnick, 1997) is shown in Figure 3.1a. There are two systems (left l and right r) with Hamiltonians H_l and H_r which are independent of one another except for the perturbation H_t which present tunneling from one system to another. The total Hamiltonian of the system is given as the sum $H = H_l + H_r + H_t$. The Hamiltonians of the left and right side are associated with eigenvectors and eigenvalues:

$$H_l \Psi_l = E_l \Psi_l,\ H_l \Psi_l = E_l \Psi_l. \tag{3.4}$$

If we write the Hamiltonian in second quantized form:

$$H_0 = H_l + H_r = \sum_{\mathbf{k}_l} E_{\mathbf{k}_l} c^\dagger_{\mathbf{k}_l} c_{\mathbf{k}_l} + \sum_{\mathbf{k}_r} E_{\mathbf{k}_r} c^\dagger_{\mathbf{k}_r} c_{\mathbf{k}_r}, \tag{3.5}$$

$$H_t = \sum_{\mathbf{k}_l, \mathbf{k}_r} T_{\mathbf{k}_l, \mathbf{k}_r} c^\dagger_{\mathbf{k}_r} c_{\mathbf{k}_l} + \sum_{\mathbf{k}_l, \mathbf{k}_r} T_{\mathbf{k}_r, \mathbf{k}_l} c^\dagger_{\mathbf{k}_l} c_{\mathbf{k}_r}, \tag{3.6}$$

where $c^\dagger_{l,r}$ and $c_{l,r}$ are the Fermion creation and annihilation operators of independent many-body state of these two systems. Two operators which represent occupation of states are $N_{\mathbf{k}_l} = c^\dagger_{\mathbf{k}_l} c_{\mathbf{k}_l}$ and $N_{\mathbf{k}_r} = c^\dagger_{\mathbf{k}_r} c_{\mathbf{k}_r}$. For finite temperature the expectation value of $N_{\mathbf{k}_l}$ and $N_{\mathbf{k}_l}$ is given by the Fermi-Dirac distribution:

$$\left\langle N_{\mathbf{k}_{l,r}} \right\rangle = f(E_{\mathbf{k}_{l,r}}) = \frac{1}{1 + e^{(E_{\mathbf{k}_{l,r}} - E_F^{l,r})/k_B T}}. \tag{3.7}$$

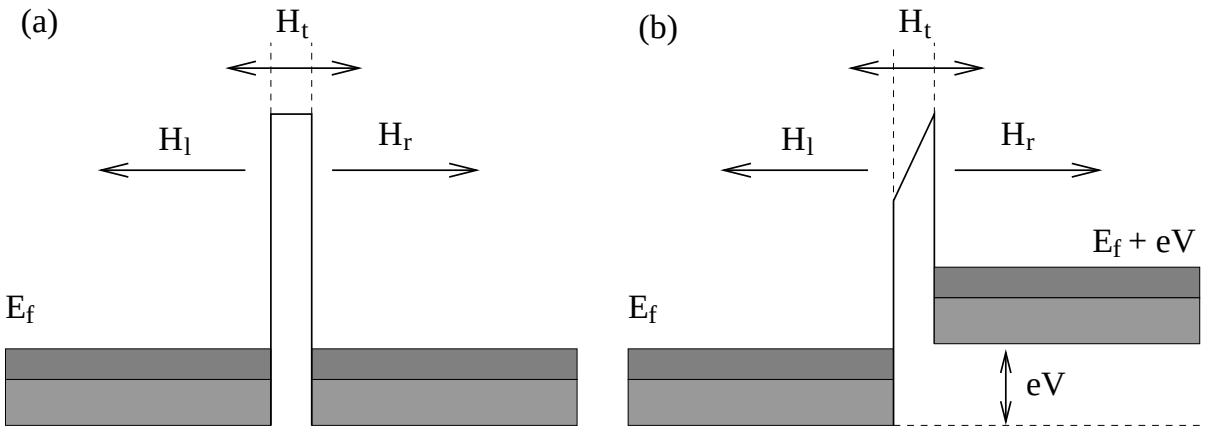

Figure 3.1: System with single barrier between two nanoparticles without (a) and with (b) external potential V.

Now we consider tunneling within the single electron picture in the case when a constant voltage is applied to the right side relative to the left (figure 3.1b). We assume that the systems remain approximately in thermal equilibrium, so the one-particle distributions are still in the same form (3.7) with different Fermi energies $E_F^r - E_F^l = eV$. The transition rate from an initial state $\mathbf{k}_l$ to final state $\mathbf{k}_r$ is treated as a scatterning process using Fermi's golden rule which gives the total tunneling rate as sum over all $\mathbf{k}_l$ and $\mathbf{k}_r$:

$$\Gamma^+(V) = \frac{2\pi}{\hbar} \sum_{\mathbf{k}_l,\mathbf{k}_r} |T_{\mathbf{k}_l,\mathbf{k}_r}|^2 f(E_l)(1 - f(E_r))\delta(E_l - E_r), \tag{3.8}$$

where the matrix elements of the tunneling Hamiltonian are given by $T_{\mathbf{k}_l,\mathbf{k}_r} = \langle \mathbf{k}_r | H_t | \mathbf{k}_l \rangle$. For relatively high barrier it is usually a good approximation to treat tunneling matrix elements as a constant T. Also the sum over momenta can be converted to a sum over energy. Since the main contribution from the sum is for a range of energies around the Fermi energy we can treat the densities of states as constant D_{l0} and D_{r0}. After one integration the expression for tunneling rate becomes:

$$\Gamma^+(V) = \frac{2\pi}{\hbar} |T|^2 D_{l0} D_{r0} \int_{E_{cm}}^{\infty} \mathrm{d}E f(E - E_F^l)[1 - f(E - E_F^r)], \tag{3.9}$$

where E_{cm} is the higher of two minimal conduction energies. The same calculations can be done for the tunneling rate in other direction and the current written as:

$$I(V) = e[\Gamma^-(V) - \Gamma^+(V)] = \frac{2\pi e}{\hbar} |T|^2 D_{l0} D_{r0} \int_{E_{cm}}^{\infty} \mathrm{d}E [f(E - E_F^r) - f(E - E_F^l)]. \tag{3.10}$$

Choosing the Fermi energy on the right as the zero of energy, then $E_F^l = -eV$. In the limit when the minimum energy is far below the Fermi energy, the integral can be solved analytically:

$$\lim_{E_{cm}\to-\infty} \int_{E_{cm}}^{\infty} \mathrm{d}E[f(E) - f(E+eV)] = eV. \tag{3.11}$$

Therefore, the I-V characteristic of a single tunnel junction is Ohmic:

$$V = IR_t, \;\; R_t = \frac{\hbar}{2\pi e^2 \left|T\right|^2 D_{l0} D_{r0}}, \tag{3.12}$$

where R_t plays the role of resistance and this constant is known as the *quantum tunneling resistance*.

Now, we will consider the generalization of the transition rates for the system of nanoparticles. We can describe the state of the system with number of a electrons on each particle $\{n\} \equiv \{n_1, n_2, ..., n_N\}$. With generalization of the analysis for the N-nanoparticle system, we can write the change in energy before and after tunneling process through $i \to j$ junction as:

$$\Delta E_{i\to j} = E\{n_1, n_2, ..., n_i - 1, ..., n_j + 1, ..., n_N\} - E\{n_1, n_2, ..., n_i, ..., n_j, ..., n_N\}. \tag{3.13}$$

Using the golden rule approximation the tunneling rate through this junction can be written:

$$\Gamma_{i\to j}(V) = \frac{2\pi}{\hbar} \sum_{\mathbf{k}_s, \mathbf{k}_f} \left|T_{\mathbf{k}_s,\mathbf{k}_f}\right|^2 f(E_s)(1 - f(E_f))\delta(E_s - E_f + \Delta E_{i\to j}), \tag{3.14}$$

where s and f refer to initial and final state of nanoparticle system. Again assuming the same approximations the tunneling rate becomes:

$$\Gamma_{i\to j}(V) = \frac{1}{e^2 R_{t,i\to j}} \int_{E_{cm}}^{\infty} \mathrm{d}E f(E)[1 - f(E + \Delta E_{i\to j})], \tag{3.15}$$

where $R_{t,i\to j}$ is given by (3.12) for junction $i \to j$. Using the property of Fermi function:

$$f(E)[1 - f(E + \Delta E_{i\to j})] = \frac{f(E) - f(E + \Delta E_{i\to j})}{1 - e^{-\Delta E_{i\to j}/k_B T}}, \tag{3.16}$$

integral (3.15) can be solved using (3.11):

$$\Gamma_{i\to j}(V) = \frac{1}{eR_{t,i\to j}} \frac{\Delta E_{i\to j}/e}{1 - e^{-\Delta E_{i\to j}/k_B T}}. \tag{3.17}$$

The equation (3.17) gives the tunneling rate under conditions of Coulomb blockade. In other cases there is different functional dependence of tunneling rate on energy change. Other processes contributing a single junction can be included through the tunneling resistance R which

in general depend on material, size, shape of nanoparticle but also on temperature (Wernsdorfer *et al.*, 1997), external magnetic field (Guéron *et al.*, 1999), distance between nanoparticles (Bezryadin *et al.*, 1997). In our model we consider the tunneling resistances as model parameters. Generally, the tunneling conductance falls off exponentially with the distance between nanoparticles (Bezryadin *et al.*, 1997).

To illustrate the Coulomb blockade effect we will consider a system of one single nanoparticle on substrate between two metallic electrodes. Two tunneling junction between electrodes and nanoparticle we describe by corresponding capacitances C and tunneling resistance R_t. The substrate (gate electrode) is at a potential V_g and it is coupled via a nanoparticle through a capacitor C_g (we assume that there is tunneling junction between nanoparticle and substrate with infinite tunneling resistance). The scheme is shown on figure 3.2. The potential of the first electrode is V while the second is at zero potential.

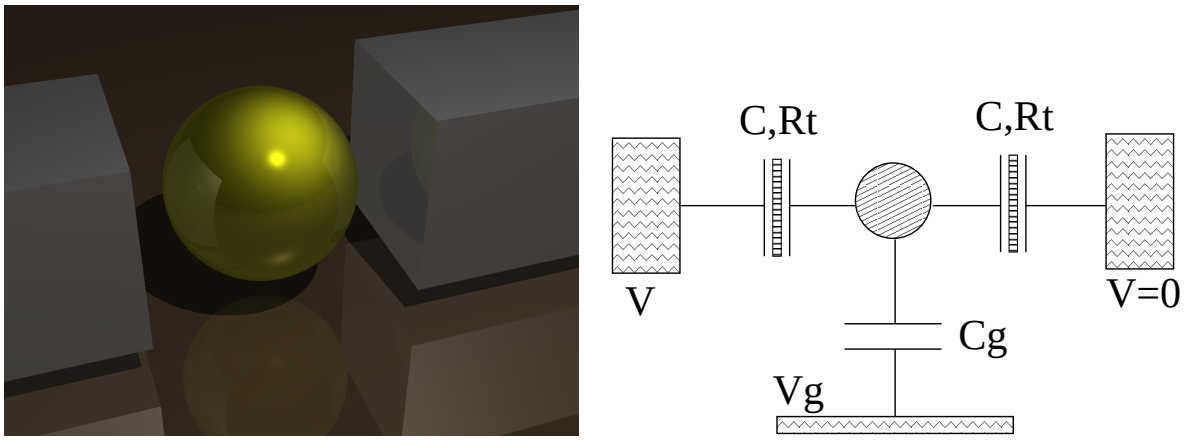

Figure 3.2: Single nanoparticle on substrate between two electrodes (left) and the equivalent circuit (right).

For this circuit the charges are given by:

$$Q_1 = C(\Phi - V),\ Q_2 = C\Phi,\ Q_g = C_g(\Phi - V_g), \tag{3.18}$$

where Φ is the potential of the nanoparticle. During the tunneling process there is an integer number of electrons accumulated on nanoparticle n. Then the charge of nanoparticle $Q = -ne$ is:

$$Q = Q_1 + Q_2 + Q_g = C(2\Phi - V) + C_g(\Phi - V_g). \tag{3.19}$$

From equation (3.19) we can find the potential of a nanoparticle:

$$\Phi = \frac{Q + CV + C_g V_g}{2C + C_g} \tag{3.20}$$

Using (3.20) and $E = \int \Phi(Q) dQ + E_e$, where E_e is energy of electrodes, we can write the electrostatic energy of the system as a function of the number of electrons on the nanoparticle:

$$E = \frac{Q^2/2}{2C + C_g} + \frac{Q(CV + C_g V_g)}{2C + C_g} + n^l eV, \tag{3.21}$$

where n^l is the number of electrons on the left electrode. Therefore the energy change for the tunneling process from the first electrode is:

$$\Delta E_1^+ = \frac{Qe}{2C + C_g} + \frac{e^2/2}{2C + C_g} + \frac{CV + C_g V_g}{2C + C_g} e - eV, \tag{3.22}$$

and the energy change due to tunneling process from the nanoparticle to the second electrode is:

$$\Delta E_2^+ = -\frac{Qe}{2C + C_g} + \frac{e^2/2}{2C + C_g} - \frac{CV + C_g V_g}{2C + C_g} e. \tag{3.23}$$

If we assume that the system is at zero temperature and that $\Delta E_{1,2}^+ < 0$ using (3.17) we have tunneling rates:

$$\Gamma_{1,2} = -\Delta E_{1,2}^+ / Re^2, \tag{3.24}$$

where R is the tunneling resistance (same for both junctions). Equilibrium will be attained when $\Gamma_1 = \Gamma_2$. If we set the gate potential to zero, $V_g = 0$, the charge on the nanoparticle is given by:

$$Q = \frac{C_g V}{2} \tag{3.25}$$

and the I-V characteristics of single nanoparticles can be written:

$$I(V) = \frac{-\Delta E_{1,2}^+}{Re} = \frac{V}{2R} - \frac{e}{R(C_g + 2C)}. \tag{3.26}$$

Therefore, in the case of one nanoparticle we found linear Ohmic conduction. This result will be used for one of the benchmark calculations in section “Numerical Implementation”.

3.3 Electrostatic Energy of an Nanoparticle Array

The generalization of the expression for charges on nanoparticles (3.19) for a NP array is given by

$$Q_i = \sum_j C_{ij}(\Phi_i - \Phi_j) + \sum_\mu C_{i,\mu}(\Phi_i - \Phi_\mu), \tag{3.27}$$

where Q_i and Φ_i are the charge and potential of ith nanoparticle, C_{ij} is the capacitance between ith and jth nanoparticle, $C_{i,\mu}$ is the capacitance between ith nanoparticle and electrode $\mu \in \{+, -, gate\}$, and Φ_μ is the potential of electrode μ. This system of equations can be written in matrix form and solved for Φ:

$$\mathbf{Q} = M\Phi - \mathbf{C}_\mu\Phi^\mu \rightarrow \Phi = M^{-1}\mathbf{Q} + M^{-1}\mathbf{C}_\mu\Phi^\mu, \tag{3.28}$$

where M is capacitance matrix given by:

$$M_{ij} = \delta_{i,j}(\sum_k C_{ik} + \sum_\mu C_{i,\mu}) - C_{ij}. \tag{3.29}$$

Then, the energy of the system can be written as (Geigenmuller & Schon, 1989; Middleton & Wingreen, 1993):

$$E = \frac{1}{2}\mathbf{Q}^\dagger M^{-1}\mathbf{Q} + \mathbf{Q}\cdot V^{ext} + Q_\mu\Phi^\mu, \quad V^{ext} = M^{-1}\mathbf{C}_\mu\Phi^\mu, \tag{3.30}$$

where Q_μ is charge on electrode μ.

If we assume a system of nanoparticles given by a graph (network) where all capacitances between two neighboring nanoparticles are the same (C) we can express the capacitance matrix as a function of the adjacency matrix A_{ij} of the structure: $M_{ij} = \delta_{i,j}(\sum_k CA_{ik} + \sum_\mu C_{i,\mu}) - CA_{ij}$.

In order to calculate energy changes for all links we perform the following calculations. After a single electron tunneling process from dot a to dot b ($Q_i' = Q_i + \delta_{bi} - \delta_{ai}$), the change of the first energy term $\Delta E^{(1)}(a \rightarrow b) = E^{(1)'} - E^{(1)}$ can be written as:

$$\Delta E^{(1)}(a \rightarrow b) = \frac{1}{2}\sum_{ij}(Q_i + \delta_{bi} - \delta_{ai})M_{ij}^{-1}(Q_j + \delta_{bj} - \delta_{aj}) - \frac{1}{2}\sum_{ij} Q_i M_{ij}^{-1} Q_j \tag{3.31}$$

Using $M_{ij}^{-1} = M_{ji}^{-1}$ (3.31) becomes:

$$\Delta E^{(1)}(a \rightarrow b) = \sum_i Q_i(M_{ib}^{-1} - M_{ia}^{-1}) + \frac{1}{2}(M_{aa}^{-1} + M_{bb}^{-1} - M_{ab}^{-1} - M_{ba}^{-1}) \tag{3.32}$$

Similarly, the change of the second energy term $\Delta E^{(2)}(a \to b) = E^{(2)'} - E^{(2)}$ in this case is:

$$\Delta E^{(2)}(a \to b) = \sum_i (Q_i + \delta_{bi} - \delta_{ai}) V_i^{ext} - \sum_i Q_i V_i^{ext} = V_b^{ext} - V_a^{ext}. \tag{3.33}$$

There is also tunneling processes between electrodes and dots. After a tunneling process between electrode and dot a ($Q_i' = Q_i \pm \delta_{ai}$) the energy changes of the two terms are:

$$\begin{aligned} \Delta E^{(1)}(a \leftrightarrow \pm) =& \frac{1}{2} \sum_{ij} (Q_i \pm \delta_{ai}) M_{ij}^{-1} (Q_j \pm \delta_{aj}) - \frac{1}{2} \sum_{ij} Q_i M_{ij}^{-1} Q_j \\ =& \pm \sum_i Q_i M_{ia}^{-1} + \frac{1}{2} M_{aa}^{-1}, \end{aligned} \tag{3.34}$$

and

$$\Delta E^{(2)}(a \leftrightarrow \pm) = \sum_i (Q_i \pm \delta_{ai}) V_i^{ext} - \sum_i Q_i V_i^{ext} = \pm V_a^{ext}. \tag{3.35}$$

If we denote $V_c = \sum_i Q_i M_{ic}^{-1}$, (3.31) and (3.34) become:

$$\Delta E^{(1)}(a \to b) = V_b - V_a + \frac{1}{2}(M_{aa}^{-1} + M_{bb}^{-1} - M_{ab}^{-1} - M_{ba}^{-1}), \tag{3.36}$$

$$\Delta E^{(1)}(a \leftrightarrow \pm) = \pm V_a + \frac{1}{2} M_{aa}^{-1}. \tag{3.37}$$

The new V_c' after the tunneling process can be calculated from old:

$$a \to b: \quad V_c' = V_c + M_{bc}^{-1} - M_{ac}^{-1}, \tag{3.38}$$

$$a \leftrightarrow \pm: \quad V_c' = V_c \pm M_{ac}^{-1}. \tag{3.39}$$

If we know V_c we do not need to calculate the sum every time when we calculating the change of energy . After any tunneling process we can update V_c.

In our model we take the same capacitance C_g between all nanoparticles and the substrate (gate electrode) $C_{i,gate} = C_g$. Also, the capacitances between two other electrodes and nanoparticles connected with them is the same as interparticle capacitance C. In the limit when $C \ll C_g$ diagonal elements of the capacitance matrix M are much larger than offdiagonal elements. Therefore the off-diagonal elements of inverse matrix M^{-1} fall off exponentially and in calculations of V_c in (3.38) and (3.39) we can use only neighboring terms.

In our numerical model (see section "Implementation") to compute the energy changes we will systematically refer to the equations (3.33) and (3.36) for the process ($a \to b$) and (3.35) and (3.37) for the process ($a \to \pm$).

3.4 Numerical Model of the Conduction

Our implementation of the conduction model is based on the calculation shown in Section 3.3. We start from an arrangement of nanoparticles given by an adjacency matrix and connections with electrodes which are included in capacitance vectors $\mathbf{C}_\mu$. We assume that at $t = 0$ system of nanoparticles are not charged (we set Q_i to zero) and that there is constant potential on electrodes Φ_μ. During the initialization we calculate inverse capacitance matrix M and vector V_{ext}.

The algorithm is based on discrete steps where each step corresponds to a tunneling event. In each step we calculate the energy change for every junction $i \to j$ (where i or j includes electrodes) using the procedure defined in 3.3. From this energy change we can calculate the tunneling rate for that tunneling process Γ_{ij}. The tunneling rate defines the tunneling time distribution. In the case when tunneling rate is constant in time, the probability density function of tunneling times is given by:

$$f_{ij}(t) = \Gamma_{ij} e^{-\Gamma_{ij} t}. \tag{3.40}$$

and we can generate a random number from this distribution as an inverse cumulative distribution function of uniform random number u from interval $(0, 1)$. First, we calculate the cumulative distribution:

$$F_{ij}(t) = 1 - e^{-\Gamma_{ij} t}. \tag{3.41}$$

and solve equation $F_{ij}(t_{ij}) = u$ for t. This gives:

$$t_{ij} = -\frac{\log(1-u)}{\Gamma_{ij}}. \tag{3.42}$$

In general the case Γ_{ij} is not constant in time (when some tunneling process has happened, the tunneling rate is changed). In this case the density and cumulative distribution of tunneling times are given by:

$$f_{ij}(t) = \Gamma_{ij}(t') e^{-\int_0^t \Gamma_{ij}(t')\mathrm{d}t'},\ F_{ij}(t) = 1 - e^{-\int_0^t \Gamma_{ij}(t')\mathrm{d}t'}, \tag{3.43}$$

and the equation $F_{ij}(t_{ij}) = u$ becomes:

$$\int_0^{t_{ij}} \Gamma_{ij}(t')\mathrm{d}t' = -log(1-u). \tag{3.44}$$

In our case tunneling rates are part by part constant functions. Therefore we can convert the integral (3.44) into sum over time intervals between two successive tunnelings. According to

this, we use the following algorithm: At the beginning we assign one random number u_{ij} from the uniform $(0, 1)$ distribution to every junction. Then in each step we solve equations (3.44) using:

$$\Delta t_{ij} = \frac{-log(1-u_{ij}) - \sum'_{\Delta t_k} \Delta t_k \Gamma_{ij}(t_k)}{\Gamma_{ij}(t)}, \tag{3.45}$$

where Δt_{ij} is the time to the next tunneling event, Δt_k are intervals between two successive tunnelings in the system with corresponding tunneling rates $\Gamma_{ij}(t_k)$. After this we find the junction with minimal t_{ij}, and we process the tunneling by updating the vectors $\mathbf{Q}$, $\mathbf{V}_c$. In addition we assign new random number u_{ij} to the junction on which the tunneling process has occured.

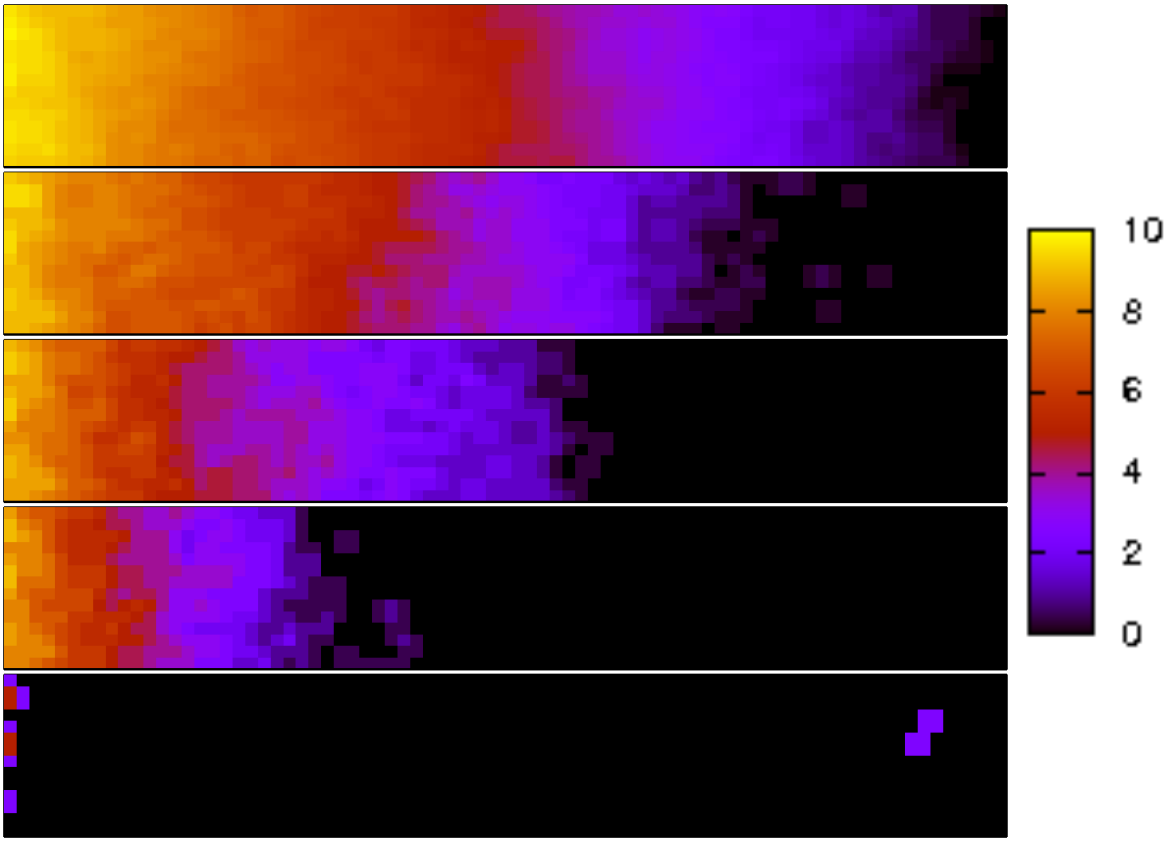

Figure 3.3: Triangular nanoparticle network with charge disorder: moving of charge front for different voltages. Colors represent charge on nanoparticles.

In this stochastic algorithm electrons start to enter into the system of nanoparticles. The

number of electrons on nanoparticles is growing in time depending on the driving voltages on the electrodes. After some relaxation period the mean number of electrons on each nanoparticle become constant with random fluctuations. For small voltages there are nanoparticles without electrons (near to the positive electrode). The electrons which have entered the system comprise a charge "front" between electrodes. When we increase the voltage, the front moves in the direction of the positive electrode and after some critical (threshold) voltage between the electrodes, front arrive to the positive electrode.In this case, even if the mean values of charges remains constant a current appears. The current is calculated by sampling the number of electrons which arrive on positive electrode in some time window after the relaxation process. The moving front of charges on slabs of regular triangular array of nanoparticles is shown in Figure 3.3 for a set of different voltages. The color intensity indicates the number of electrons at the nanoparticles.

Schematically, the main steps in the algorithm are:

```
Input: graph, parameters
Calculate capacitance and inverse capacitance matrix
Initialize vectors Q, Vc, V+  with zeros
Initialize time t=0
While(V+ < V_{max})
While(enough sampled data)
  Calculate vector Vc
  Calculate energy change for all junctions
  For each link
    t(i,j)=next random from distribution pij(t)
  End For
  Process the tunneling with smallest time t(i,j)
  Increment time t=t+t(i,j)
  If(relaxation is done)
    Sample data of interest
  End If
End While
Increase V
End While
```

In the case when $C \ll C_g$ the off-diagonal elements of the inverse capacitance matrix fall of exponentially and can be neglected. Therefore, we have computational acceleration because we need to calculate only V_c in (3.38) with the neighboring indices.

We use LU decomposition to calculate the inverse capacitance matrix. This algorithm require N^3 computational steps, where N is size of matrix, in our case number of nanoparticles. The rest of the code require N^2 operations per each tunneling process. Therefore, algorithm complexity is $O(N^3 + MN^2)$ where M denote number of processed tunneling events. In the described case when $C \ll C_g$ algorithm require $O(N)$ operations per each tunneling, and complexity of the whole algorithm is given by $O(N^3 + MN)$.

Usually there are charge impurities in real nanoparticle systems. The effect of impurities can be included in our model by assigning random offset charges q_i ($0 \leq q_i < e$) to each nanoparticle. We take q_i randomly from a uniform distribution and fix them a constant during the simulations (quenched charge disorder). The effective charge of each nanoparticle is given by the number of electrons on it and the random charge q_i. Therefore, in all equations (3.31-3.39) we need to replace Q_i with $Q_i + q_i$. As we will see later, the charge disorder have large influence on the nonlinearity of the conduction.

Temperature effects are included through the expression for the tunneling rate (3.17). In this chapter we will present only results at zero temperature $T = 0$. In this case (3.17) can be simplified in the limit $k_B T \to 0$ and it becomes:

$$\Gamma_{i\to j}(V) = \frac{1}{e^2 R_{t,i\to j}} \Delta E_{i\to j}. \tag{3.46}$$

Many other effects can be also included into the model. For instance, local variations in compositions will result in different capacitances C_{ij} and in different tunneling resistances $R_{t,i\to j}$ through each junction. In order to find effects of local variations in the composition, one can put a random distribution of these values assigned to each tunneling junction. Furthermore the functional dependence of the tunneling rate on the energy change (3.46) is not necessarily linear; it can be modeled by some other functional dependence given empirically or from theory for a given system.

3.5 Current–Voltage Characteristics

3.5.1 Benchmarks and Regular Structures

In the previous session we presented our implementation of the conduction model with its capabilities. In order to test our model we perform few benchmark calculations shown on figure 3.4 for conduction through one nanoparticle, $1D$ nanoparticle array, and a regular triangular lattice. In all calculations we assume that R, C, C_g are constants and that $\Phi^- = \Phi^{gate} = 0$. The

driving parameter is potential of positive electrode $\Phi^+ = V$. In addition, we fix the ratio $C/C_g = 10^{-4}$ where the condition $C \ll C_g$ is well satisfied. The capacitance between the electrodes and the neighboring nanoparticles is constant and equal to the interparticle capacitance C. The uniform-random charge disorder is also assumed.

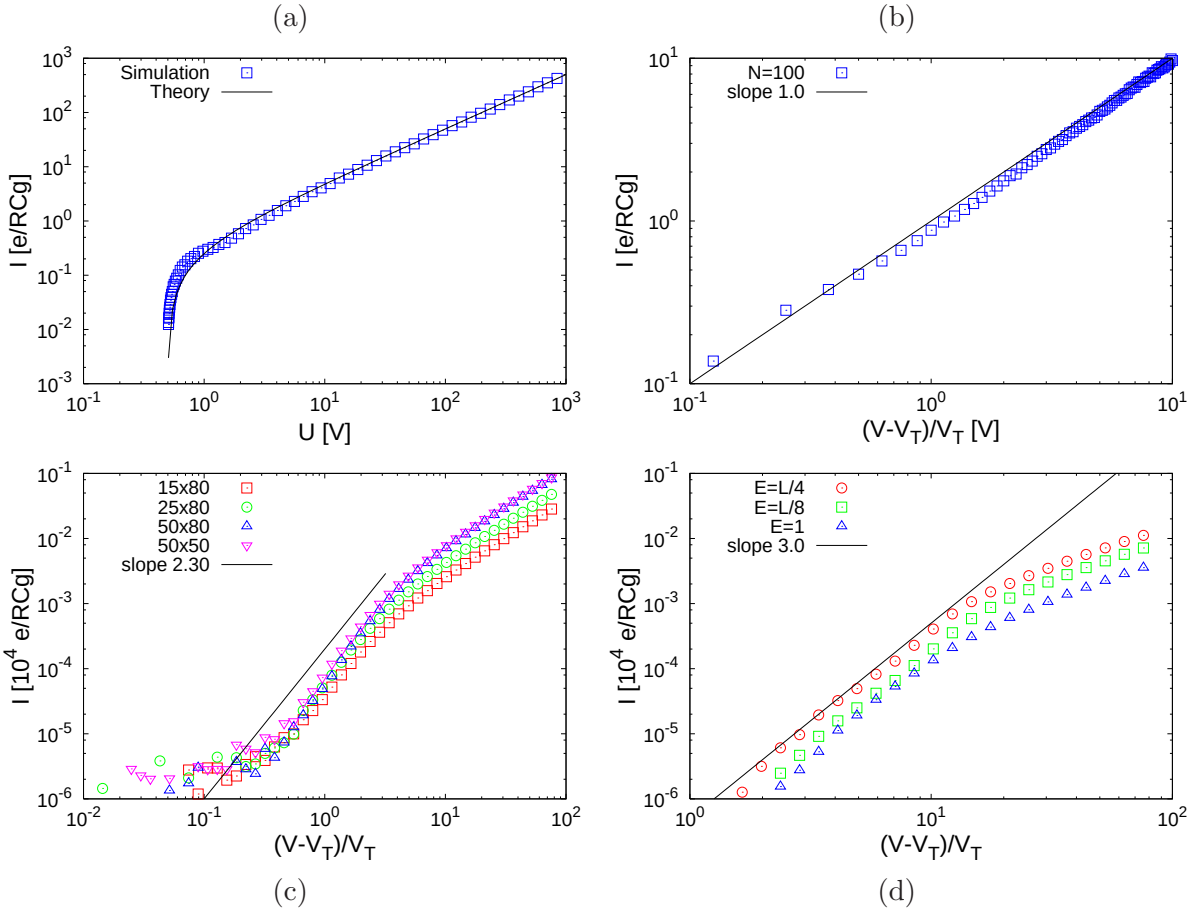

Figure 3.4: Simulated current–voltage curves for: (a) Single nanoparticle and comparison with the exact expression Eq. (3.26), (b) Linear chain of nanoparticles; (c) Regular triangular array with quenched charge disorder and comparison with experimental results of Ref. (Parthasarathy *et al.*, 2001); (d) Regular hexagonal structure.

In the case of a single nanoparticle connected with tunneling junctions to both electrodes and capacitively coupled with gate electrode as in figure 3.2, we find good agreement with theoretical prediction given by equation (3.26) (see figure 3.4a). The behavior of I-V curve in this case is linear beyond the threshold voltage.

Second benchmark calculation is conduction through $1D$ nanoparticle array. On figure 3.4b we show dependence of current I on reduced voltage $(V - V_T)/V_T$ where V_T is threshold voltage and find linear behavior in aggreament with theoretical prediction and experiments. In this case we also find that the threshold voltage is proportional to number of nanoparticles in the array N.

Figure 3.4c shows are results for regular triangular array for four different sizes of system: 15x80, 25x80, 50x80, and 50x50 (first number correspond to the system size along the electrodes and second to the perpendicular direction). This figure illustrates well typical I-V curve which is often obtained in our simulations. First, we observe noise at the small values of the reduced voltage, near the threshold voltage. This is followed by the powerlow behavior with a critical exponent ζ in a range above V_T, and saturation at large values of the reduced voltage. The system size does not appear to have strong influence on the nonlinearity exponent. In the case of triangular array with charge disorder we find $\zeta \approx 2.3$ which is in good agreement with the experiment of Ref. (Parthasarathy *et al.*, 2001).

In the case of regular hexagonal structure without random charge disorder the results are shown in figure 3.4d. Shown are the calculations for three different sizes of the electrodes: one quarter of the graph boundary, one eight part of the graph boundary, and the point-like electrodes (one node). Similar to the previous situation the nonlinear exponent does not depend on the sizes of the electrodes. The slope of I-V curve in this case is $\zeta \approx 3.0$.

3.5.2 Conduction through the Nanonetworks of a General Topology

Current-voltage characteristic for cell-aggregated networks for the case when random charge disorder is included in the calculations is shown on figure 3.5a. There are results for two different sizes of the system (1000 and 2000 nodes) and for two different sizes of electrodes (single node electrodes and electrodes wit length equal to one eight part of network boundary). All calculations are made under the same conditions as the benchmark calculations. The system size and size of electrodes do not change the exponent of nonlinearity and in this particular case it is $\zeta \approx 1.33$. In the case when random charge disorder is not included (figure 3.5b) the nonlinear exponent is much larger, and in this case we find $\zeta \approx 2.5$.

The results for the I-V characteristics of nanoparticle networks are shown in Figure 3.6. This results are obtained without imposition of random charge disorder - the topology of the network is enough to produce a scaling exponent which is in good agreement with that observed in the experiments. There is saturation in nonlinearity for voltage values above $V \approx 10V_T$. In the case

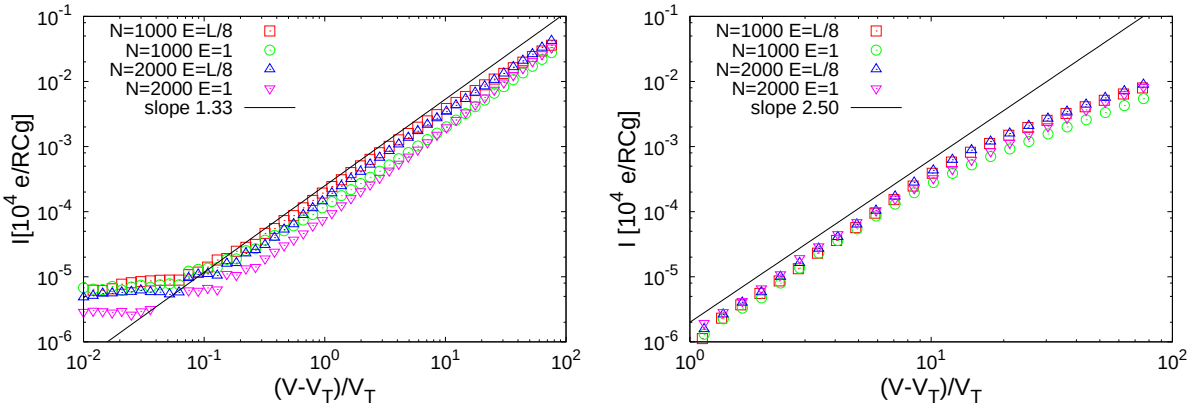

Figure 3.5: I-V characteristics for cell-aggregated nanoparticle networks: (a) calculations on cellular network with $\mu_2 = 0.5$ and with random charge disorder included in the calculations; (b) the same network without charge disorder. In both cases there are results for two different system sizes ($N = 1000$ and $N = 2000$) and two different sizes of electrodes (one node and one eighth fraction of the network boundary nodes).

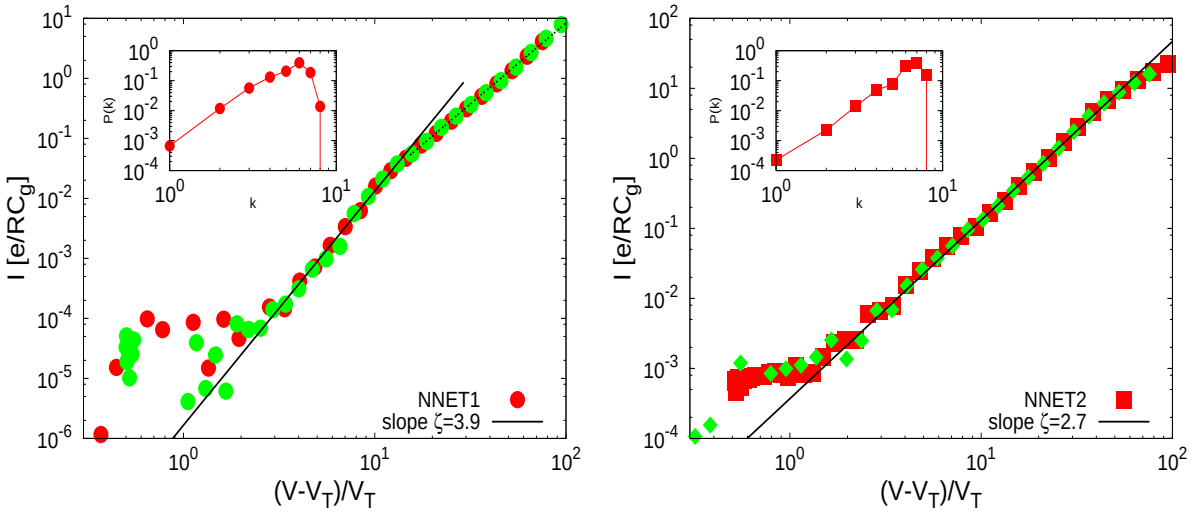

Figure 3.6: I-V characteristics for nanoparticle film networks shown in Figure 2.3: simulations for (a) $NNET1$; and (b) $NNET2$. Insets: Degree distributions of nodes for the corresponding network.

of $NNET1$ (figure 3.6a) there is strong nonlinear behavior of the current with the exponent $\zeta \approx 3.9$, which is comparable to the experimental results (Blunt *et al.*, 2007c). Figure 3.6b shows results for $NNET2$, where we obtained smaller exponent $\zeta = 2.8$, similar to the results in

the case of regular (homogeneous) structures. However, in this case saturation occurs at a value ten times larger of reduced voltage $V \approx 10V_T$. Main conclusion is that topology have important influence on nonlinear conduction. Inhomogeneities in the structure dramatically increases the nonlinear exponent in the current-voltage characteristic curve.

Geometry of Conduction Paths. In our model electrons simultaneously tunnel through the whole system. However, for voltages just below the threshold voltage, the flow of electrons is confined into a few major flow-carrying paths - conduction paths. The geometry of those paths is generally different and strongly related to the topology of the network. The number of conduction channels (paths) are increasing with increasing voltage. Understanding relation between the topology of the system and the geometry of the conduction paths gives us a better picture of the physical processes leading to the nonlinear I(V) dependence in the range of voltages above V_T.

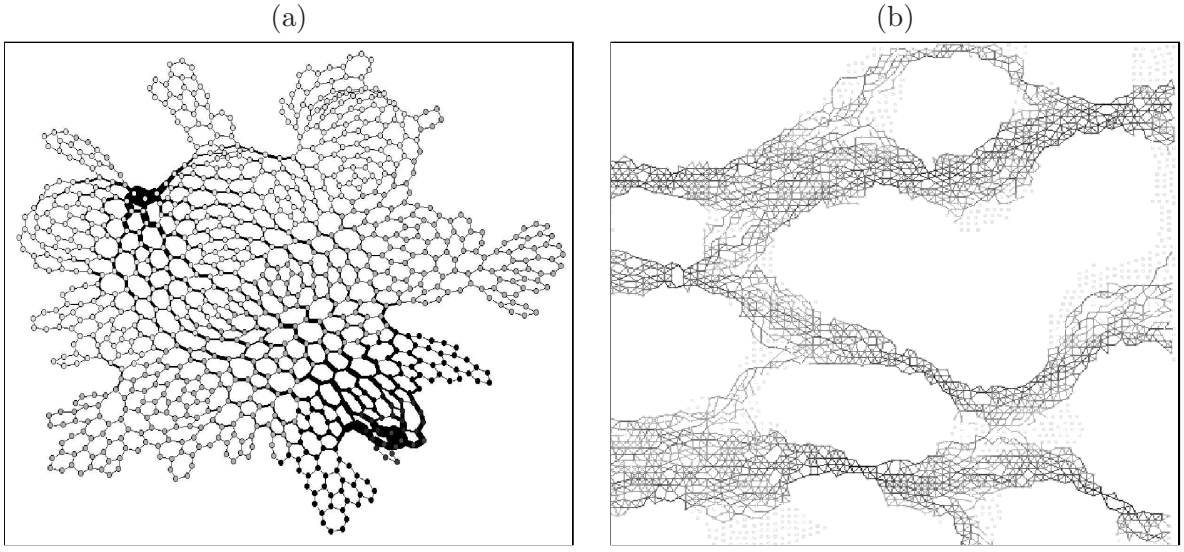

Figure 3.7: Visualization of the conduction paths through nanoparticle networks: (a) cellular network $CNET$ with point electrodes, colors indicate different voltage areas; (b) nano-network $NNET1$ with line electrodes along left and right boundary.

The shortest path between electrodes plays an important role in establishing current through the network. The distributions of shortest paths and topological flow (betweenness centrality) for cellular network $CNET$ and nano-network $NNET1$ is discused in Chapter 2. Another method for analyzing the topological flow is the construction of maximum flow spanning tree (Šuvakov

& Tadić, 2006b). This is the spanning tree, a subgraph that is a tree containing all nodes, with maximum sum of link betweenness. In order to find the local properties of charge transport

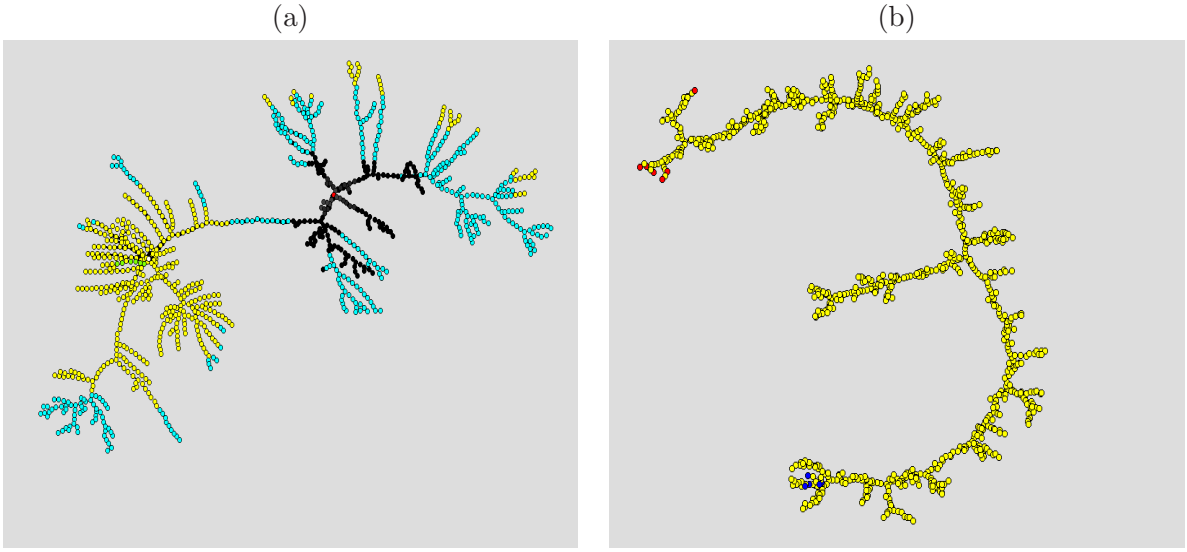

Figure 3.8: Maximum conduction flow spanning trees: (a) $CNET$ with marked different voltage areas and (b) part of $NNET1$ including the main channel, electrodes are marked with different dark colors.

we monitor the current (charge flow) through each link f_{ij}. Figure 3.7 we show how the flow is distributed along networks $CNET$ with point electrodes (Figure 3.7a) and for $NNET1$ with extended line electrodes placed along left and right graph boundary (Figure 3.7b). The line widths/brightness are proportional to flow through a link.

In Figure 3.8a we show the maximum flow spanning tree for $CNET$, defined in an analogous way to the topological spanning tree. Similarly, a dominant part of the maximum flow spanning tree for $NNET1$ is shown in Figure 3.8b).

3.6 Statistical Properties of Charge Transport

In the previous section we shown the global dynamical properties of discussed conduction via single electron tunneling through nanoparticle networks. In this section we will focus on local behavior of the dynamics. Using several statistical measures, such as, charge flow along individual junctions, activity delay and charge fluctuations on a single nanoparticle, we will investigate

local properties and long-range correlations in the system. All measures will be presented for the two example networks, $CNET$ and $NNET1$, introduced before.

Charge Flow Distribution. The charge flow $f_{i\to j}$ through links is defined as number of tunnelings from a nanoparticle i to a nanoparticle j in a given time window T_{win}. The absolute value of current for each link ij can be calculated:

$$f_{ij} \equiv |f_{i\to j} - f_{j\to i}| \,. \tag{3.47}$$

Note that the flow f_{ij} is defined between all neighboring nanoparticles, see Figure 2.3.

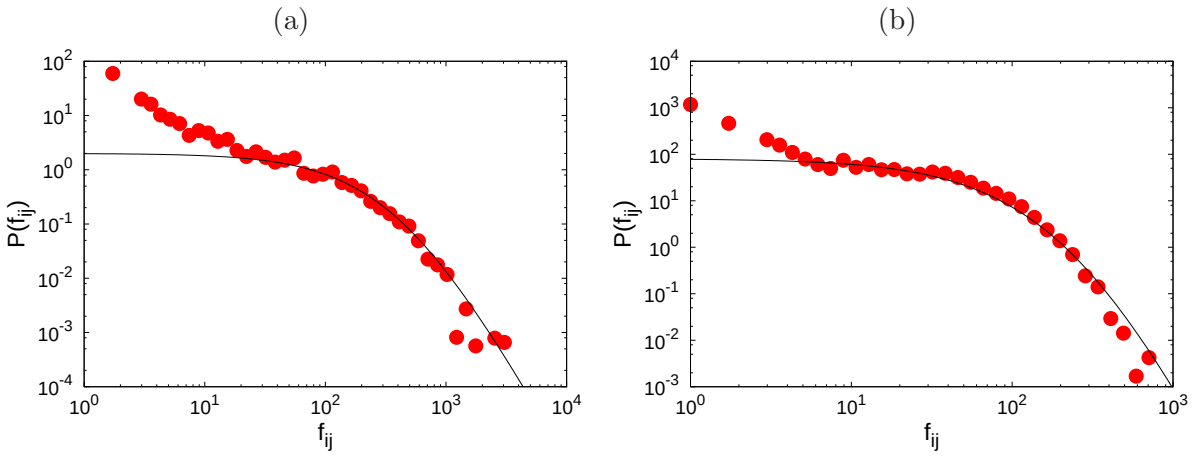

Figure 3.9: Distribution $P(f_{ij})$ of charge flow along the links (dynamic betweenness) averaged over the network and pits Fit lines according to Eq. (3.48) for (a) $CNET$: $B_q = 2$, $X_0 = 100$, $q = 1.25$; (b) $NNET1$: $B_q = 80$, $X_0 = 35$, $q = 1.14$.

We determine the flow distributions $P(f_{ij})$ for these two sample networks. Results are shown of figure 3.9. The both distributions of flow appear to have power law tails and they can be fitted with a q-exponential form, which is often found for non-ergodic behavior in dynamical systems (Tsallis, 1988):

$$P(X) = B_q \left[1 - (1-q)\frac{X}{X_0}\right]^{-1/(1-q)} . \tag{3.48}$$

The parameters for the first network $CNET$ are: $B_Q = 2$, $X_0 = 100$, and $q = 1.25$. The q-exponential form (3.48) in limit of large flow value gives a power law tail with exponent $\tau = 1/(1-q)$, and for our example it is $\tau = 4.0$. For the second network $NNET1$ parameters are: $B_Q = 80$, $X_0 = 35$, and $q = 1.14$ with corresponding exponent $\tau = 7.0$.

Return Time Statistics. One dynamical measure we studied was the statistics of return-times, defined as time intervals Δt between two successive tunnelings at a given nanoparticle. In strongly correlated dynamical systems such as earthquakes (Corral, 2004, 2005, 2006), critical sendpiles (Boguna & Corral, 1997; Sanchez & Carreras, 2002) and financial market dynamics (Lee *et al.*, 2006; Sabatelli *et al.*, 2002), the distribution of return times is found with long power law tails. Appearance of a power law tail in distributions suggests the occurrence of long-range correlations between the events.

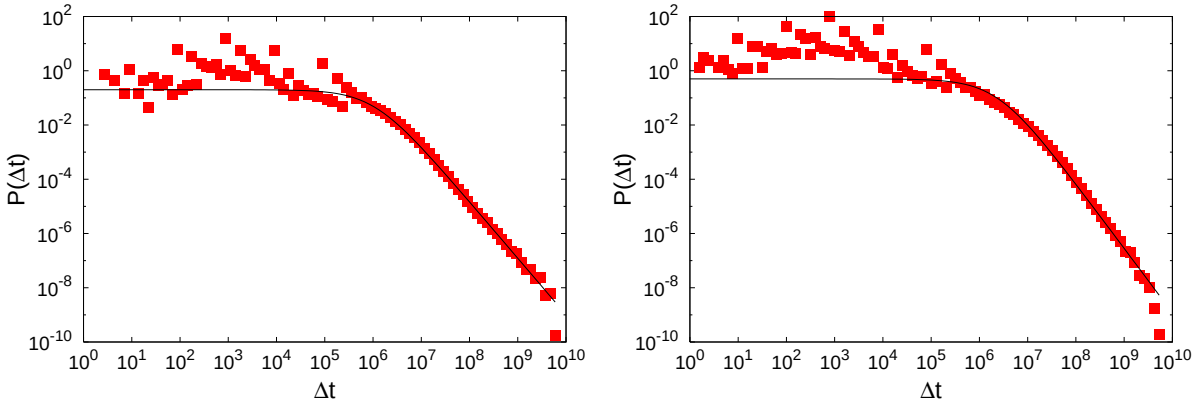

Figure 3.10: Distributions of time intervals Δt between two successive tunnelings at a node (return-times) $P(\Delta t)$, averaged over the network. Fits according to Eq. (3.48) (a) $CNET$: $B_Q = 0.2$, $X_0 = 5 \cdot 10^5$, $q = 1.48$; (b) $NNET1$: $B_Q = 0.5$, $X_0 = \cdot 10^6$, and $q = 1.4$.

Here we address the issue of return times in order to investigate the nature of collective dynamics behavior in conduction via single electron tunneling. The results are shown on figure 3.10. In both cases ($CNET$ and $NNET1$), distributions can be fitted with a q-exponential form (3.48). The parameters for first network $CNET$ are: $B_Q = 0.2$, $X_0 = 5 \cdot 10^5$, and $q = 1.48$. This value of parameter q correspond to power-low tail on large values of return time with exponent $\tau = 2.08$. For the second network $NNET$ parameters are: $B_Q = 0.5$, $X_0 = \cdot 10^6$, and $q = 1.4$ with corresponding exponent $\tau = 2.5$. In both cases results indicate presence of long-range dynamic correlations in the system. For large flow data is well fitted with q-exponential form. On small values deviations from fit are related to graph periphery, a large number of non-active nodes (see figure 3.7).

Charge Fluctuation. For both sample networks $CNET$ and $NNET1$ we simulated conduction for a voltage above threshold $V = 10V_T$ and following a relaxation period we sampled charge

fluctuation time-series. These are determined by the number of activities (tunnelings) $n_i(t)$ in a given time window T_{win} ($T_{win} = 4.11/\langle\Gamma\rangle$ for $CNET$ and $T_{win} = 17.10/\langle\Gamma\rangle$ for $NNET$) on a given typical node i in the middle of the network.

On the left hand side of series in the figures 3.11 and 3.12 one can see an example of noise on a single nanoparticle in the time and corresponding power spectrum defined as:

$$S(\nu) = \left| \sum_{j=0}^{N_s} n_j e^{i2\pi j\nu/N_s} \right|^2 \sim \nu^{-\beta}, \tag{3.49}$$

where N_s is number of time samples.

In the case of $CNET$ there is a slope larger than $\beta = 1$ suggesting weak correlations (Tadić & Thurner, 2004) between tunneling events on a nanoparticle. However, results for $NNET$ show that in the case of inhomogeneous connectivity correlation are strong on whole network $\beta = 1$ but weak locally.

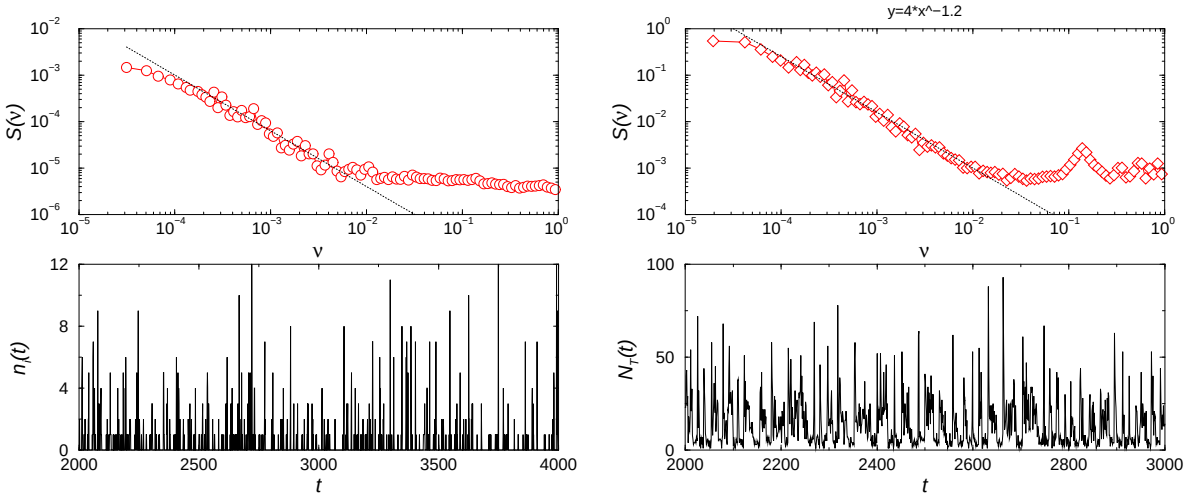

Figure 3.11: Power spectrum of fluctuations on a single node for the network $CNET$ (left) and on the whole network (right). Slopes: $\beta = 1.2$ and $\beta = 1.2$

In order to compare activity noise on single nanoparticles and on large scale, we determine the global noise N_T as the number of activities (tunnelings events) on whole network in a given time window T_{win}. The global noise $N_T(t)$ can be calculated as the sum:

$$N_T = \sum_{i=1}^{N} n_i(t). \tag{3.50}$$

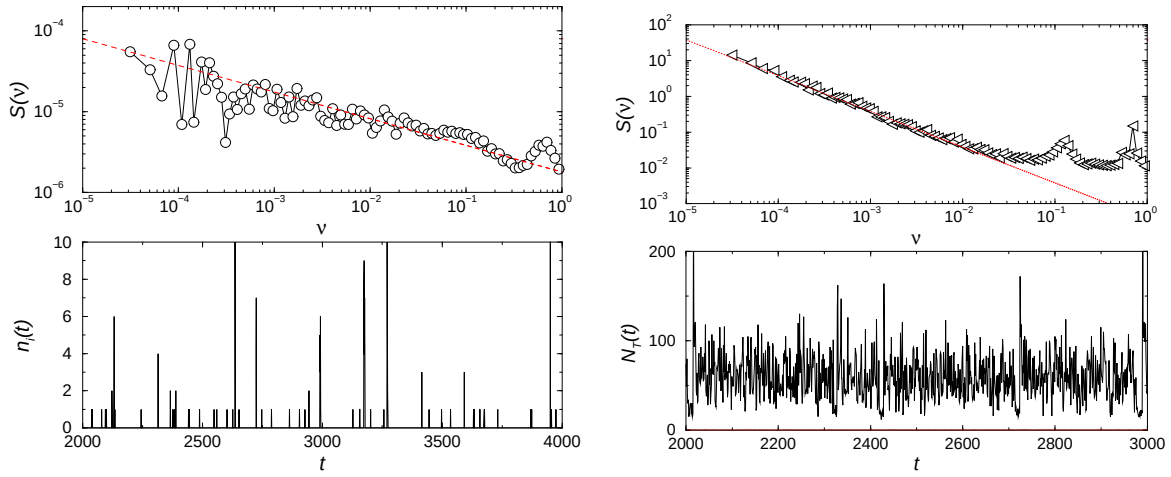

Figure 3.12: Power spectrum of fluctuations on a single node for the network $NNET1$ (left) and on the whole network (right). Slopes: $\beta = 0.33$ and $\beta = 1.0$

The power spectrum for the global noise is shown on the right hand side of figures 3.11 and 3.12. There is strong correlation in both cases comparable with $1/f$ noise usually found in dynamical systems suggesting long-range correlations between activities in the system.

Another way to study local dynamical properties is to analyze dispersion of multichannel time-series $\{n_i(t)\}$ deffined for every node $i = 1, 2, ..., N$ (Argollo de Menezes & Barabasi, 2004; Duch & Arenas, 2006; Kujawski *et al.*, 2007; Tadić, 2006).

The standard deviation vs average value of time-series obeys scaling defined by equation:

$$\sigma_i(n_i) \sim < Q_i >^{\mu}, \tag{3.51}$$

with exponents μ between two limit values: $\mu = 1/2$ and $\mu = 1$. The scaling relation suggests a universal behavior across a variety of networks (Argollo de Menezes & Barabasi, 2004). For each nanoparticle in the network we found average charge $< Q_i >$ and the standard deviation σ_i of charge fluctuations in time. Results for our two example networks are shown in Figure 3.13. In both cases: (a) on a network with homogeneous connectivity $CNET$ and (b) on the $NNET$ with inhomogeneous connectivity, points for all nanoparticles obey scaling behaviour.

3.7 Comparison of Topological and Charge Disorder

In this section we will compare the effects of topological vs. charge disorder in the system by analyzing local conduction properties in two cases: (1) a regular triangular array with charge

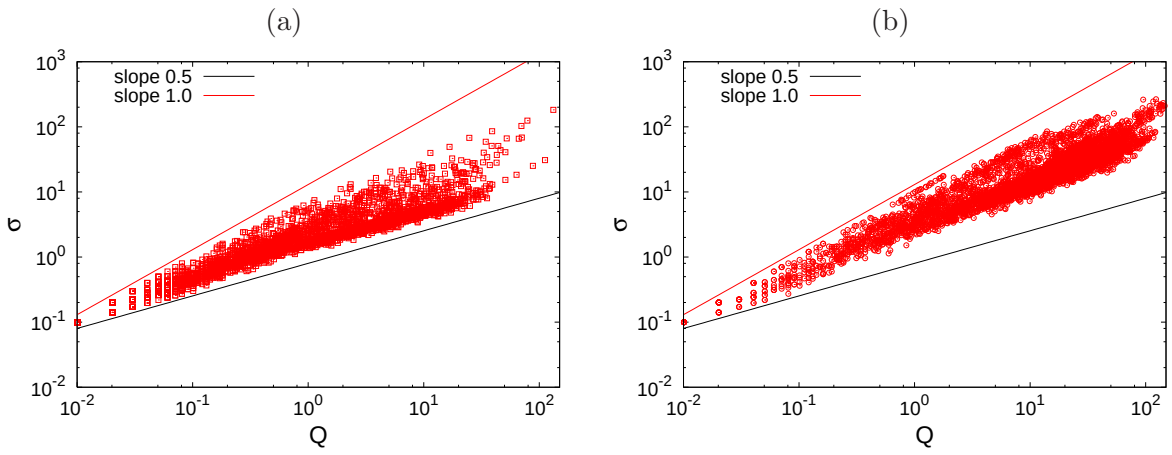

Figure 3.13: Standard deviations σ_i of fluctuations time series of charge on a single node against average charge Q_i at that node. Each point represents one node on: (a) a network with homogeneous connectivity $CNET$ and (b) on the $NNET$ with inhomogeneous connectivity. Limiting slopes $\mu = 1/2$ and $\mu = 1$ defined in Eq. (3.51) are shown by straight lines.

disorder; and (2) the inhomogeneous nano-network $NNET1$.

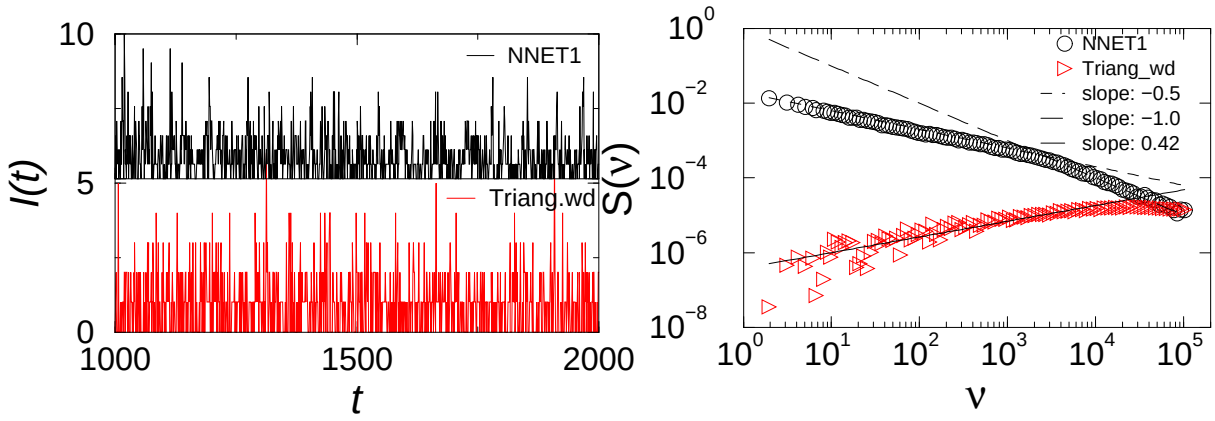

Figure 3.14: Current fluctuation time series for triangular nanoparticle array with charge disorder and for NNET1 (left) and the corresponding power spectra (right).

For the current, which is measured at the electrode, we consider its time-series of the current $\{I(t)\}$, given in Fig. 3.14, and the increments of the current $\{\Delta I(t)\}$, which is a measure of the acceleration in the electron transport along the conducting paths. Each point is averaged

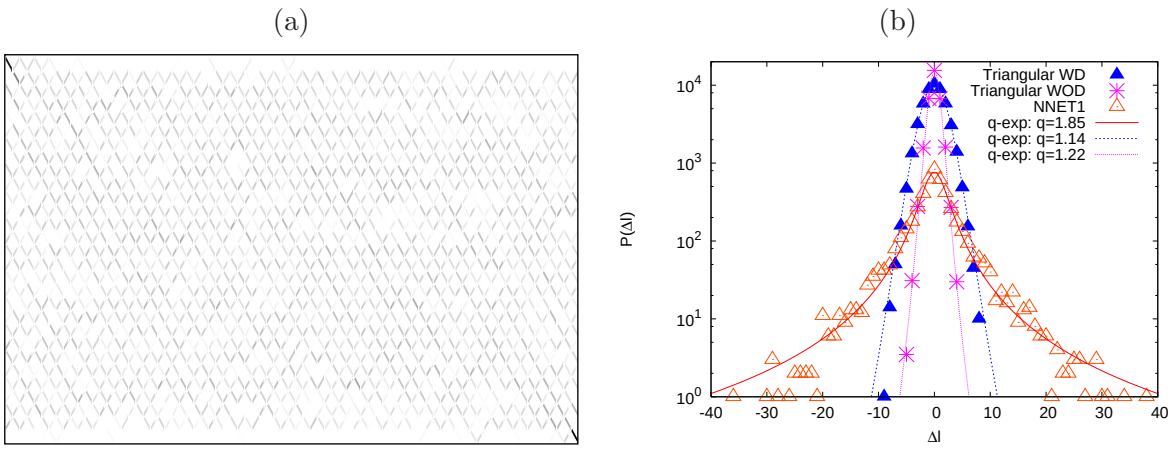

Figure 3.15: (a) Visualization of the conduction paths through a regular triangular array with charge disorder at nodes (b)Distributions of the increments of charge-fluctuations $P(\Delta I)$ plotted against ΔI for the regular triangular array with charge disorder and for the topologically disordered NNET1. Fits are q-Gaussian according to Eq. 3.52

over time window $t_{WIN} = 100$ time steps (updates of the whole network). In Fig. 3.15(right) we have shown the distributions of the increments $P(\Delta I)$ obtained for a fixed voltage above the threshold, for the triangular array with charge disorder and for the topologically disordered nanoparticle array NNET1. The distributions are fitted with the q-Gaussian (Pluchino *et al.*, 2008; Tsallis, 1988)

$$P(\Delta I) = B\left(1-(1-q)\left(\frac{\Delta I}{D_0}\right)^2\right)^{1/1-q} \quad ; \tag{3.52}$$

with different q values for different geometries of the nanoparticle arrays: $q = 1.14$ for the geometrically regular triangular array with charge disorder, while $q = 1.85$ for the topologically inhomogeneous NNET1. Similarly, the analysis of the time series of the current itself, $\{I(t)\}$, exhibits different correlations in these two geometries. In Fig. 3.14 the power-spectra of the time series for triangular network are shown. The spectrum of the topologically in homogeneous NNET1 shows the long-range correlations as $S(\nu) \sim 1/\nu$ at high frequencies, whereas the spectrum flattens at high frequencies in the case of the triangular charge-disordered array. At low frequencies, however, weak correlations are observed in both networks.

3.8 Conclusions

In this chapter the conduction via single electron tunneling through nanonetworks is studied. We have given a detailed theoretical background and introduced a generalized conduction model. The model has been tested on cases where analitical solutions are well established (single nanoparticle and one-dimensional array) and numerically for previously studied regular structures. Furthermore, we studied in detail properties of the conduction processes through the sample which make physical ground for the observed I-V nonlinearity. We used nanonetwork models introduced in previous chapter and found that topology have important influence on nonlinearity in conduction. Inhomogeneities in structure increase the nonlinear exponent at the current-voltage curve. The results are consistent with experimentally measured I-V characteristics. The collective dynamic behavior along the conducting paths through the nanoparticle arrays leads to nonlinear current–voltage curves, correlations in time series of charge fluctuations, and fat-tail distributions and scale invariance. The scaling exponents and other quantitative indicators of the dynamics vary when certain topological features of the graph are changed.

Chapter 4

Colloidal Assembly with Bio-Molecular Recognition

In the Introduction it was shown that different methods have been developed recently for the assembly of nanoscale particles ligated with complementary chemical molecules (Mirkin, 2000; Mirkin *et al.*, 1996; Nykypanchuk *et al.*, 2008; Park *et al.*, 2008). Consider two types of colloidal particles, A and B, which are ligated by biopolymers, as shown schematically in figure 4.1a, such that the complementary parts of the molecule is attached to different particle types. Some well known examples are the proteins with *specific reactions*, e.g., in the *antigen–antibody* recognition (Huber, 1986) and in the complementary pieces of DNA molecule (Mirkin *et al.*, 1996), where the strength of bonding is directly related to the number of complementary base pairs. It was demonstrated recently (Nykypanchuk *et al.*, 2008; Park *et al.*, 2008) that, by varying the lengths of the free and the bonding parts of the ligands, different three-dimensional structures of nanoparticles may emerge, including regular BCC-like supra-crystals.

4.1 Model of Interactions Between Ligated Nanoparticles

Attractive interactions between the particles of interest here arise both due to van der Waals interactions and hydrogen-bonding and are usually described in the literature by the attractive part of the α-Lennard-Jones potential (Mossa *et al.*, 2004; Zaccarelli, 2007). The attraction occurs at distances above the "bonding distance", d_B, which depends on the particle sizes and the lengths of the attached biopolymers (see Figure 4.1). At the "bonding distance" particle pair A–B binds together via hydrogen bonding (Nykypanchuk *et al.*, 2008) or click-chemistry mechanisms (Brennan *et al.*, 2006) where at smaller distances $d < d_B$, a repulsive interaction

starts building up first as a soft interaction between attached polymer chains and eventually reaches the hard-core repulsion at the touching distance $d = R_A + R_B$ (as shown in figure 4.1b). We also assume that a large number of polymer chains of the same kind are symmetrically distributed over the particle surface, so that the radial symmetry of the potential is preserved. Hence, in the absence of the long-range electrostatic repulsion, the potential for the effective

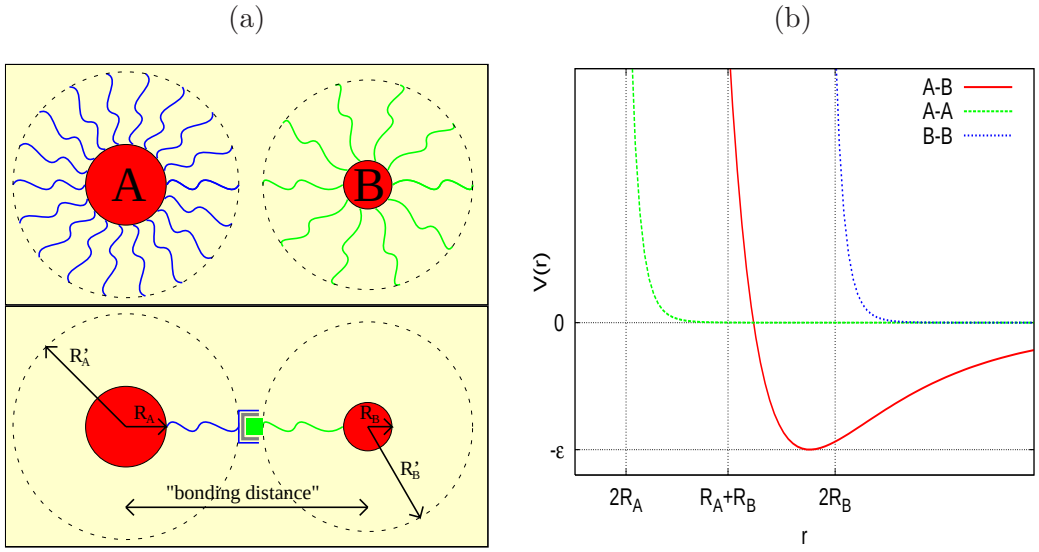

Figure 4.1: Schematic view of the bio-recognition bonding between pairs of ligated colloidal particles A and B (a) and the potentials (b) in the binary colloidal mixture with particle radii R_A and R_B.

interaction between pairs of particles of different kind is given by

$$V_{A-B}(r) = 4\epsilon \left(\frac{\sigma^{12}}{(r - R_A - R_B)^{12}} - \frac{\sigma^{6}}{(r - R_A - R_B)^{6}} \right), \tag{4.1}$$

where r denotes the distance between particles, R_A and R_B are their radii and σ and ϵ are the parameters. Here we use the $\alpha = 6$, the classical version of the Lennard-Jones potential, given in Eq. (4.1), which corresponds to a wide potential well and, thus, allows the particle attraction in a wider area. (The potential well becomes increasingly narrow for larger α values studied in Ref. (Mossa *et al.*, 2004). The depth ϵ measures directly the binding strength of the bio-recognition pair (I. Jelesarov & Bosshard, 1996). Similarly, the optimal binding distance, corresponding to the potential minimum in figure 4.1b, is related to the parameter σ in view of Eq. (4.1), suggesting that σ should be suitably selected when the particle sizes are given. For

the pairs of equal-type particles, A–A and B–B, we assume repulsive interactions described by the first term in the Lennard-Jones potential:

$$V_{X-X}(r) = 4\epsilon' \frac{\sigma'^{12}}{(r - 2R_X)^{12}} \ , \tag{4.2}$$

where R_X stands for R_A or R_B, and the parameters σ' and ϵ' may in principle be different from those for the A–B interaction.

4.2 Equation of motion and Simulations

4.2.1 Langevine equation

First we will consider a single nanoparticle in liquid. Over the time particle will continuously collide with the small liquid molecules. On average the particle will collide more often on the front side than on the back side. Therefore, it will experience a force proportional to its velocity. This proportional constant is given as viscosity coefficient ν. Besides this viscosity force the particle will experience a stochastic force $\mathbf{F}_T(t)$. The equation of motion can be written:

$$\dot{\mathbf{r}} = \mathbf{v}, \tag{4.3}$$

$$m\dot{\mathbf{v}} = -\nu\mathbf{v} + \mathbf{F}_T. \tag{4.4}$$

The viscosity coefficient is given by:

$$\nu = 6\pi\eta R/m, \tag{4.5}$$

where R and m are radius and mass of the particle, and η is viscosity of liquid. General solution for equation 4.4 is:

$$\mathbf{v}(t) = \mathbf{v}_0 e^{-\nu t/m} + \int_0^t \mathrm{d}\tau e^{-\nu(t-\tau)/m} \mathbf{F}_T(\tau)/m. \tag{4.6}$$

If we want to calculate kinetic energy of the particle or any other macroscopic quantity we have to average over all realizations of $\mathbf{F}_T$. Therefore, kinetic energy is given:

$$\begin{aligned} E = \frac{m\left\langle \mathbf{v}^2 \right\rangle}{2} = \frac{m}{2} \Bigg[& \mathbf{v}_0^2 e^{-2\nu t/m} + 2\int_0^t \mathrm{d}\tau e^{-\nu(2t-\tau)/m} \mathbf{v}_0 \cdot \left\langle \mathbf{F}_T(\tau) \right\rangle / m^2 + \\ & \int_0^t \mathrm{d}\tau \int_0^t \mathrm{d}\tau' e^{-\nu(2t-\tau-\tau')/m} \left\langle \mathbf{F}_T(\tau) \cdot \mathbf{F}_T(\tau') \right\rangle / m^2 \Bigg]. \end{aligned} \tag{4.7}$$

In order to continue we have to make some assumptions about the conditional averages of the stochastic forces. In view of the chaotic character of the stochastic forces the following assumptions seem to be appropriate:

$$\langle \mathbf{F}_T(t) \rangle = 0, \tag{4.8}$$

$$\left\langle \mathbf{F}_T(t) \cdot \mathbf{F}_T(t') \right\rangle = C\delta_{t,t'}, \tag{4.9}$$

where C is constant quantity or depend on $\mathbf{v}_0$. From equations 4.7, 4.8, and 4.9:

$$E = \frac{m}{2}\mathbf{v}_0^2 e^{-2\nu t/m} + \frac{C}{4\nu}\left(1 - e^{-2\nu t/m}\right). \tag{4.10}$$

In the thermodynamics equilibrium (in the limit for large t) kinetic energy $E \to C/4\nu$ should be equal to $3k_BT/2$ from which we get $6k_BT\nu$ and finally:

$$\left\langle \mathbf{F}_T(t) \cdot \mathbf{F}_T(t') \right\rangle = 6k_BT\nu\delta_{t,t'}, \tag{4.11}$$

Integrating equation 4.6:

$$\mathbf{r}(t) = \mathbf{r}_0 + \mathbf{v}_0 m \frac{1 - e^{-\nu t/m}}{\nu} + \int_0^t \mathrm{d}\tau \int_0^\tau \mathrm{d}\tau' e^{-\nu(\tau-\tau')/m} \mathbf{F}_T(\tau')/m, \tag{4.12}$$

from which we can calculate the mean square displacement. In thermodynamics limit $t \to \infty$ this becomes:

$$\left\langle (\mathbf{r}(t) - \mathbf{r}_0)^2 \right\rangle = \frac{6k_BT}{\nu} t. \tag{4.13}$$

The standard meaning of these term, in view of the Einstein-Smoluchowski relation, is that the diffusion coefficient D of nanoparticle is given by $D_i = k_BT/\nu_i$. Here we used: $\left\langle (\mathbf{r}(t) - \mathbf{r}_0)^2 \right\rangle = 6Dt$.

In our system of binary colloidal mixture we have to include interaction between pairs of nanoparticles described in Eqs. (4.1)-(4.2):

$$\nu_i \dot{\mathbf{r}}_i = -\nabla_{\mathbf{r}_i} \sum_j V_{i-j}(|\mathbf{r}_i - \mathbf{r}_j|) + \mathbf{F}_{i,T}, \tag{4.14}$$

where r_i is the position of ith particle and ν_i stands for $\nu_A \equiv 6\pi\eta R_A$ or $\nu_B \equiv 6\pi\eta R_B$, when the ith particle is of the type A or type B, respectively, η is the fluid viscosity coefficient. The stochastic Langevin force $F_{i,T}$ can be seen as originating from the integration over the fluid degrees of freedom. In the simplest case the fluctuations of the Langevin term are uncorrelated, and described by the moments of a normal distribution with

$$\langle F_{i,T}(t) \rangle = 0, \tag{4.15}$$

$$\left\langle F_{i,T}(t)F_{j,T}(t')\right\rangle = 6k_BT\nu_i\delta_{i,j}\delta_{t,t'}. \tag{4.16}$$

The standard meaning of these terms, in view of the Einstein-Smoluchowski relation, is that the diffusion coefficient D_i of ith particle is given by $D_i = k_BT/\nu_i$, which is generally different for the particles of A and B type, and k_BT is the thermal energy.

4.2.2 Numerical Implementation

We used fourth-order Runge-Kutta method ($RK4$) to solve the differential equations (4.14) for the trajectories of colloids of both A and B type. In the simulations the following set of parameters is specified: the size R_A, R_B and number N_A, N_B of the particles of the type A and B, the respective viscosity (or diffusion) coefficients ν_A and ν_B, the temperature T and the parameters of the potential σ and ϵ/k_BT. We start with a random distribution of $N = N_A+N_B$ particles in a box of size $L \times L$ with an infinite potential at the boundaries. At each time step $k \times \Delta t$ the positions of the particles are updated in parallel according to the Eq. (4.14). The small step Δt is chosen so that the updated positions of the particles result in a smooth change of the potential. The random Langevin force $F_{i,T}$ is distributed once at each time step according to the symmetric normal distribution with the second moment given by Eq. (4.16).

Initial Conditions: We assign uniformly random coordinates within box $L \times L$ to all particles (m of A kind and $n - m$ of B kind).

Time Integration: For each particle we calculate the position in the next time step as:

$$\mathbf{r}_i(t + \Delta t) = \mathbf{r}_i(t) + \frac{\Delta t}{6}(\mathbf{k}_1 + 2\mathbf{k}_2 + 2\mathbf{k}_3 + \mathbf{k}_4), \tag{4.17}$$

where the vectors $\mathbf{k}_j$ are given:

$$\mathbf{k}_1 = \mathbf{f}(\mathbf{r}_i), \mathbf{k}_2 = \mathbf{f}(\mathbf{r}_i + \mathbf{k}_1\Delta t/2), \tag{4.18}$$

$$\mathbf{k}_3 = \mathbf{f}(\mathbf{r}_i + \mathbf{k}_2\Delta t/2), \mathbf{k}_4 = \mathbf{f}(\mathbf{r}_i + \mathbf{k}_3\Delta t), \tag{4.19}$$

$$\tag{4.20}$$

and where $\mathbf{f}(\mathbf{r}_i)$ is the force on the particle i in the position $\mathbf{r}_i$, given as gradient of the potential and the Langevin term.

Boundary conditions: The boundary conditions are given with infinite potential barrier outside of the box $L \times L$. This is implemented in the way that in each time step we check if a particle position is outside of the box and reflect the particle position if it is.

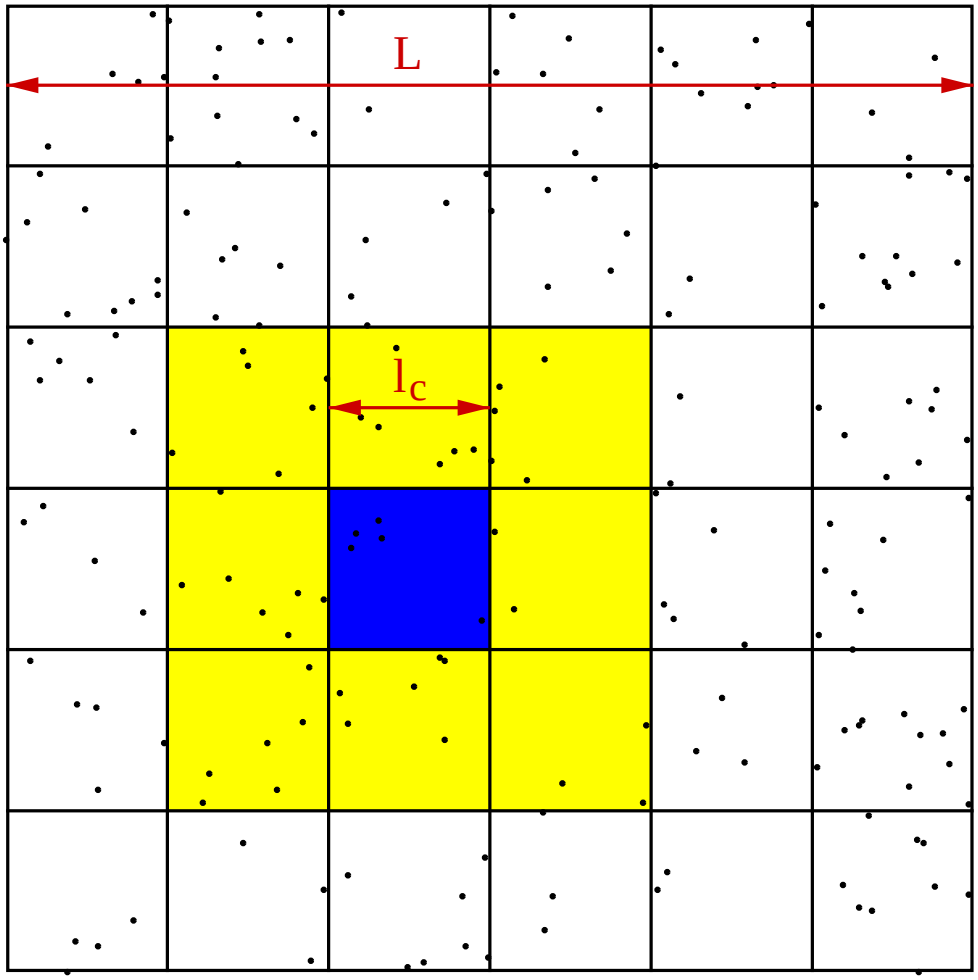

Figure 4.2: Cell-List Algorithm. Schematic view.

Algorithm complexity: In each time step we need to calculate interaction between each pair of particles. Therefore, the complexity of the algorithm is given as $o(n_{ts}n^2)$ where n_{ts} is number of time steps.

Cell lists: There are only short-range interactions in our system. Therefore, we can reduce the computational cost of algorithm using cell list algorithm. Cell lists works by subdividing the simulation box $L \times L$ into square cells $l_c \times l_c$ with an edge equal to the cut-off radius l_c of the Lenard-Jones interaction (see Fig. 4.2). In first step we calculate the cell indices (i_c, j_c) for each particle and make the list of all existing cells. This takes $o(n)$ calculation steps. Then the interactions are computed between particles in the same and neighboring cells from the list,

see figure 4.2. The computational complexity of this step is $o((k+1)n_c n)$ where k is maximum number of neighboring cells ($k = 8$ for $2D$) and n_c is average number of particles per cell $n_c \approx n l_c^2/L^2$. Because there exist the maximum number of particles per cell, the complexity is linear $o(n)$, which is significantly better than computing the $o(n^2)$ interactions.

The whole algorithm can be written as follows:

```
Initial: random positions within box LxL
For each time step:
  calculate cell (ic,jc) index for each particle
  make list of neighboring cells
  For all neighboring pair of cells (C1,C2):
    For all particles i in C1:
      For all particles j in C2:
        Calculate interaction between i and j
      End for
    End for
  End for
  Update positions of particles
  For all particles:
    If particle is outside the box LxL:
      reflect the positions of particle
        over box edge
    End for
  End for
End for
```

Notice that due to the ligands attached to each particle, the larger radii marked with R'_A and R'_B in the figure 4.1a, are relevant for the definition of the *coverage* of the box with particles. In the simulations, when two particles bind with the compatible chemistry, they stay at the binding distance which may be larger than the particle radii, however, a free particle can not move across the bond. Such constraints to the particle motion induce additional effective interactions, making the system to condense at non-equilibrium global energy states. These effects are depending on the overall particle density and the fraction of the attractive particle pairs compared to the total number, N_A/N. In principle, at any finite temperature a bond may break, however, the process is less probable at the low temperatures. Here we keep $k_B T\epsilon \ll 1$. The system can be additionally "equilibrated" by sudden increase and subsequent drop of temperature.

4.3 Emergent Nanoparticle Aggregates

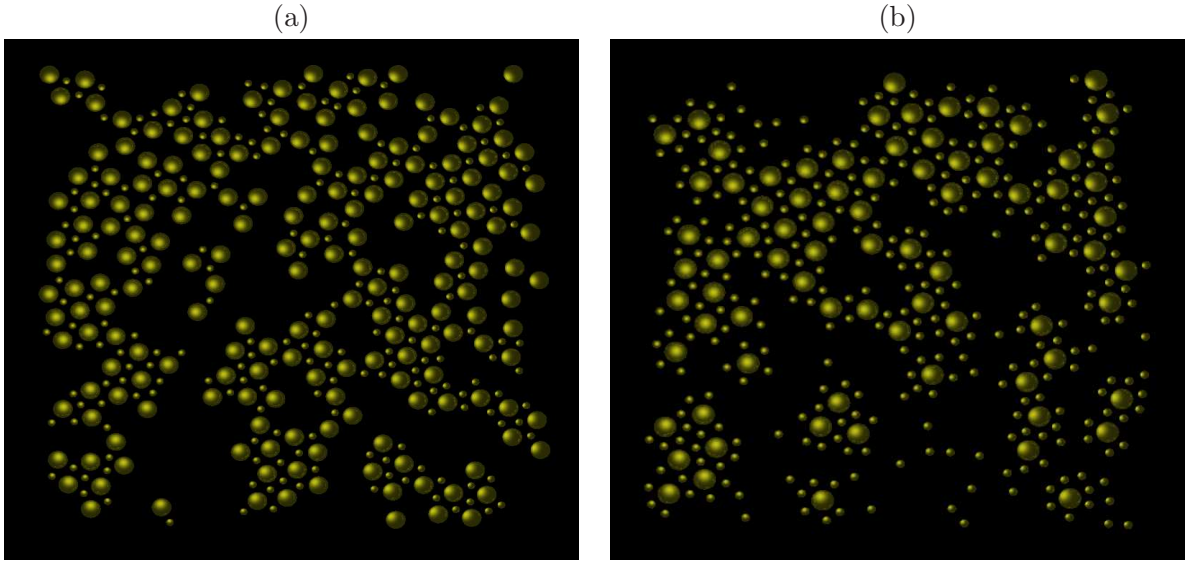

Figure 4.3: A three-dimensional rendering of simulated nanoparticle assemblies obtained by diffusion and aggregation with bio-recognition bonding: two types of particles with the size ratio $R_A/R_B = 2.5$ and fixed total number of particles $N_A + N_B$ and for the concentration ratio $N_B/N_A =$ (a) 1 and (b) 4.

For a given ratio of the particle sizes R_A/R_B, the emergent structure of the nanoparticle aggregates depends on the coverage, $\Phi = A/L^2$, where A is total area covered by the particles, and on the relative concentrations of two particle types N_B/N_A. In Figs. 4.3a and b we show the assemblies obtained with same total number of particles but different fractions of the large (A) and small (B) particles. Note that the ratio of the particle sizes R_A/R_B determines the maximum number of small particles that can attach to a single large particle. The local structures with large particles linked via small particles occur, which are joined in an irregular pattern, with voids of different sizes. The walls of such voids are built of large particles in the case of equal concentrations. However, for the abundance of the small particles, as in figure 4.3b, the aggregates of different sizes are often isolated by small particles.

Entirely different situation if found when the particle sizes are equal, the particles differ only by the ligand type. In figure 4.4a we show the situation corresponding to the equal concentrations of particles, when the spatially regular structure arises. The regular pattern with alternating A-B-A-B particles spans almost the whole system, with a few topological defects. In the case

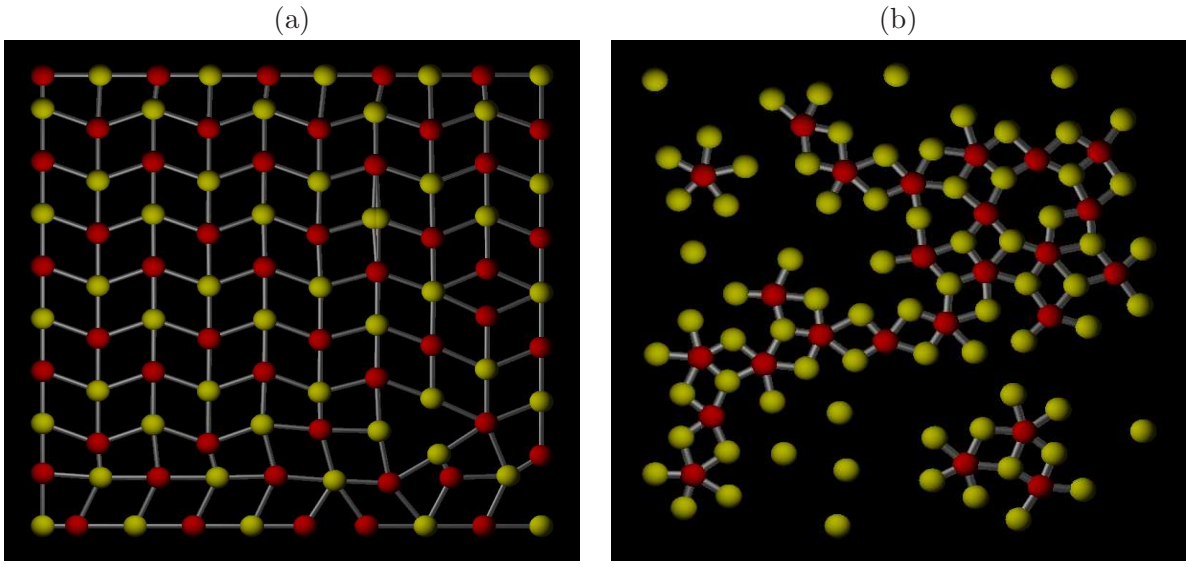

Figure 4.4: Simulated nanoparticle structures obtained by diffusion and aggregation with bio-recognition potentials: Occurrence of regular structure at equal size particles with (a) full coverage with equal concentrations of A and B particles and (b) 50% coverage with concentration ratio 1:3.

when one particle type is in abundance compared to the other, such structural regularity remains only at the local level. Large as well as isolated clusters may be found, as in figure 4.4b. In both figures the bonding links between the compatibly ligated nanoparticles are shown.

4.3.1 Parameter Dependencies and Phase Diagrams

In figure 4.5 we present nine different emergent structures (three different coverages times three different relative concentrations) in the case when particles have different sizes $R_A = 2.5R_B$. Different phases can be recognized: gas phase, quasi one-dimensional aggregates, crystals, quasi-crystals, and glasses.

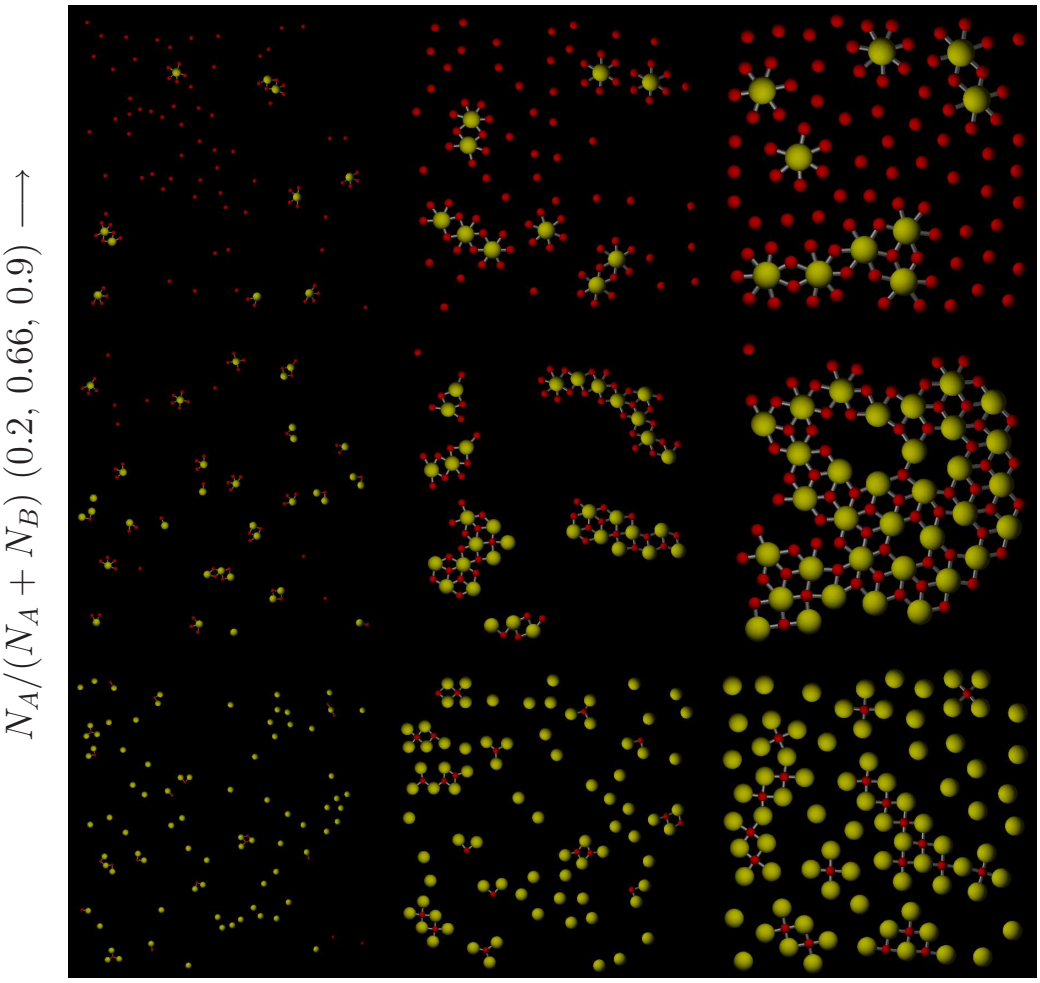

Figure 4.5: Phase diagram in the case $R_A = 2.5R_B$

Similarly, on figure 4.6 are presented nine different emergent structures for the same particle sizes. Note that in this case phase diagram is symmetrical in respect to a line $N_A/(N_A+N_B) = 1/2$. The figure 4.6 illustrate one half of it.

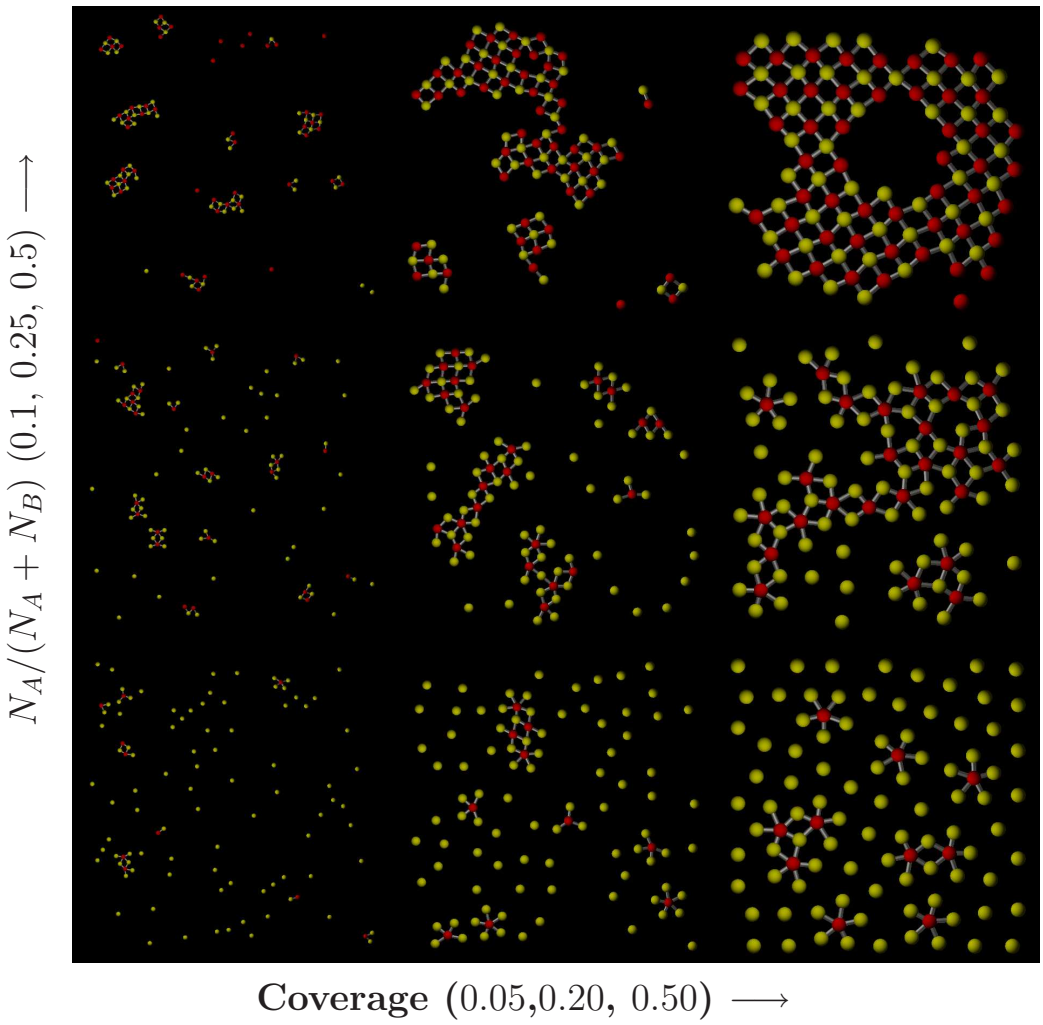

Figure 4.6: Phase diagram in the case $R_A = R_B$

4.3.2 Structural properties of the Aggregates

The regularity of the nanopatterns in our 2-dimensional simulations can be quantitatively measured by computing the structure factor $S(q)$ defined by

$$S(\mathbf{q}) = \left| \sum_{i=1}^{N} e^{-i\mathbf{q}\mathbf{r}_i} \right| \tag{4.21}$$

where r_i are positions of nanoparticles in the 2-dimensional box. In figure 4.7a we show $S(q)$ obtained after angular averaging of $S(\mathbf{q})$ and different coverages Φ. The figure 4.7a shows how the regular structure of nanoparticles arises, leading to the characteristic oscillatory pattern of the surface $S(q, \Phi)$ (seen in the upper left part), with increased coverage and equal particle size.

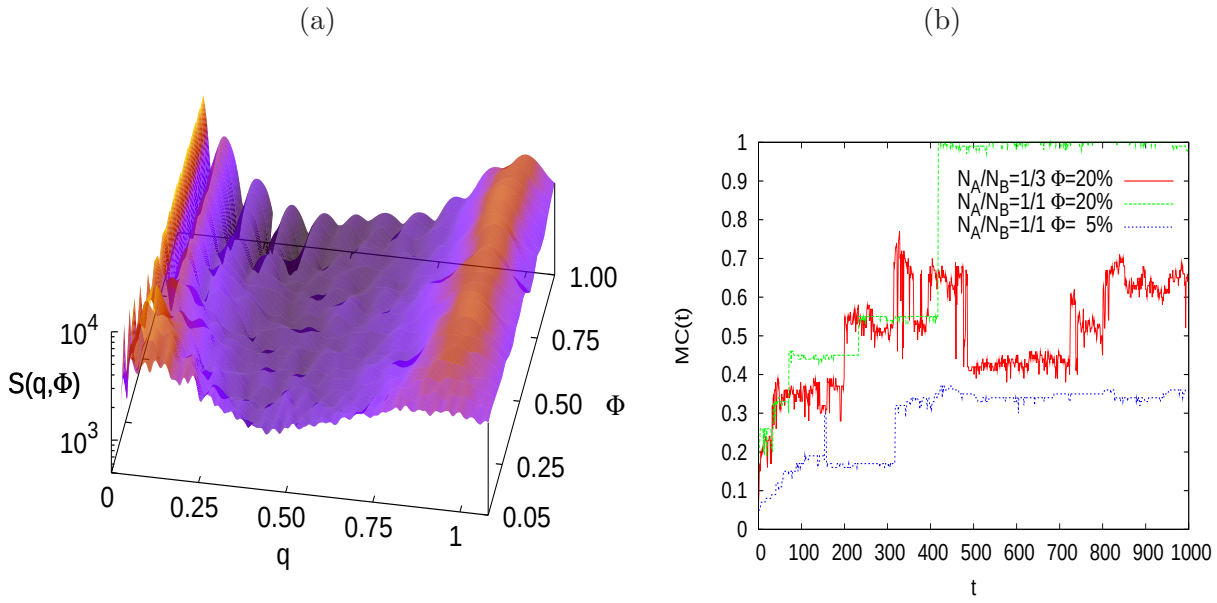

Figure 4.7: (a) Structure factor $S(q)$ for nanoparticle aggregates obtained by bio-recognition bonding for equal size particles and varied coverage Φ. (b) Growth of the largest cluster of connected nanoparticles against time for various values of coverage Φ and concentration ratios N_A/N_B.

The time evolution of the largest cluster, shown in figure 4.7b, reveals the aggregation process in more details. Depending on the coverage Φ and relative concentrations of the A and B particle types, one can observe that either large clusters join together (marked by big jumps in the upward curves), or small A–B complexes are being attached to a large cluster. In addition, the process

is affected by the initial growth of the large cluster, which increasingly slows down the cluster diffusion.

4.4 Conclusions

In this part of the thesis, a model of colloidal aggregation via bio-recognition binding was studied. The interaction between chemically complementary particles was treated as a Lennard-Jones interaction while interaction of particles of the same kind was considered as short range repulsion. The system was simulated by solving the Langeven equation in highly viscous media. It was shown that both regular and highly inhomogeneous nanoparticle films can be assembled within the same process. The system studied is far from the thermodynamic equilibrium but, in the low temperature limit, the final assemble is metastable.

Chapter 5

Conclusions

In this thesis we studied single electron transport through topologically complex nanoparticle networks formed by a far-from-equilibrium self-assembly process. The interpretation, modeling and analysis of the experiments in this area is far from being simple. The physics of nanoparticle ensembles is a rich and complex area of modern condensed matter science, that has rapidly expanded in the past few decades.

We investigated two types of problems related to large-size nanoparticle films: (a) the structure of nanoparticle aggregates, (b) the conduction via single electron tunneling through nanopaticle films.

The structure of complex nanoparticle aggregates was studied using three different models:

- Networks based on fixed positions of the nanoparticles on substrate from empirical data: we introduced a network model in which we use the known positions of nano-particles on the substrate, e.g. via AFM measurements or as a result of the self-assembly model.

- Nearly-equilibrium assemblies emerging in bio-molecular recognition binding: we simulated binary colloidal mixtures directly by solving the equations of motion.

- Cellular networks grown by cell-aggregation rules: a new algorithm for the growth of graphs by aggregation process of extended objects - polygons with a give size distribution are introduced.

Conduction via quantum tunneling has been studied numerically through some of the nanoparticle arrays. The topological elements of these nano-networks were selected as follows: a node represents a nanoparticle, while the edges (links) represent tunneling junctions between nanoparticles. The main conclusions from this numerical study of single electron transport can be summarized as follows:

- Inhomogeneities in structure increase the nonlinearity exponent ζ in current-voltage characteristic curve. The exponent for the I–V curve, found in range $\zeta \in (1, 4)$ depending on structure, is in agreement with the experiments.

- Collective dynamical effects in the tunneling process deep inside the sample lead to a non-Gaussian current fluctuations on the electrode. We have determined various statistical measures of these collective effects. A non-Gaussian distribution has been found in the experiments with nanowires (Kohno & Takeda, 2007). Our numerical results suggest that a $q-$Gaussian distribution with different parameters could be measured in the nanoparticle films. The occurrence of the $q-$Gaussian distribution in a larger class of complex dynamical systems with long-range interactions has been discussed recently (Tsallis *et al.*, 2007).

- Numerical model allows study away from the electrode deep inside the sample. Long range correlations in total charge in the system is observed. Conducting paths through the film have been identified. Coalescence of flow along different pathways contributes to the nonlinearity of the conduction process. Distribution of current through single junctions was compared with topological flow distribution.

- We demonstrate how different types of disorder affect the conduction in our comparative study of regular nanoparticle array in the presence of local charge disorder, on one side, and topologically inhomogeneous nano-network without charge disorder, on the other.

The material presented here sheds a new light on the problem of engineering of the functional materials with desired characteristics.

List of Figures

Appendix A

Physics Based Layouts for Graph Visualization

As we mentioned in the introduction in this thesis are used force based layouts for the graph visualization. Graph visualization itself represents an important computational tool in analysis of complex networks.

Two physical models which are often used are: the spring algorithm (Eades, 1984), where the links are replaced by springs with unit natural length and the nodes are interacting with a repulsive force, and Kamada-Kawai algorithm (Kamada & Kawai, 1989), where one looks for the optimal potential that makes the distances between the nodes tend to their corresponding topological distances. The efficiency of these two algorithms for different kinds of networks (trees, scale-free graphs, cellular networks which are planar graphs introduced in the Chapter 2, and gene interaction network (Živković *et al.*, 2006)) are shown in this Appendix. Furthermore, in the case of highly clustered graphs next-neighbor approximation is proposed.

The first model is known as Kamada-Kawai (Kamada & Kawai, 1989) model and it is based on idea to place the vertices on such places in the plane with geometric distances correlated with topological distances. The energy in this model is given with:

$$E = \sum_{i,j} k_{ij}(|\mathbf{r}_i - \mathbf{r}_j| - l_{ij})^2, \tag{A.1}$$

where $\mathbf{r}_i$ are vectors of positions of vertices, k_{ij} are parameters (here we use constant value $k_{ij} = 1$), and l_{ij} is topological distance between vertices - shortest path length. Shortest path

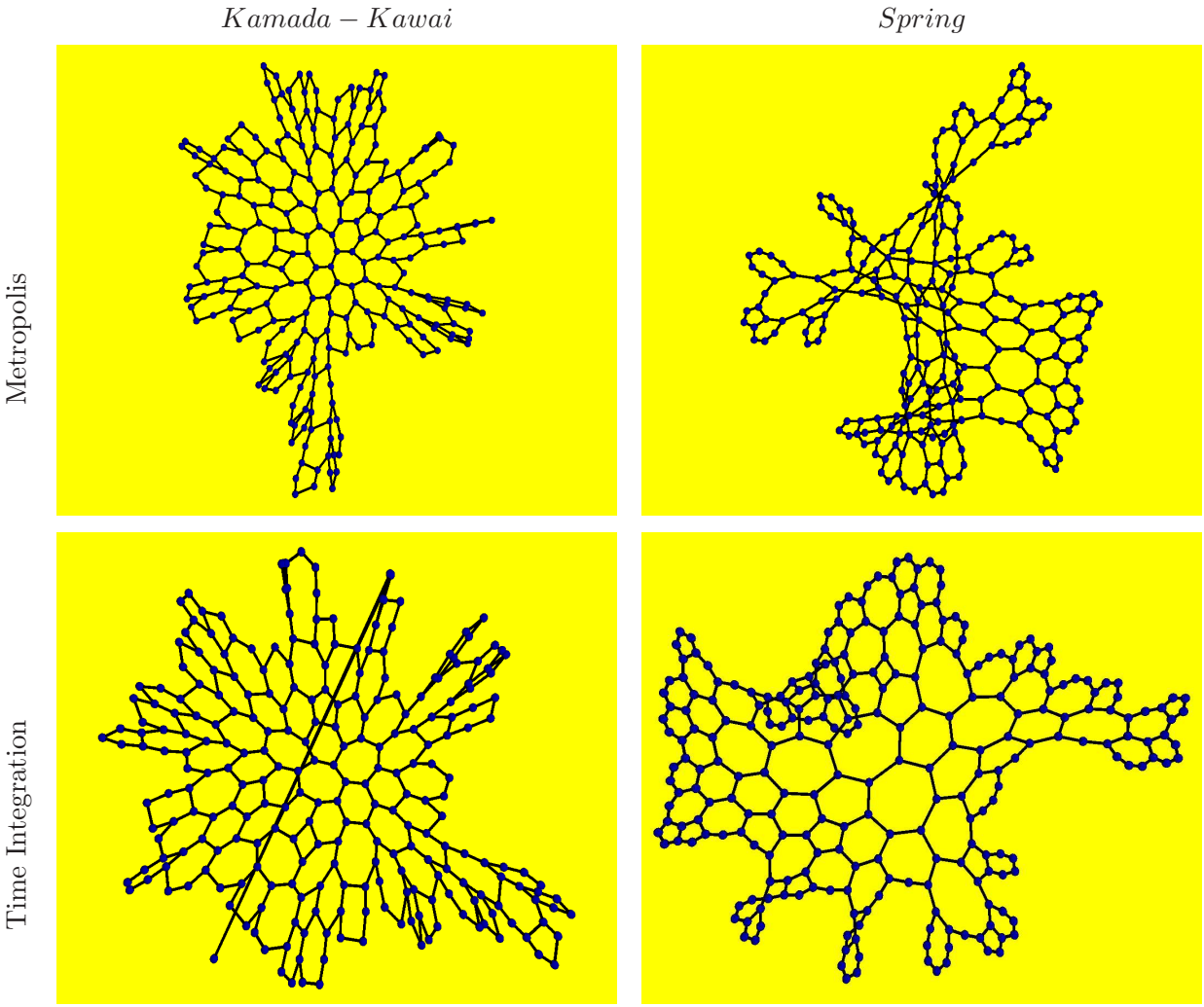

Figure A.1: Same cellular planar graph of $N = 256$ nodes shown with four different visualization methods. Relative numbers of edge crossings χ are: 0.01%, 0.31%, 0.05%, 0.06%.

between two vertices is defined as path between them with smallest number of edges (Bollobás, 1998). In this case, the value of l_{ij} is an positive integer number. The physical interpretation is an harmonic interaction between every two vertices with a minimum on the distance given with shortest path length.

Second model is known as spring model (Eades, 1984) in which the energy is given by:

$$E = \sum_{(i,j)\in E} k_{ij}(|\mathbf{r}_i - \mathbf{r}_j| - l_0)^2 + \sum_{i,j} \frac{g}{|\mathbf{r}_i - \mathbf{r}_j|^\eta}, \tag{A.2}$$

where k_{ij}, l_0, g and η are parameters, and $\mathbf{r}_i$ are vectors of the positions of vertices. In the physical interpretation, first term represent springs with length l_0 between neighboring vertices and second term represent "electrostatic repulsion" each pair of vertices.

For large graphs there are lot of local minima in the energy function, which make the visualization procedure increasingly complex.

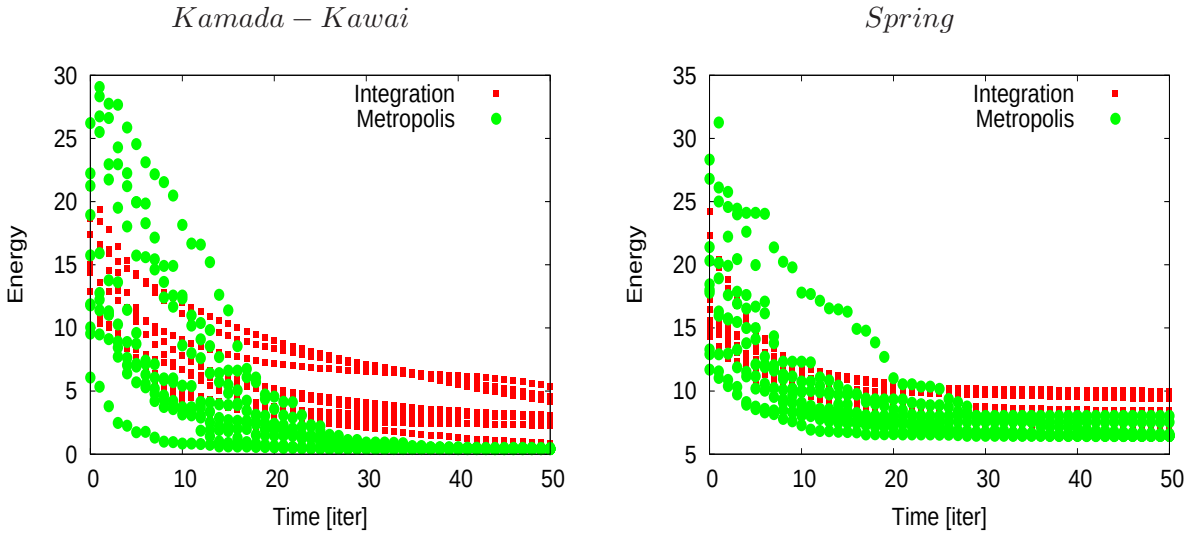

Figure A.2: Relaxation of two energy models for the same planar graph shown on Fig. A.1 ant two minimization algorithms. Different lines correspond to different initial conditions.

We show two models for graph visualization given by energy as function of the positions of the vertices. The final planar embedding is given as a minimum of the energy function. In order to find the energy minimum we use two different algorithms: metropolis and time-integration algorithm.

In the metropolis algorithm we calculate the energy change for node random movement, usually taken from Gaussian distribution. The movement is accepted with a probability given by $p = max(1, e^{-\Delta E/T})$, where ΔE is energy change and T is "temperature" parameter. We implement this algorithm according to following steps:

```
Initial node positions: randomly given

Do:

  For i=1 to N:
```

```
    e0=energy of the system
    move node i randomly
    e1=energy of the system
    Accept movement with probability: exp(-(e1-e0)/T))
  End loop i
Until maximal movement is smaller than a threshold value
```

As the second algorithm we use the numerical time-integration of the following set of equations:

$$\frac{\mathrm{d}\mathbf{r}_i}{\mathrm{d}t} = -\nu \frac{\partial E}{\partial \mathbf{r}_i}, \tag{A.3}$$

where ν is a "viscosity" parameter. It is implemented as follows:

```
Initial node positions: randomly given
Do:
  For i=1 to N:
    Calculate force on node i as gradient of the energy
    Move the node
  End loop i
Until maximal movement is smaller than a threshold value
```

Algorithm Efficiency and the Graph Layouts On Fig. A.1 we show different graph layouts for the same planar graph with cellular structure introduced in Chapter 2 with control parameters $\mu_2 = 1.0$ and $\nu = 1.0$. For reasons of clarity here we use the small size of network is $N = 256$. To compare results we will use relative number of edge crossings defined as $\chi = N_{cs}/N_{cs,0}$ where N_{cs} is number of edge crossings for given layout and $N_{cs,0}$ is average number of edge crossings for the same graph for a random layout. In all results we calculated χ using value for $N_{cs,0}$ averaged over 10 random layouts. The Kamada-Kawai method gives better result (see left column on Fig. A.1). Quantitatively this difference can be related to faster energy relaxation and absence of many minima shown on Fig. A.2. In both cases there are a lot of minima, but in the Kamada-Kawai case a global minima is always found with metropolis algorithm. For the planar graph the difference in the minimization procedure is less pronounced in the case of the spring algorithm.

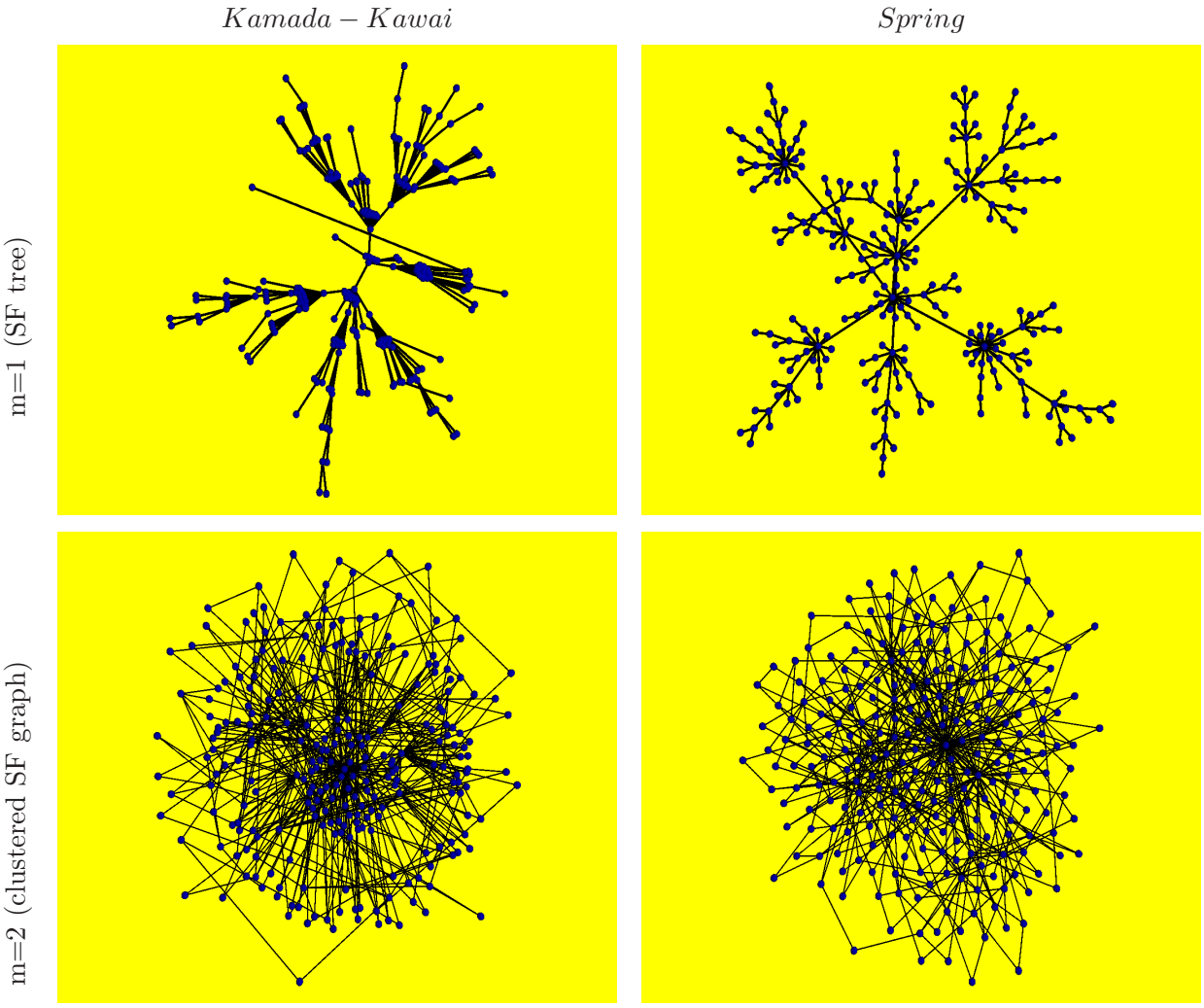

Figure A.3: Emergent layouts for two different models (left column: Kamada-Kawai, right column: spring model) for scale-free tree (top panels), and clustered scale-free graph (Tadić, 2001) (bottom panel). In all cases the metropolis minimization algorithm was used. Relative numbers of edge crossings χ are: 0.70%, 0.25%, 23.5%, 17.0%.

The comparison between two energy models for scale-free graphs is shown on Fig. A.3. In both cases spring algorithm gives better results.

Spring Model with Next-neighbor Interaction A considerable computational acceleration in the algorithm is possible if the range of interactions in Eqs. A.1 and A.2 can be restricted. For

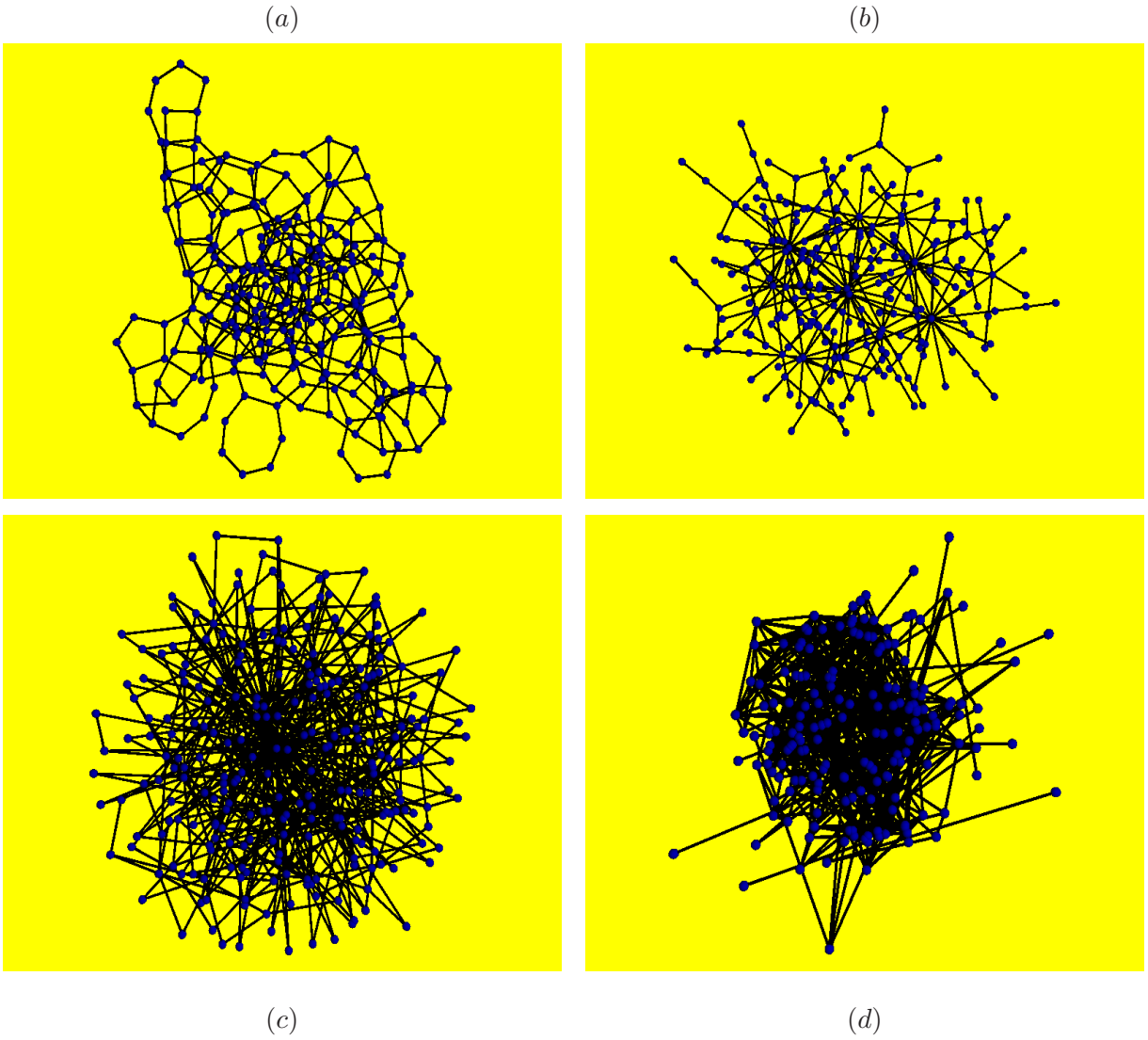

Figure A.4: Emergent layouts in the case of next-neighbor spring model approximation for different graphs: (a) planar graph of Fig. A.1; (b) scale-free tree of Fig. A.3; (c) clustered scale-free graph of Fig. A.3; (d) gene network from Ref. (Živković *et al.*, 2006). Relative numbers of edge crossings χ are: 3.7%, 6.0%, 25.6%, 45.0%.

instance here we use next-neighbor interactions in the sums in Eqs. A.1 and A.2 and apply to different graphs. We studied when this approximation gives satisfactory results.

For this purpose we studied the next-neighbor spring model on four different networks shown

on Fig. A.4: planar cellular graph, scale-free tree, clustered sparse scale-free graph, and gene network.

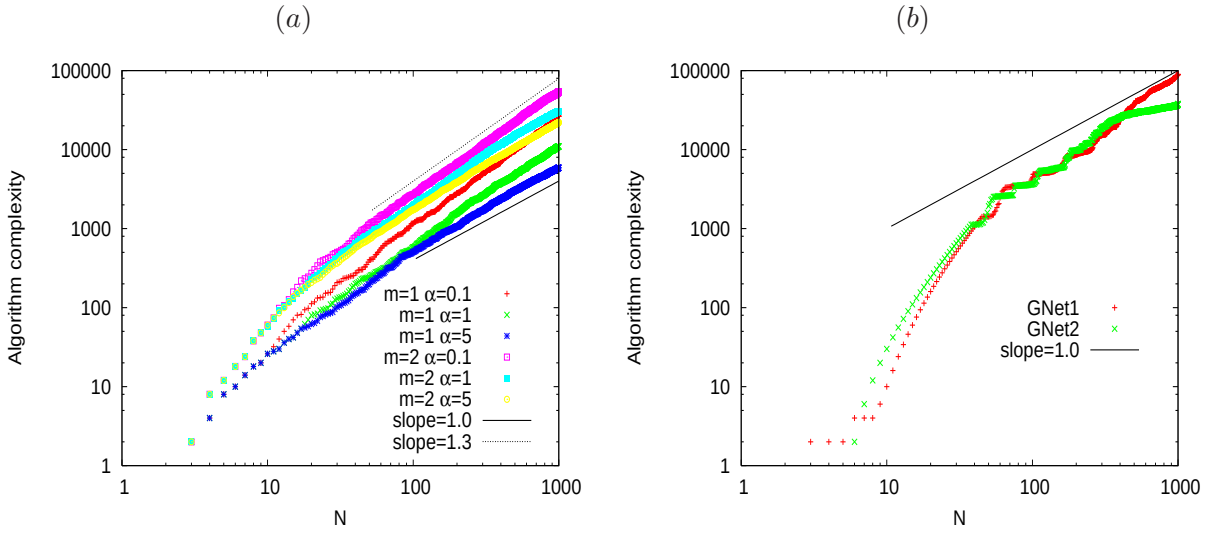

Figure A.5: Algorithm complexity $N\times < k_{nn} >$ on size of network N: (a) Growing network model from (Tadić, 2001) for different model parameters (b) Gene networks from (Živković *et al.*, 2006).

In the case when clustering is too small the emergent layouts are not well outstretched. However, in the case of sparse networks with higher clustering coefficient the algorithm seems much better (see Fig. A.4(c)). In the case of not-scalefree gene network, see example in Fig. A.4(d) the next-neighbor approximation does not give a good layout.

The complexity of the energy calculation algorithm is proportional to the mean value of next-neighbors $< k_{nn} >$. The one computational step (loop through all nodes) in both energy minimization algorithms takes $N\times < k_{nn} >$ calculations. Since the mean value $< k_{nn} >$ increases with system size and saturates at a threshold, the complexity of energy calculation algorithm for all nodes appears to be proportional to system size N instead to N^2. For the network sizes around the threshold value, the exponent is between one and two (see Fig. A.5).

Three energy models for two-dimensional visualization of graphs have been tested. We give certain quantitative measures of efficiency of the energy minimization algorithm. We presented layouts for different type of graphs, in particular the graphs which appear in applications of statistical physics to real-world networks. In summary we find that different algorithms work

differently depending on the graph structure. For particular graph type we summarize the method of choice in Table A.1.

Table A.1: For different graph structures the listed are methods of choice with metropolis minimization.

Graph structure	Visualization Method of Choice	χ
Planar graph with loops	Kamada-Kawai model	0.01%
Scale-free trees	Spring model - infinite range interaction	0.26%
Scale-free clustered	Spring model- short range interaction	26%
Non-SF clustered	??	45%

Appendix B

Publications Related to Thesis

1. M. Šuvakov and B. Tadić, *Charge Transport in Assembled Nanoparticle Structures*, in preparation (2008)
2. M. Šuvakov and B. Tadić, *Collective Charge Fluctuations in Single-Electron Processes on Nano-Networks*, JSTAT_032P_1008 (2008)
3. A. Stannard, M. O. Blunt, E. Pauliac-Vaujour, C. P. Martin, P. Moriarty, I. Vancea, U. Thiele, M. Šuvakov and B. Tadić, *Patterns and Pathways in Nanoparticle Self-Organization*, Chapter in book: Handbook of Nanoscience and Nanotechnology, Oxford University Press, in press (2008)
4. Milovan Šuvakov, *Physics Based Algorithms for Sparse Graph Visualization*, ICCS 2008, Lecture Notes in Computer Science, Springer Berlin, **5102**, pp. 593-600 (2008)
5. Milovan Šuvakov and Bosiljka Tadić, *Simulation of the Electron Tunneling Paths in Network of Nano-particle Films*, ICCS 2007, Y. Shi et al., Eds., Lecture Notes in Computer Science, Springer Berlin, **4488**, Part II, pp. 641-648 (2007)
6. B. Tadić and M. Šuvakov, *Multiscale Network Models of Nano-Materials: Structure and Dynamics* , Symposium Condensed-Matter Physics SFKM2007, Vrsac, Serbia, 16-20 September 2007.
7. M. O. Blunt, M. Šuvakov, F. Pulizzi, C. P. Martin, E. Pauliac-Vaujour, A. Stannard, A. W. Rushforth, B. Tadić, and P. Moriarty, *Charge Transport in Cellular Nanoparticle Networks: Meandering through Nanoscale Mazes*, Nano Letters **7**, pp. 855-860 (2007)
8. M. Šuvakov and B. Tadić, *Transport Processes on Homogeneous Planar Graphs with Scale-Free Loops*, Physica A **372** pp. 354 (2006)

9. M. Šuvakov and B. Tadić, *Topology of cell-aggregated planar graphs*, ICCS 2006, V.N. Alexandrov et al., Eds., Lecture Notes in Computer Science, Springer Berlin, **3993**, Part III, pp. 1098-1105 (2006)

References

Ahuja, R., Magnanti, T. & Orlin, J. (1993). *Network Flows: Theory, Algorithms and Applications*. Prentice Hall (New Jersey). 28

Albert, R. & Barabasi, A. (2002). Statistical mechanics of complex networks. *Reviews of Modern Physics*, **74**, 47–97. 13

Aldaye, F., Palmer, A. & Sleiman, H. (2008). Assembling materials with dna as the guide. *Science*, **321**, 1795. 3

Alivisatos, A., Johnsson, K., Peng, X., Wilson, T., Loweth, C., Bruchezjr, M. & Schultz, P. (1996). Organization of 'nanocrystal molecules' using dna. *Nature*, **382**, 609–611. 3

Alivisatos, P. (2004). The use of nanocrystals in biological detection. *Nature Biotechnology*, **22**, 47–52. 8

Argollo de Menezes, M. & Barabasi, A. (2004). Fluctuations in network dynamics. *Phys. Rev. Lett.*, **92**, 028701. 14, 52

Bakhvalov, N., Kazacha, G., Likharev, K. & Serdyukova, S. (1991). Statics and dynamics of single-electron solitons in two-dimensional arrays of ultrasmall tunnel junctions. *Phisica B*, **173**, 319–328. 2, 31, 32

Batagelj, V. (2008). `http://vlado.fmf.uni-lj.si/pub/networks/pajek/`. 15

Bezryadin, A., Dekker, C. & Schmid, G. (1997). Electrostatic trapping of single conducting nanoparticles between nanoelectrodes. *Appl. Phys. Lett.*, **71**, 1273. 36

Blunt, M., Martin, C., Ahola-Tuomi, M., Pauliac-Vaujour, E., Sharp, P., Nativo, P., Brust, M. & Moriarty, P. (2007a). Coerced mechanical coarsening of nanoparticle assemblies. *Nature Nanotechnology*, **2**, 167–170. 3

Blunt, M., Martin, C., Pauliac-Vaujour, E., Stannard, A., Moriarty, P., Vancea, I. & Thiele, U. (2007b). Controlling pattern formation in nanoparticle assemblies via directed solvent dewetting. *Phys. Rev. Lett.*, **99**, 116103. 7, 21

Blunt, M., Šuvakov, M., Pulizzi, F., Martin, C., Pauliac-Vaujour, E., Stannard, A., Rushforth, A., Tadić, B. & Moriarty, P. (2007c). Charge transport in cellular nanoparticle networks: meandering through nanoscale mazes. *Nano Letter*, **7**, 855. 2, 14, 17, 19, 21, 31, 32, 46, 74

Boccaletti, S., Latora, V., Moreno, Y., Chavez, M. & Hwang, D. (2006). Complex networks: Structure and dynamics. *Phys. Rep.*, **424**, 175–308. 13

Boguna, M. & Corral, A. (1997). Long-tail trapping times and levy flights in a self-organized critical granular systems. *Phys. Rev. Lett.*, **78**, 4950–3. 50

Bollobás, B. (1998). *Modern Graph Theory*. Springer (New York). 12, 13, 20, 22, 28, 80

Brennan, J., Hatzakis, N. & T. Tshikhudo, e. (2006). Bionanoconjugation via click chemistry: The creation of functional hybrids of lipases and gold nanoparticles. *Bioconjug Chem.*, **17**, 1373–1375. 57

Corral, A. (2004). Long-term clustering, scaling and universality in the temporal occurence of earthquakes. *Phys. Rev. Lett.*, **92**, 108501. 50

Corral, A. (2005). Mixing of rescaled data and bayesian interface for earthquakes recurrence times. *Nonlinear processes Geophys.*, **12**, 89–100. 50

Corral, A. (2006). Universal earthquake-occurence jumps, correlation with time and anomalous diffusion. *Phys. Rev. Lett.*, **97**, 17850. 50

Di Battista, G., Tollis, I., Eades, P. & Tamassia, R. (1998). *Graph Drawing: Algorithms for the Visualization of Graphs*. Prentice Hall. 15

Di Ventra, M., Evoy, S. & Heflin, J., eds. (2004). *Introduction to Nanoscale Science and Technology*. Technology & Industrial Arts, Springer. 31

Dorogovtsev, S. & Mendes, J. (2003). *Evolution of Networks*. Oxford University Press. 12

Duch, J. & Arenas, A. (2006). Scaling of fluctuations in traffic on complex networks. *Phys. Rev. Lett.*, **96**, 218702. 52

Duruöz, C.I., Clarke, R.M., Marcus, C.M. & Harris, J.S., Jr. (1995). Conduction threshold, switching and hysteresis in quantum dot arrays. *Phys. Rev. Lett.*, **74**, 3237–3240. 31

Eades, P. (1984). A heuristic for graph drawing. *Congraessus Numerantium*, **42**, 149–160. 15, 79, 80

Elteto, K., Lin, X.M. & Jaeger, H.M. (2005). Electronic transport in quasi-one-dimensional arrays of gold nanocrystals. *Phys. Rev. B*, **71**. 2, 31

Ferry, D. & Goodnick, S. (1997). *Transport in Nanostructures*. Cambridge University Press. 2, 17, 31, 32, 33

Freeman, L. (1977). A set of measures of centrality based on beetweenness. *Sociometry*, **40**, 35–41. 20

Ge, G. & Brus, L. (2000). Evidence for spinodal phase separation in two-dimensional nanocrystal self-assembly. *J. Phys. Chem. B*, **104**, 9573–9575. 5

Geigenmuller, U. & Schon, G. (1989). Single-electron effects in arrays of normal tunnel junctions. *Europhys. Lett.*, **10**, 765–770. 2, 32, 38

Guéron, S., Deshmukh, M.M., Myers, E.B. & Ralph, D.C. (1999). Tunneling via individual electronic states in ferromagnetic nanoparticles. *Phys. Rev. Lett.*, **83**, 4148–4151. 36

Guo, L., Leobandung, E. & Chou, S. (1997). A silicon single-electron transistor memory operating at room temperature. *Science*, **275**, 649. 2

Huber, R. (1986). Structural basis for antigen-antibody recognition. *Science*, **233**, 702. 8, 57

I. Jelesarov, L.l. & Bosshard, H. (1996). Probing the energetics of antigen-antibody recognition by titration microcalorimetry. *METHODS: A Companion to Methods in Enzymology*, **9**, 533. 58

Kamada, T. & Kawai, S. (1989). An algorithm for drawing general undirected graphs. *Inf. Process. Lett.*, **31**, 7–15. 15, 79

Kohno, H. & Takeda, S. (2007). Non-gaussian fluctuation in the charge transport of si nanochains. *Nanotechnology*, **18**, 359706. 72

Kujawski, B., Tadić, B. & Rodgers, G. (2007). Preferential behaviour and scaling in diffusive dynamics on networks. *New Journal of Physics*, **9**, 000. 14, 52

Lawler, G. (1991). *Intersections of Random Walks*. Birkhauster - Boston. 19

Lee, J., Lee, E. & Rikvold, P. (2006). Waiting-time distributions for a stock-market index. *J. Korean Phys. Soc.*, **48**, 123–6. 50

Likos, C. (2001). Effective interactions in soft condensed matter physics. *Physics Reports*, **348**, 267–439. 3, 8

Lu, P., Zaccarelli, E., Ciulla, F., Schofield, A., Sciortino, F. & Weitz, D. (2008). Gelation of particles with short-range attraction. *Nature Letters*, **453**, 499–504. 8

Maillard, M., Motte, L., Ngo, A. & Pileni, M. (2000). Rings and hexagons made of nanocrystals: A marangoni effect. *J. Phys. Chem. B*, **104**, 11871–11877. 8, 73

Martin, C., Blunt, M. & Moriarty, P. (2004). Nanoparticle networks on silicon: Self-organized or disorganized? *Nano Lett.*, **4**, 2389 –2392. 7, 19, 74

Middleton, A. & Wingreen, N. (1993). Collective transport in arrays of small metallic dots. *Phys. Rev. Lett.*, **71**, 3198–3201. 2, 31, 32, 38

Mirkin, C. (2000). Programming the assembly of two- and three-dimensional architectures with dna and nanoscale inorganic building blocks. *Inorg. Chem.*, **39**, 2258–2272. 1, 2, 4, 8, 9, 10, 57, 74

Mirkin, C., Letsinger, R., Mucic, R. & Storhoff, J. (1996). A dna-based method for rationally assembling nanoparticles into macroscopic materials. *Nature*, **382**, 607–609. 8, 57

Moriarty, P. (2001). Nanostructured materials. *Reports on Progress in Physics*, **64**, 297–381. 1, 3, 4, 21

Moriarty, P., Taylor, M. & Brust, M. (2002). Nanostructured cellular networks. *Phys. Rev. Lett.*, **89**, 248303. 7, 8, 21, 23, 31, 73

Mossa, S., Sciortino, F., Tartaglia, P. & Zaccarelli, E. (2004). Ground state clusters for short-range attractive and long-range repulsive potentials. *Langmuir*, **20**, 10756. 57, 58

Murray, C., Kagan, C. & Bawendi, M. (2000). Synthesis and characterization of monodisperse nanocrystals and close-packed nanocrystal assemblies. *Ann. Rev. Mater. Sci.*, **30**, 545–610. 4

Nepomnyashchy, A. & Golovin, A., eds. (2006). *Self-assembly, Pattern Formation And Growth Phenomena in Nano-systems*. Springer. 1

Nykypanchuk, D., Maye, M., van der Lelie, D. & O.Gang (2008). Dna-guided crystallization of colloidal nanoparticles. *Nature Letters*, **451**, 549–552. 3, 4, 8, 9, 57

Park, S., Lytton-Jean, A., Lee, B., Weigand, S., Schatz, G. & Mirkin, C. (2008). Dna-programmable nanoparticle crystallization. *Nature*, **451**, 553–556. 3, 4, 8, 9, 57

Parthasarathy, R., Lin, X. & Jaeger, H. (2001). Electronic transport in metal nanocrystal arrays: The effect of structural disorder on scaling behavior. *Phys. Rev. Lett.*, **87**, 186807. 31, 44, 45, 75

Parthasarathy, R., Lin, X., Elteto, K., Rosenbaum, T. & Jaeger, H. (2004). Percolating through networks of random thresholds: Finite temperature electron tunneling in metal nanocrystal arrays. *PRL*, **92**, 076801. 2, 31, 32

Pileni, M. (2001). Nanocrystal self-assemblies: Fabrication and collective properties. *J. Phys. Chem. B*, **105**, 3358–3371. 4

Pileni, M. (2006). Self-organization of inorganic nanocrystals. *J. Phys.: Condensed Matter*, **18**, S67–S84. 4

Pileni, M. (2007). Self-assembly of inorganic nanocrystals: Fabrications and collective intrinsic properties. *Acc. Chem. Res.*, **40**, 685–693. 4

Pluchino, A., Rapisarda, A. & Tsallis, C. (2008). A closer look at the indications of q-generalized central limit theorem behavior in quasi-stationary states of the hmf model. *PHYSICA A*, **387**, 3121. 54

Prim, R. (1957). Shortest connection networks and some generalisations. *Bell System Technical Journal*, **36**, 1389–1401. 12

Rabani, E., D. R. Reichman, P.G. & Brus, L. (2003). Drying-mediated self-assembly of nanoparticles. *Nature*, **426**, 271–274. 5, 6, 7, 19, 73

Rimberg, A., Ho, T. & Clarke, J. (1995). Scaling behavior in the current-voltage characteristic of one- and two-dimensional arrays of small metallic islands. *Phys. Rev. Lett.*, **74**, 4714–4717. 2, 31

Robinson, B., ed. (2003). *Self-Assembly*. IOS Press. 1

S. W. Koch, F.A., R. C. Desai (1983). Dynamics of phase separation in two-dimensional fluids: Spinodal decomposition. *Phys. Rev. A*, **27**, 2152–2167. 5, 73

Sabatelli, L., Keating, S., Dudley, J. & Richmond, P. (2002). Waiting-time distributions in financial markets. *Eur. Phys. J. B*, **27**, 273–5. 50

Sanchez, R. & Carreras, B. (2002). Waiting-time statistics of self-organized criticality systems. *Phys. Rev. Lett.*, **88**, 068302. 50

Stannard, A., Blunt, M., Pauliac-Vaujour, E., Martin, C., Moriarty, P., Vancea, I., Thiele, U., Šuvakov, M. & Tadić, B. (2008). *in review*, chap. Patterns and Pathways in Nanoparticle Self-Organization. Oxford University Press. 4, 6, 73

Stavans, J. (1993). Evolution of cellular structures. *Rep. Prog. Phys.*, **56**, 733–789. 7, 21, 22

Storhoff, J. & Mirkin, C. (1999). Programmed materials synthesis with dna. *Chem. Rev.*, **99**, 1849–1862. 4

Tadić, B. (2001). Dynamics of directed graphs: the world-wide web. *Physica A*, **293**, 273–284. 13, 74, 77, 83, 85

Tadić, B. (2006). Structure of noise and flow in transport on complex networks. *Prog. Theor. Phys. Suppl.*, **162**, 112–20. 14, 52

Tadić, B. (2008). *Systems Self-Assambly: Multidisciplinary Snapshots*, chap. From Microscopic Rules to Emergent Cooperativity in Large Scale Patterns. Elsevier. 1, 3, 14

Tadić, B. & Thurner, S. (2004). Information super-diffusion on structured networks. *Physisca A*, **332**, 566–584. 14, 51

Tadić, B., Malarz, K. & Kulakowski, K. (2005). Magnetization reversal in spin patterns with complex geometry. *Phys. Rev. Lett.*, **94**, 137204. 14

Tsallis, C. (1988). Possible generalization of boltzmann-gibbs statistics. *J. Stat. Phys.*, **52**, 479. 49, 54

Tsallis, C., Rapisarda, A., Pluchino, A. & Borges, E. (2007). On the non-boltzmannian nature of quasi-stationary states in long-range interacting systems. *Physica A*, **381**, 143. 72

Šuvakov, M. (2008). Physics based algorithms for sparse graph visualization. In M.B. *et al.*, ed., *Lecture Notes in Computational Science - ICCS 2008, Part II*, vol. 5102 of *Lecture Notes in Computer Science*, 593–600, Springer, Berlin. 14, 15

Šuvakov, M. & Tadić, B. (2006a). Topology of cell-aggregated planar graphs. In V.A. *et al.*, ed., *Computational Science — ICCS 2006*, vol. 3993 of *Lecture Notes in Computer Science*, 1098–1105, Springer, Berlin. 2, 13, 14, 17, 27, 74

Šuvakov, M. & Tadić, B. (2006b). Transport processes on homogeneous planar graphs with scale-free loops. *Physica A*, **372**, 354. 2, 14, 17, 47

Šuvakov, M. & Tadić, B. (2007). Simulation of the electron tunneling paths in network of nano-particle films. In Y.S. *et al.*, ed., *Lecture Notes in Computational Science - ICCS 2007*, vol. 4488 of *Lecture Notes in Computer Science*, 641–648, Springer, Berlin. 2, 14, 17

Šuvakov, M. & Tadić, B. (2008). Collective charge fluctuations in single-electron processes on nano-networks. 14

Živković, J., Tadić, B., Wick, N. & Thurner, S. (2006). Statistical indicators of collective behavior and functional clusters in gene expression networks of yeast. *Europ. Physical Journal B*, **50**, 255–258. 13, 14, 74, 77, 79, 84, 85

Wernsdorfer, W., Bonet Orozco, E., Hasselbach, K., Benoit, A., Mailly, D., Kubo, O., Nakano, H. & Barbara, B. (1997). Macroscopic quantum tunneling of magnetization of single ferrimagnetic nanoparticles of barium ferrite. *Phys. Rev. Lett.*, **79**, 4014–4017. 36

Witten, T. & Sander, L. (1981). Diffusion-limited aggregation, a critical phenomenon. *Phys. Rev. Lett.*, **47**, 1400–1403. 22

Wybourne, M., Clarke, L., Yan, M., Cai, S., Brown, L., Hutchison, J. & Keana, J. (1997). Coulomb-blockade dominated transport in patterned gold-cluster structures. *Jpn. J. Appl. Phys.*, **36**, 7796–7800. 2, 31

Yosef, G. & Rabani, E. (2006). Self-assembly of nanoparticles into rings: A lattice-gas model. *J. Phys. Chem. B*, **110**, 20965. 7

Zaccarelli, E. (2007). Colloidal gels: equilibrium and non-equilibrium routes. *J. Phys.:Cond. Matter*, **19**, 323101. 8, 57

MILOVAN ŠUVAKOV

DOCTORAL DISSERTATION